CEFET/RJ
DIRETORIA DE PESQUISA E PÓS-GRADUAÇÃO

A Framework for Autonomous UAV in Offshore Mooring Tasks

Gabryel Silva Ramos

Dissertação de Mestrado apresentada ao Programa de Pós-Graduação em Engenharia Elétrica, Centro Federal de Educação Tecnológica Celso Suckow da Fonseca, CEFET/RJ, como parte dos requisitos necessários à obtenção do título de mestre.

Orientadora:
Milena Faria Pinto

Rio de Janeiro,
Dezembro, 2021

A Framework for Autonomous UAV in Offshore Mooring Tasks

Dissertação de Mestrado apresentada ao Programa de Pós-Graduação em nome do programa, Centro Federal de Educação Tecnológica Celso Suckow da Fonseca, CEFET/RJ, como parte dos requisitos necessários à obtenção do título de mestre.

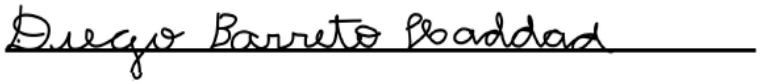
Gabryel Silva Ramos

Aprovada por:



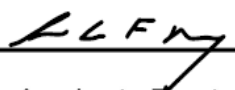
Presidenta, Milena Faria Pinto, D.Sc. (orientadora)

Centro Federal de Educação Tecnológica Celso Suckow da Fonseca (CEFET/RJ)



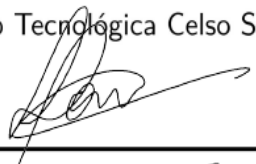
Diego Barreto Haddad, D.Sc.

Centro Federal de Educação Tecnológica Celso Suckow da Fonseca (CEFET/RJ)



Ana Lucia Ferreira de Barros, PhD.

Centro Federal de Educação Tecnológica Celso Suckow da Fonseca (CEFET/RJ)



Leonardo de Melo Honório, D.Sc.

Universidade Federal de Juiz de Fora (UFJF)



Amalia Cristina Urdiales Garcia, D.Sc.

Universidad de Málaga (UMA)

Rio de Janeiro,

Dezembro, 2021

Ficha catalográfica elaborada pela Biblioteca Central do CEFET/RJ

R175 Ramos, Gabryel Silva
A framework for autonomous UAV in offshore mooring tasks / Gabryel Silva Ramos. — 2022.
80f. : il. (algumas color.) , enc.

Dissertação (Mestrado) Centro Federal de Educação Tecnológica Celso Suckow da Fonseca, 2022.
Bibliografia : f. 74-80
Orientador: Milena Faria Pinto

1. Drone – Métodos de simulação. 2. Indústria offshore de petróleo. 3. Robôs - Sistemas de controle. 4. Visão por computador. 5. Campos petrolíferos. I. Pinto, Milena Faria (Orient.). II. Título.

CDD 629.8

Elaborada pela bibliotecária Tania Mello – CRB/7 nº 5507/04

AGRADECIMENTOS

Aos meus pais, que com muito sacrifício me permitiram sonhar e chegar onde estou.

À minha orientadora Milena Faria Pinto por todas as contribuições com o projeto, além da disponibilidade e boa vontade ao longo do processo de pesquisa. Obrigado por compartilhar comigo não apenas seu conhecimento e experiência, mas sobretudo por me inspirar coragem para dar passos além do que eu imaginei que meus pés alcançassem.

Aos meus competentes colegas de trabalho, principalmente Eduardo Soares Silveira de Souza e Gilberto Beduhn Machado, pelas contribuições para avaliação técnica e econômica feita em minha pesquisa e consultoria sobre as operações offshore.

Aos professores e servidores do CEFET-RJ por sua competência e dedicação. A qualidade da pesquisa e ensino das instituições públicas, das quais sinto orgulho em ter sido discente, é inigualável no Brasil. O ensino público é o alicerce da minha vida e certamente de outros milhares de brasileiros, e esse resultado eu só posso atribuir ao trabalho de vocês. Muito obrigado.

Aos meus colegas do CEFET-RJ por todas as contribuições e trabalho em equipe durante este curso de pós-graduação.

À banca examinadora, pelo convite aceito para avaliação deste trabalho.

Gabryel Silva Ramos

"Try not. Do or do not. There is no try."

Yoda

RESUMO

A Framework for Autonomous UAV in Offshore Mooring Tasks

Gabryel Silva Ramos

Orientadora:

Prof. Milena Faria Pinto, Dsc.

À medida que a exploração de óleo e gás encaminha-se para campos cada vez mais profundos no cenário da indústria brasileira, as operações de *offloading* se consolidam como a opção mais viável para escoar a produção. No entanto, esse tipo de operação demanda recursos caros, como navios aliviadores e barcos de apoio, e apresentam riscos operacionais que, apesar de geridos, limitados e mitigados para serem os mais baixos possíveis, ainda estão presentes. Neste contexto, esta pesquisa propõe a utilização de Veículos Aéreos Não Tripulados (VANTs) em modo autônomo para realizar a transferência do cabo mensageiro do navio aliviador para a plataforma em vez de usar barcos de manuseio de linha (para operações convencionais que utilizam esses recursos) ou os canhões de lançamento de cabo mensageiro (para operações de posicionamento dinâmico). Isso representa uma solução alternativa viável para reduzir custos e riscos nessas tarefas e uma possibilidade de eliminar algumas condições meteorológicas e oceanográficas limitantes às operações, uma vez que o VANT será suscetível apenas às condições do vento, e não às condições de mar e visibilidade como as embarcações de manuseio de linha. É apresentada neste trabalho uma metodologia de navegação híbrida baseada em visão computacional e técnica de fusão de sensores com Filtro de Kalman Estendido para VANTs autônomos. O *framework* proposto foi desenvolvido em *Robotics Operating System* (ROS), testado em um ambiente simulado realista considerando diversas restrições operacionais práticas. O mesmo controlador foi testado em um VANT físico usando modelos de navio em escala e também em um teste de campo a bordo de uma instalação de produção para validar os resultados da simulação. Observou-se que o controlador desenvolvido se comportou muito bem e as simulações e testes físicos mostraram resultados robustos. Com base nesses testes, foi realizada uma avaliação econômica simulando a aplicação dessa tecnologia em dois cenários distintos de campos petrolíferos em águas profundas no Brasil.

Ancoragem Offshore, Operação de Transferência de Cabo Offshore, Tecnologias Autônomas Offshore, Veiculo Aereo Não Tripulado, Visão Computacional, Filtro de Kalman Estendido.

ABSTRACT

A Framework for Autonomous UAV in Offshore Mooring Tasks

Gabryel Silva Ramos

Advisor:

Prof. Milena Faria Pinto, Dsc.

As oil and gas exploration goes toward deeper fields in the Brazilian industry scenario, the offloading operations consolidate themselves as the most viable option to drain production. However, this operation demands expensive resources, such as shuttle tankers and support boats, and presents operational risks, which despite managed, limited and mitigated to be as low as reasonably possible, are still present. Therefore, this research proposes to use Unmanned Aerial Vehicles (UAVs) in an autonomous mode to carry out the messenger line from the shuttle tanker to the oil rig instead of using a Line Handling (LH) boat (for conventional operations that use those resources) or the messenger cable launching guns (for dynamic positioning operations). This represents a viable alternative solution to reduce costs and risks in these tasks and a possibility to eliminate some meteorologic and oceanographic limiting conditions to operations, since the UAV will be susceptible only to wind conditions, and not to sea and visibility conditions like LHs are. It is presented in this work a hybrid navigation methodology based on computer vision and sensor fusion technique with Extended Kalman Filter for autonomous Unmanned Aerial Vehicles (UAV). The proposed framework was developed in Robotics Operating System (ROS), tested in a realistic simulated environment considering several practical operational constraints. The same controller was tested on a physical UAV using scale ship models and also in a field test aboard a production facility to validate simulation results. The developed controller was noted to behave very well and simulations and physical tests showed robust results. Based on these tests, an economical evaluation was conducted by simulating the application of this technology in two distinct Brazilian deep water oilfield scenarios.

Offshore Mooring, Offshore Cable Transfer Operation, Autonomous Offshore Technologies, UAV, Computer Vision, Extended Kalman Filter.

Contents

I Introduction **15**

I.1 Considerations and Work Motivation . . . 15

I.2 Main Contributions . . . 17

I.3 Papers associated with this research work . . . 18

I.4 Organization . . . 18

II Background and Related Works **20**

II.1 Offshore Technologies and Operation . . . 20

II.2 Satellite Navigation . . . 23

II.3 Convolutional Neural Networks for Object Detection . . . 25

II.4 Kalman Filter . . . 30

II.5 Related Works . . . 33

III Materials and Methods **37**

III.1 Initial Waypoint GNSS Navigation . . . 39

III.2 YOLOff Training and Validation . . . 42

III.3 Extended Kalman Filter . . . 43

III.4 Cable delivery location . . . 49

III.5 Flight controller with MavROS . . . 50

III.6 Technical and Economic Feasibility Study . . . 51

III.6.1 Project in Final Operational Year . . . 52

III.6.2 Project in the First Years of Production . . . 57

IV Results and Discussion **60**

IV.1 Object Detection Training and Results . . . 60

IV.2 Sensor Fusion . . . 62

IV.3 Simulation Results . . . 63

IV.3.1 Messenger Line Considerations . . . 68

IV.4 Scale test . . . 72

IV.5 Field test . . . 75

IV.6 Economic Evaluation 77
IV.6.1 Final Year of Production Scenario 77
IV.6.2 First Years of Production Scenario 83

V Conclusions and Future Work **86**

V.1 Conclusions 86
V.2 Future Propositions 86
References 88

List of Tables

II.1 Related works summary. 36

IV.1 Detection results. 61
IV.2 Detection evaluation metrics. 61
IV.3 EKF validation results. 62
IV.4 List of messenger line's parameters. 69
IV.5 FPSO's Estimated Daily Production. 78
IV.6 Resources Tariffs. 79
IV.7 Brazilian considered taxes. 80
IV.8 Selected UAVs, characteristics and investment costs. 80
IV.9 UAV operational costs. 81
IV.10 Economic results. 81
IV.11 Economic indicators. 82
IV.12 Offloading parameters. 83
IV.13 UAV operational costs. 84
IV.14 Cost reduction evaluation. 85

List of Figures

II.1 Tandem approach scheme (elaborated by the author). 21
II.2 Line Throwing Apparatus tool (elaborated by the author). 21
II.3 Tandem mooring in offloading operation (Ramos et al. 2021). 22
II.4 Typical mooring link configuration (Ramos et al. 2021). 22
II.5 Executed waypoint flight. The red color represent waypoints, yellow represent the projected trajectory and green represent the executed trajectory (elaborated by the author). 24
II.6 RTK traingulation and trilateration representation (adapted from (OXTS 2021)). 25
II.7 Basic CNN for object detection architecture (adapted from (Camacho 2018)). 26
II.8 YOLOv3 convolutional neural network structure (adapted from (Redmon e Farhadi 2018).) 27
II.9 Example of YOLOff detection with the 13x13 feature map (adapted from (Balsys 2019)). 29
II.10 Basic YOLOff detection model (adapted from (Balsys 2019)). 29
II.11 Box class probability calculation (adapted from (Balsys 2019)). 30

III.1 UAV's rigid body simplified illustration (elaborated by the author). 37
III.2 Operation flowchart (Ramos et al. 2021). 38
III.3 Linear trajectory (Ramos et al. 2021). 39
III.4 Example of an annotated image in CVAT (Ramos et al. 2021). 42
III.5 Cartesian operation scheme (elaborated by the author). 43
III.6 Control loop of approaching flight mode strategy adopted in stage 2 (consider yaw_y as the $\text{yaw}_{k,\text{YOLOff}}$, $yaw_L K$ as the $\text{yaw}_{k,\text{LK}}$, and yaw_c as the $yaw_{k,compass}$ of the model description)(elaborated by the author). 48
III.7 EKF validation setup with the rotary encoder detail in (a) (elaborated by the author). . 49
III.8 Schmitt-Trigger debouncing circuit (elaborated by the author). 49
III.9 IOU metric definition (adapted from (Balsys 2019)). 50
III.10 Robotic system active nodes and messages (elaborated by the author). 51
III.11 Production Decline Curves (elaborated by the author). 52
III.12 FPSO's Historical Production (ANP 2021). 53
III.13 Production Analysis for the Harmonic Decline (elaborated by the author). 53

IV.1 YOLOff results for all classes (Ramos et al. 2021). 60

IV.2 YOLOff example of detection (Ramos et al. 2021). 61
IV.3 EKF validation essay results (elaborated by the author). 62
IV.4 Simulated hexarotor on Gazebo (elaborated by the author). 63
IV.5 Simulated offloading world on Gazebo (elaborated by the author). 64
IV.6 Calculated and performed trajectories (Ramos et al. 2021). 64
IV.7 Flight height in simulation step 1 (elaborated by the author). 65
IV.8 Drone orientation in simulation step 1 (elaborated by the author). 66
IV.9 Approach trajectory results. (a) 2D trajectory (XY plan) (b) 3D trajectory (elaborated by the author). 66
IV.10 Yaw readings and prediction during simulation (elaborated by the author). 67
IV.11 Marker detection results (elaborated by the author). 68
IV.12 Marker detection on simulation (adapted from (Ramos et al. 2021)). 68
IV.13 UAV's trajectory in simulation. (a) 2D executed trajectory (XY plan) compared to planned. (b) 3D executed trajectory compared to the direct ideal (Ramos et al. 2021). . 69
IV.14 Messenger line model for simulations. 70
IV.15 Dynamic forces acting on a line model link. 70
IV.16 Messenger line in simulation. 71
IV.17 Typhoon H480 pitch and roll angles (a) and vibration (b) transporting the line in simulation. 72
IV.18 Ship model used for real tests (elaborated by the author). 73
IV.19 Test UAV setup: (a) PixHawk Px4 FCU; (b) Base station running ROS system; (c) MavLink telemetry radio; (d) Turnigy 9XR radio; (e) RC receiver; (f) SE100 GPS Module; (g) [4x] Sunnysky 720KV brushless motor; (h) [4x] Hobbywing 40A Electronic Speed Controller; (i) Tattu 4 cells 5200mAh LiPo battery; (j) Camera gimbal; (k) Eachine TX03 NTSC FPV Camera; (l) Safety killswitch; (m) Current sensor (elaborated by the author). 73
IV.20 UAV used in real tests (elaborated by the author). 74
IV.21 Controller test on real UAV. 75
IV.22 Real UAV's trajectory in test. (a) 2D executed trajectory (XY plan) compared to the desired direct navigation. (b) 3D executed trajectory compared to the desired direct navigation 75
IV.23 Real test trajectory on map 76
IV.24 Yaw during the test on real UAV. 76
IV.25 VI approaching navigation in field test. 77
IV.26 VI approaching navigation in field test trajectory log. 77
IV.27 Yaw readings during VI approaching navigation field test. 78

IV.28 Oil inventory evolution in economic simulated scenario (Ramos et al. 2021). 79
IV.29 Cash flow comparison for each simulated month (Ramos et al. 2021). 81
IV.30 Accumulated gain on simulated period (Ramos et al. 2021). 82
IV.31 Accumulated volumes and offloading numbers by month within the economic simulation time (elaborated by the author). 84
IV.32 Monthly accumulated offloading costs comparison within the economic simulation time (elaborated by the author). 85

List of Abbreviations

AHTS	Anchor Handling Support Vessel 21, 55, 58, 83
BDS	BeiDou Navigation Satellite System 23
BLS	Bow Load System 21, 22, 23
CNN	Convolutional Neural Network 25, 26, 27, 33, 42
CVAT	Computer Vision Annotation Tool 42
DP	Dynamic Positioning 21, 22
EKF	Extended Kalman Filter 15, 16, 25, 31, 32, 34, 35, 36, 38, 41, 46, 47, 48, 62, 65, 67
FCU	Flight Control Unit 23, 37, 50, 51
FOV	Field Of View 34
FPSO	Floating Production Storage And Offloading 15, 17, 20, 21, 22, 23, 42, 52, 54, 55, 56, 57, 58, 63, 77, 78, 82, 83, 85
FSO	Floating Storage And Offloading 20, 21, 22, 23, 42, 54, 56, 58
GIS	Geographic Information Systems 23
GLONASS	GLObal NAvigation Satellite System 23
GNSS	Global Navigation Satellite 15, 16, 23, 24, 33, 36, 37, 67, 86
GNSS-RTK	Global Navigation Satellite System-RTK 33
GPS	Global Positioning System 23, 33, 34, 35, 38, 39, 41, 63, 65, 67
IMU	Inertial Measurement Unit 15, 16, 34, 35, 36, 37
IOU	Intersection Over Union 50, 64
KNN	K-Nearest Neighbors 30
LH	Line Handling 15, 21, 22, 23, 56
LIDAR	Light Detection And Ranging 25
MAE	Mean Absolute Error 62, 67
MSE	Mean Squared Error 62
NSV	*North Sea* Valve 22, 23
PID	Proportional-Derivative-Integrative 47
PPK	Post Processing Kinematics 24, 33, 67
QR	Quick Response 34, 49, 64
RC	Remote Controlled 16, 34

RGB Red, Blue, And Green 28

ROS Robot Operating System 16, 42, 50, 51, 63, 86

RTK Real Time Kinematics 24, 33, 67

SLAM Simultaneous Localization And Mapping 25

ST Shuttle Tanker 15, 58

UAV Unmanned Aerial Vehicle 15, 16, 17, 23, 24, 25, 32, 33, 34, 35, 36, 37, 38, 41, 47, 48, 50, 52, 56, 57, 58, 59, 63, 64, 65, 66, 67, 68, 69, 80, 82, 83, 84, 85, 86, 87

UKF Unscented Kalman Filter 35

UWB Ultra-Wideband 33

VI Vision Inertial 15, 16, 34, 35

YOLO You Only Look Once 30

YOLOV3 You Only Look Once Version 3 . . . . . 27, 28

Chapter I Introduction

I.1 Considerations and Work Motivation

Since the 1970's, robotic concepts have been used to offshore surface oil production facilities (Petillot et al. 2019). According to (Durdevic et al. 2019), the sector is transitioning from conventional operations to fully autonomous workplaces and installations utilizing new robotic technology, lowering operating costs and human labor while also improving safety and dependability (Yu et al. 2019). The flexibility and reliability of aerial robots, also known as Unmanned Aerial Vehicle (UAV), has piqued interest in a variety of applications in recent years (Ahmed et al. 2015; Pinto et al. 2020; Pinto et al. 2020; Rodin et al.; Andrade et al. 2019; Silva et al. 2016), and according to (Mullenders 2019), this includes several offshore ones. As research progresses, these robotic systems are demonstrating a high level of autonomy, allowing them to execute jobs safely with minimal human involvement (Selecký et al. 2015; Pinto et al. 2017; Pinto et al. 2019; Coelho et al. 2018).

Given the complicated process of mooring on offloading operations outlined in Chapter II and the usage of automated robotics solutions in the offshore oil and gas sector, robotics in offloading operations may be used to decrease risk, costs, time, and man-hour. In light of this, the present study offers a hybrid architecture for an UAV to fly autonomously from the Floating Production Storage and Offloading (FPSO) offshore facility to the Shuttle Tanker (ST), or vice-versa, arriving at a precise location on the target structure. The concept is that in the future, the vehicle will be able to carry and distribute the messenger line, enhancing operational safety by extending the distance between boats receiving the messenger line and exposing fewer crew members to danger by managing the line throwing equipment. By minimizing the need for Line Handling (LH) boats, operating time, and potentially being less sensitive to sea conditions, the suggested technique has the potential to save money on operations.

The methodology is called hybrid because it is based on two approaches: the initial positioning, where the UAV will fly through an automatically calculated trajectory based on Global Navigation Satellite (GNSS) and the final approaching, based on vision inertial (VI) navigation. In this last stage, the UAV will detect and track the region where it must go, and an Extended Kalman Filter (EKF) will be applied to fuse the information from the Inertial Measurement Unit (IMU) with camera heading (yaw) estimation to control the vehicle's resultant velocity, therefore approaching to the desired site with precision. To evaluate the designed framework, the controller package will be developed using Robot Operating

System (ROS) and a simulation will be performed in with Gazebo platform (Koenig e Howard 2004). The system also will be tested in a controlled environment with a simple UAV, using scale models to verify the implemented controller behavior.

The hybrid technique gets its name from the fact that it uses two approaches: initial positioning, in which the UAV follows an autonomously computed trajectory based on GNSS, and final approaching, which uses VI navigation. The UAV will identify and track the area where it must travel in this last step, and an EKF will be used to fuse the information from the IMU with camera heading (yaw) estimate to regulate the vehicle's resulting velocity, allowing it to approach the target location with accuracy. The controller package will be built using ROS, and a simulation will be run on the Gazebo platform (Koenig e Howard 2004) to test the proposed framework. The system will also be tested using a basic UAV in a controlled setting, utilizing scale models to validate the implemented controller behavior.

In terms of applicability, according to the Journal of Petroleum Technology (SPE 2018), a Dutch offshore and tugboat business filed for a patent to use UAVs for towing operations in ports. The project comprises of a manually-controlled multirotor with a camera that can identify a target (such as a window) and fire the messenger line with pinpoint accuracy. Their major contribution is the increased towing distance of cargo ships and tugboats for port mooring operations (Kotug 2018). The UAV is also fitted with a portable pneumatic line throwing device for firing the messenger line, but the operation is performed by Remote Controlled (RC) flight.

Other comparable uses are mentioned by (Frederiksen e Knudsen 2018), which reports on a marine logistics and drilling company's usage of manually-controlled UAVs for transporting tiny goods between boats, such as light-weighted equipment and medications. According to Kim et. al. (2019), UAV carrying messenger wires are also being tested outside of the offshore sector. They demonstrated a technique for building electricity transmission lines using manually-controlled UAV carrying messenger wires. This final paper discussed an effort to use this kind of robot to transport messenger lines and how to cope with wind drag on the wire being carried, but it focuses on manned RC operations.

Most studies on UAV carrying thin lines, such as suggested, or other tiny cargo of any kind concentrate on the application's goals, thus they're marketed as manual solutions. The current work, on the other hand, describes both the goal of carrying the messenger line and the autonomous strategy for doing so, which is based on computer vision and fusing camera readings with the yaw of the compass sensor to help the UAV maintain orientation as it approaches the delivery region of the destination ship. In this regard, very similar methods are being simulated for use in offshore wind farms (Durdevic et al. 2019), where the UAV identifies the wind turbines using computer vision and autonomously flies directly to the identified item to conduct a visual examination. This project, on the other hand, does not include fail-safe conditions or strong control methods, such as the EKF sensor fusion.

About vision, (Qin e Wang 2019) proposed an object tracking method to estimate object location

and utilizing Kalman Filter to cope with target tracking failure due by background color interference and obstacle occlusion for a limited period in non-offshore vision-assisted UAV navigation. The UAV in this project hovers above the item to keep it in the center of the picture, even if it is obscured by a screen. The navigation approach is similar to the one described in this paper, but the aim here is to approximate from the ship in order to achieve orientation control resilience if object identification fails or the UAV encounters wind drag. Similarly, Chuang et. al. (2019) presented a relative positioning method for a UAV based on a tracked item position on the picture with relation to the final spot location. Their approach is similar to the one suggested for adjusting the final UAV's location to deliver the messenger line depending on the identified marker.

Based on two extreme hypothetical situations, the study will also assess the technical, safety, and economic effects, both positive and negative, of implementing this suggested technology in industry. One will look at a real-world implementation of the concept based on an FPSO placed in a deepwater post-salt oilfield in Brazil in its last year of production, while the other will look at a new pre-salt project with an FPSO in its first year of production. In all situations, the study will evaluate cash flow cost reduction, investment payback time, net present value, and internal rate of return to validate the project's economic attractiveness.

I.2 Main Contributions

The primary aim of this study is to develop a technique for an autonomous UAV to fly from the fluctuating production plant to the shuttle tanker in order to mimic messenger cable delivering using computer vision and sensor fusion methods. Simulations in ROS and physical testing are used to evaluate the framework. As a result, the most important contributions may be summed up as follows:

- A novel automated approach to offshore messenger cable transfer operation, contributing to literature with an application not yet widely explored;
- A novel mathematical modeling that considers the agents' relative positioning, estimating the UAV's heading using computer vision. The guidance angle estimate based on percentage variation of the detected object and interest pixels by optical flow algorithm is not yet found in the literature;
- To simulate the framework in a realistic environment and to physically test the developed packages in order to verify the proposed hybrid approach's functionality as a proof of concept. Beyond the contribution to application, the controller packages and developed environment to perform simulation are a contribution to the community to future developments;
- The detailed evaluation of this novel technology as a real oil and gas project, taking into account real industry parameters. This is a contribution to literature, for this kind of study proved to be

rare in academic texts in a way that the addressed methodology may be replicated or enhanced for future economic and technical evaluations of robotics applications.

- A databank of 580 images of shuttle tankers, FPSOs, FSOs as well as digital 3D models, with the respective objects (ship, bow, mid-ship and stern) respectively annotated and organized in Pascal VOC files, ready to train new neural network computer vision models (Ramos e Pinto 2021).

I.3 Papers associated with this research work

Until the presented moment, this research work has generated reports in the form of two journal articles, being them:

- **Published:**

  Ramos, Gabryel Silva; Pinto, Milena Faria; de Souza, Eduardo Soares Silveira; Machado, Gilberto Beduhn and Gabriel Gelard Reis de Castro. "Technical and Economic Feasibility Study for Implementing a Novel Mooring-Assisting Methodology in Offloading Operations Using Autonomous Unmanned Aerial Vehicles". SPE Production & Operations (2021): doi: https://doi.org/10.2118/205524-PA.

- **Accepted for publication:**

  Ramos, Gabryel Silva; Pinto, Milena Faria; Honorio, Leonardo Melo; Haddad, Diego. "Hybrid Methodology based on Computational Vision and Sensor Fusion for Assisting Autonomous UAV on Offshore Messenger Cable Transfer Operation". Submitted to: Robotica on May 5^{th}, 2021.

- **Submitted:**

  Ramos, Gabryel Silva; Haddad, Diego; Barros, Ana L. F.; Honorio, Leonardo Melo; Pinto, Milena Faria. "EKF-Based Vision Assisted Target Tracking and Approaching forAutonomous UAV in Offshore Mooring Tasks". Submitted to: Mechatronics on September 25^{th}, 2021.

I.4 Organization

Chapter II will present the background of the research, where the theoretical revision of the related issues will be addressed, such as convolutional neural networks for object detection in images, as well as its training and detection metrics, Extended Kalman Filters, and sensor fusion. This chapter also will present the related works used as a reference for the methodology's implementation.

In Chapter III, it will be described the materials and methods used to build the described technology, including mathematical modeling and electronic setup, as well as validation steps to prove its function-

ality. The technical and economic feasibility study will also be presented, and also the scenario modeling references, methodology, and mathematical formulation.

The results obtained by applying those methods will be presented in Chapter IV. Moreover, critical analysis and discussion of these results will be covered within this section in order to show the methodology's functionality and robustness.

The final conclusions of this dissertation and the next steps to be taken on future works will be presented in Chapter V.

Chapter II Background and Related Works

II.1 Offshore Technologies and Operation

Because of their ability to store fluids in cargo tanks, the Floating Storage and Offloading (FSO) and FPSO production facilities are one of the most appealing choices for exploration and production projects with logistic constraints (Duggal e Minnebo 2020). The most prolific commercial oil fields in Brazil are progressively far from the coast, where the enormous post and pre-salt reservoirs are situated, as demonstrated in production and exploration reports published by the Brazilian National Petroleum Agency (ANP 2021).

Building and running undersea oil pipes to drain output so far away from the continental shelf (Menegaldo et al. 2009) becomes less economically viable, which is why there are 48 active FPSO/FSO of the 143 total active offshore production units in Brazil (ANP 2021). Due to the restricted storage capacity of FPSO/FSO, this system necessitates a complicated logistic framework to transfer treated crude oil. Production continuity depends on the design and implementation of intermittent relief activities, often known as offloadings. This procedure is broken down into the following stages:

i - *Approaching:* the tanker to the FPSO in a determined distance;

ii - *Mooring:* the two vessels with a robust link;

iii - *Connection:* of the offloading hose;

iv - *Pumping:* fluids from oil rig's tanks to the ship;

v - *Disconnection:* of the hoses and mooring links;

vi - *Departure*.

In the first phase, a shuttle tanker will approach the FPSO/FSO until it reaches the safe operating distance, ranging from the offloading station to the vessel's bow depicted by the Figure II.1, which ranges from 50 m to 150 m (depending on type of shuttle tanker). In the mooring stage the FPSO/FSO and the vessel are linked together with the mooring link, although according to the International Marine Forum guidelines of the Oil Companies (OCIMF 2018), the connection procedure may depend on the kind of vessel.

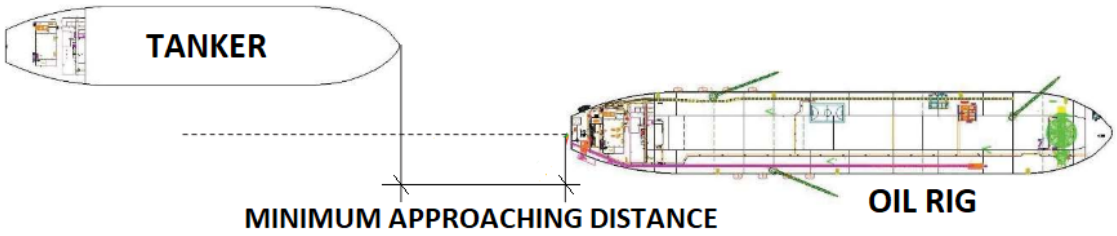


Figure II.1: Tandem approach scheme (elaborated by the author).

The operation on the vessel bow is performed via Bow Load System (BLS) for dynamic positioning vessels, which are a kind of vessel that can maintain its position by thrusters and satellite positioning. An air gun like the one shown in Figure II.2 or a modified firearm will be used to transmit a messenger line from the bow of the vessel to the production plant. The messenger line is a somewhat thin, light weighted rope, being reasonably easy to toss over a gap. The heavier line, warp or chain is connected to the messenger line and then it can be pulled across the gap. In mooring stage, the end of the messenger line is connected to the mooring link after it is received in destination. The tanker uses its machines to draw the entire system, fixing it at the conclusion of the mooring operation on a chain stopper. Support vessels may be needed for Dynamic positioning (DP) vessels depending upon the circumstances, visibility or degradation of the system, or if the DP tanker (OCIMF 2018) needs to operate in conventional mode.



Figure II.2: Line Throwing Apparatus tool (elaborated by the author).

The procedure is more complicated for conventional shuttle tankers, a kind of vessel which cannot maintain its position independently. Support boats are usually necessary and the procedure is done in the middle of the vessel, or the mid-ship. First, the LH approaches to the FPSO/FSO hull and the messenger lines is launched from the FPSO/FSO to the deck of the LH. The messenger line are connected to the mooring link. The crew attaches the mooring link on the LH, which carries it to the tanker. Once the LH is nearer, the crew of the tanker will toss another messenger line, and the boat's crew will use it to connect the mooring link. The tanker then pulls the mooring link and completes the mooring operation using its crane.

A Anchor Handling Support Vessel (AHTS) is necessary for the conventional shuttle tanker to pull the ship, maintaining its position, and also a special kind of pilot, called maneuver captain, to direct the AHTS maneuvers and efforts during operation. These processes and the requirement for resources

increase the danger, cost and restriction of offloadings with conventional tankers when compared to DP shuttle tankers. The Figure II.3 shows a simplified tandem mooring scheme of a offloading operational and a typical mooring link composition is also shown in Figure II.4.

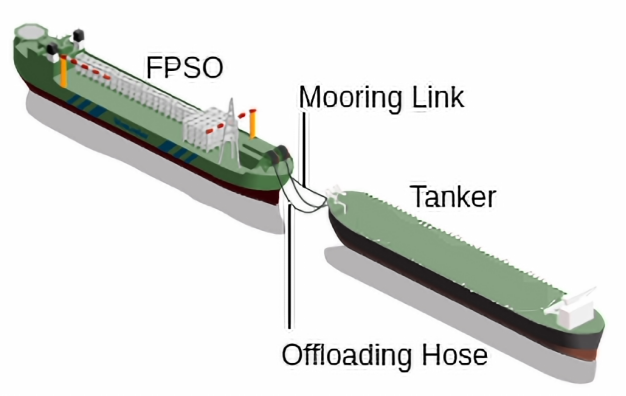


Figure II.3: Tandem mooring in offloading operation (Ramos et al. 2021).

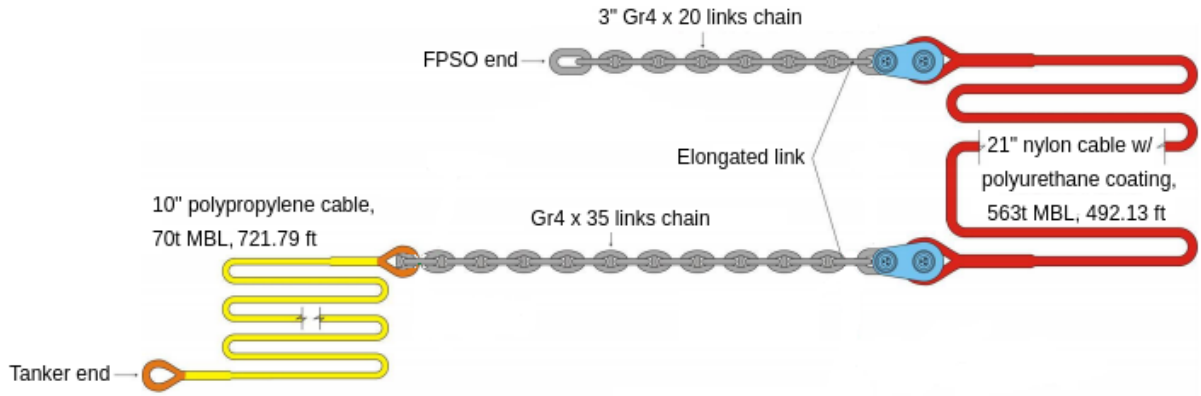


Figure II.4: Typical mooring link configuration (Ramos et al. 2021).

The offloading hose must be attached after mooring. Despite uncommon, it occasionally takes the messenger line to be launched again in the production facility with DP shuttle tankers operations. The line is now connected to the loading shaft end, on the *North Sea* Valve halter. The crane of the ship pulls the line and thus the hose. The finishing hose's connection *North Sea* Valve (NSV) is attached to the DP shuttle tanker's BLS automatically. For conventional tankers, the LH again approaches the FPSO/FSO hull, receives the messenger lines for the hose and pulls the messenger line and attaches the pitcher on its deck. The end of the hose, in this case, has no NSV but just blind flanges, since conventional vessels have no BLS. The LH takes the shaft towards the tanker and the tanker crew lift the messenger line connected to the offloading hose. The vessel pulls the hose with its crane and the crew removes its blind flange and connects it to the pipeline of the vessel, finishing the connection stage (OCIMF 2018).

Some leak testing are conducted after connection. If no leaks are identified, the pumping of the oil from FPSO's tanks into the vessel's tanks will commence. The hose, vessel and FPSO/FSO will

be disconnected after the whole volume is transferred. In this process, the BLS releases the NSV for the DP Shuttle tanker, with the FPSO/FSO using the offloading hose heel to recover the shaft. When the chain stopper releases the mooring links, a similar procedure happens where the FPSO/FSO crane retrieves the mooring links. In conventional mode offloadings, the LH gets close to the tanker's hull and the tanker crew tosses the messenger line to the LH's deck. The LH pulls the hose to its deck trough the messenger line and attaches it, carrying the hose back to the FPSO/FSO. The crew of the oil rig launches the messenger line to the LH, then it is connected to the hose and the FPSO/FSO utilizes its cranes to retract the hose trough the messenger line. The shuttle tanker leaves the FPSO and departs once it is released (OCIMF 2018).

Not only is the offloading operation complex but also the programming of logistical schedule of the vessels, because it needs to consider the correct distribution of transporting and support resources and the continued oil delivery for terminals, refineries and international clients without allowing tank top-up to the production platforms (that is, the maximum storage limits is reached by FPSO/FSO cargo tanks). Based on this backdrop, a smart system application to this process is a fruitful scenario, following the propensity of the oil and gas industry orientation to effectiveness, product quality and safety while minimizing both human labor and suppliers (Stavinoha et al. 2014).

II.2 Satellite Navigation

As described before, one of the operational stages in this proposed hybrid methodology is the first navigation through a calculated route based on satellite coordinates. When it comes to this kind of worldwide positioning technology, the general therm GNSS is used to describe a constellation of satellites that supply geospatial location information and measurements (Lechner e Baumann 2000). This information is used by several civil applications, such as mapping for general purposes, forest and environmental surveillance, topography, photogrammetry, and general navigation (Hein 2020). This technology was initially made available by the American Global Positioning System (GPS), but nowadays there are other satellite constellation global positioning systems available such as the Russian GLObal NAvigation Satellite System (GLONASS), European Union's Galileo Navigation Satellite System (Galileo), and the Chinese BeiDou Navigation Satellite System (BDS) (Hein 2020).

Regarding UAV, the satellite navigation essentially consists of a trajectory of waypoints, which is a sequence of geographic coordinates provided by Geographic Information Systems (GIS) databases, that the robot has to sequentially follow, keeping on track from the start to the end of the mission. The UAV Flight Control Unit (FCU) will correct the vehicle's inertial parameters in order to reach each waypoint, having the coordinates as setpoints and the continuous GNSS readings of the vehicle as to the controller's feedback. Thus, knowing the UAV geographic position and the target position, the controller will execute flight commands in order to fly to the desired waypoint, correcting the position

if the UAV deviates from the path (Ardupilot 2021). Figure II.5 represents a real mission executed by an UAV using autonomous GNSS navigation.

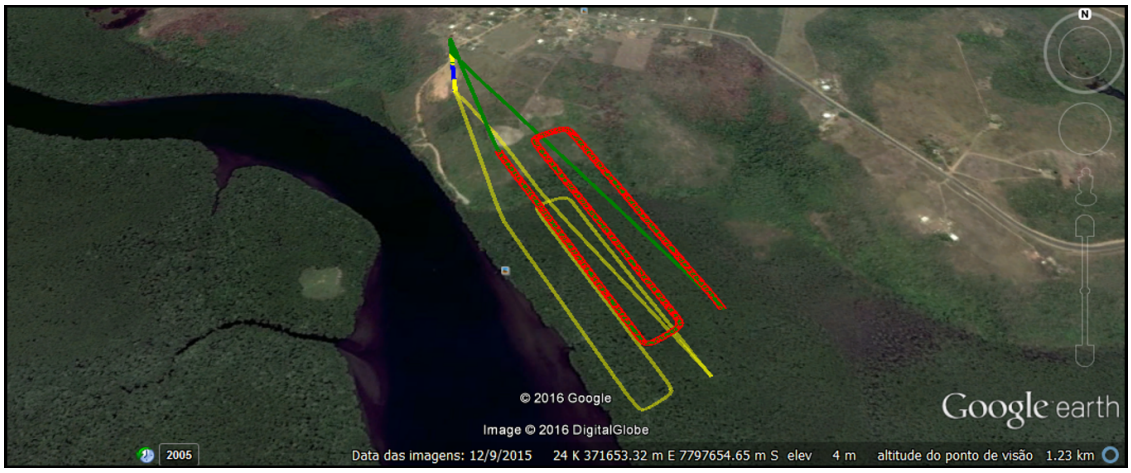


Figure II.5: Executed waypoint flight. The red color represent waypoints, yellow represent the projected trajectory and green represent the executed trajectory (elaborated by the author).

The GNSS satellites numbers and capabilities within a single constellation improved over the years. Also, they may be triggered using only one system or using different constellations, improving positioning precision (Pan et. al. 2017). Although simple GNSS positioning improved since its first civil application in 90's decade, it still presents a position error up to 10 m (Kaartinen et al. 2015) and may be susceptible to radio interference (Dovis 2015). Regarding this issue, some navigation systems may demand high positioning precision, and therefore resort only to simple conventional GNSS won't meet the application's requirements. Several methodologies are being applied to improve position precision on GNSS systems.

For single-point centimeter-precision, the Real Time Kinematics (RTK) and Post Processing Kinematics (PPK) are the mainstream of the technology. The RTK works by using a pair of GNSS Receivers with an internal radio link, therefore communicating with each other during measurements in the field. The base receiver, which stays static (stationary) at a known coordinate, sends positioning correction via radio to the mobile (or Rover), obtaining ambiguity fixation after a series of algorithms and calculations, based on the principle of triangulation and trilateration, such as represented in Figure II.6. The PPK system works the same way, but the position correction is performed after the rover and the base station measurements collection by post-processing algorithms. The limiting factor for using the conventional RTK system is related to the transmission range of radio waves (McMahon et. al. 2021), which depends, among other things, on the radio power and the topography of the area to be surveyed (Famiglietti et al. 2021).

In addition to GNSS-improved positioning methodologies, some authors use inertial navigation sensors to improve the satellite points, fusing position estimated by sensors with the position given by satellite. For example, (Zhang et al. 2018) used an adaptive Kalman filter to fuse velocity and position parameter to improve positioning data for a moving object, Melendez-Pastor et. al. (2017) reported

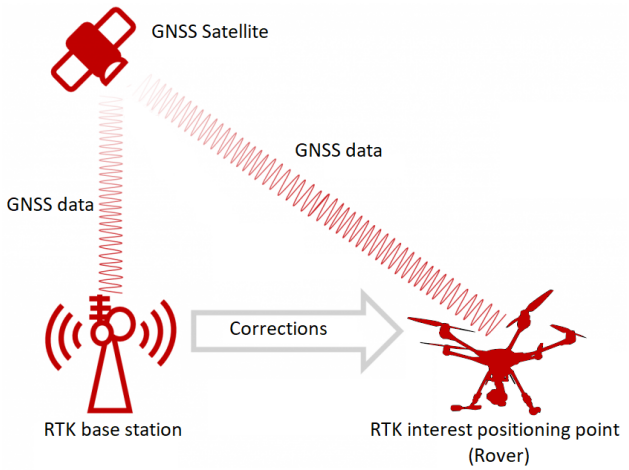


Figure II.6: RTK traingulation and trilateration representation (adapted from (OXTS 2021)).

the use of four-wheel speed sensors, a lateral acceleration sensor, and a steering wheel angle sensor of a car to estimate its position, and also fused it to the GNSS positioning with an EKF in order to improve localization data. Other sensors may also be fused with GNSS positionings, such as Light Detection and Ranging (LiDAR), Simultaneous Localization and Mapping (SLAM) and vision-based sensors as cameras, binocular cameras and IR sensors (Wang et. al. 2013), also improving the position estimation (Hsu 2018). The present work relies on both strategies by proposing an initial stage based on waypoint navigation, where the UAV will takeoff and position itself approximately perpendicular to the destination point, which is on a shuttle tanker's main deck, and a second stage where the UAV will precisely approach to that point, fusing vision and inertial navigation parameters to maintain trajectory.

II.3 Convolutional Neural Networks for Object Detection

The performance of Convolutional Neural Network (CNN) in image classification and other recognition tasks has considerably improved. Convolutional neural networks have continuously outperformed previous picture classification and identification algorithms since their inception in the early 1990s (Aghdam e Heravi 2017). In general, a CNN is a multilayer neural network that is specifically developed for 2D image classification. Each CNN layer is made up of several 2D planes, each of which contains a large number of individual neurons. The most basic construction of a CNN for object detection in digital images is shown in Figure II.7, which requires three operations: convolution, pooling, and output (Khan et al. 2018).

To create four feature maps in a convolutional layer, the input image is wrapped in four trainable filters. To construct four feature maps in the pooling layer, each 2x2 block in the feature maps is added, weighted, mixed with a bias, and sent through an activation function. All pixels from the pooling layer are combined into a 1D output vector by the fully connected layer (Camacho 2018). The convolutional

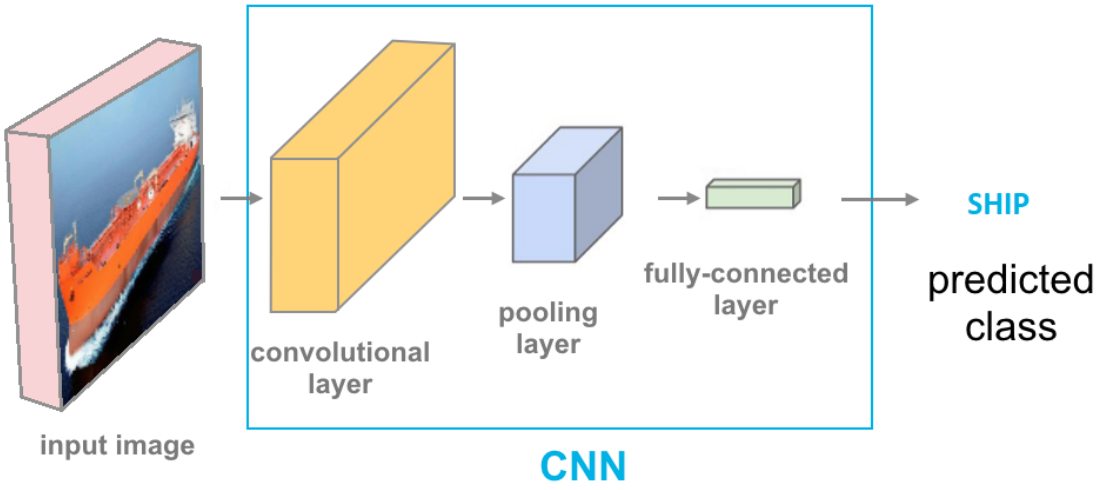


Figure II.7: Basic CNN for object detection architecture (adapted from (Camacho 2018)).

layer's feature map is defined as:

$$x_j{}^l = f(\sum_{i \in M} x_j{}^{l-1} \circledast k_{ij}{}^l + b_j{}^l), \tag{II.1}$$

where $x_j{}^l$ is the j^th feature map in the l^th layer, f is the activation function and M is the number of feature maps in layer $l-1$. The operation $x_j{}^{l-1} \circledast k_{ij}{}^l$ is the convolution between the map of i^th feature in layer $l-1$, represented by $x_j{}^{l-1}$, and $k_{ij}{}^l$, which is the kernel core between the i^th feature map in layer $l-1$ and the j^th feature map in l^th layer. Finally $b_j{}^l$ is the bias for the j^th feature map in the l^th layer (Chu e Krzyak 2014).

The image as a whole, as well as the feature maps from different kernels, is convoluted in convolutional layers (Camacho 2018; O'Shea e Nash 2015), resulting in a slew of new feature maps. The weight sharing method in the same feature map minimizes the number of parameters that the network must analyze, and the local connection learns correlations between surrounding pixels, enhancing object positioning evenness. This last benefit is crucial in pattern recognition because an object in an image is the same no matter where it is (O'Shea e Nash 2015).

Pooling layers are considered translation invariants, as they take into account neighbor pixels in their calculations, as similarly occurs in the convolutional layers. They are used to reduce the size of feature maps and the number of parameters, with average pooling and max pooling being the most commonly used. Finally, the fully connected layers usually come after the last pooling layer and convert, through multiple connections, a 2D feature map to a 1D feature map. These layers work as a final and traditional classifier, acting as a classic neural network with the majority of the overall network parameters (Chu e Krzyak 2014).

In general, there are two steps of training the CNN: forward and backward. Following the convolution

and grouping phases, the image's key properties will be extracted, resulting in an output prediction that will be compared to the actual output (i.e., ground truth). The prediction inaccuracy, which is the loss cost, is calculated using this output forecast. The backward stage now uses chain rules to calculate the gradients of each parameter depending on the loss cost calculated by the loss function. All parameters have been adjusted based on the gradients, and the process can now proceed forward. Learning can be terminated after a certain number of forward and backward cycles, usually when a preset loss cost is met (Chu e Krzyak 2014).

The You Only Look Once version 3 (YOLOv3) convolutional neural network was used in this study. The versatility, ease of training, known results evaluation metrics, and credited detecting speed all contributed to this decision (Choi et al. 2019). Based on YOLOv3, the CNN, namely YOLOff, was developed to detect the ship and its regions (i.e., bow, midship, and stern), as presented in (Gonzalez et al. 2020). Unlike the general structure shown, the YOLOv3 structure is simply made up of convolutional layers, with a 2D convolution layer serving as the output layer to downsample the image, fulfilling the same function as a fully connected layer without the loss of low-level features. Figure II.8 presents the structure of the YOLOv3 (and therefore the YOLOff as well) used in this work.

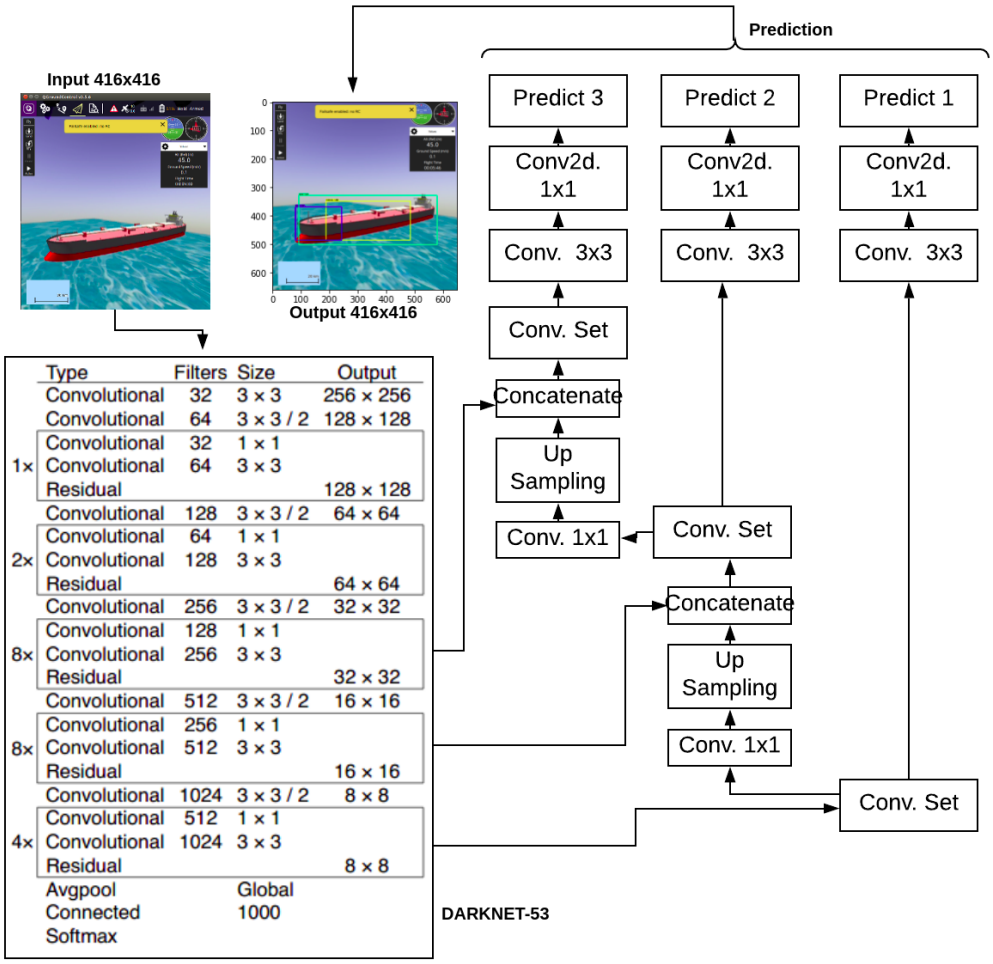


Figure II.8: YOLOv3 convolutional neural network structure (adapted from (Redmon e Farhadi 2018).)

In fact, YOLOv3 detects utilizing $(1, 1)$ detection kernels on feature maps in three distinct scales (exactly given by downsampling the dimensions of the input picture by 32, 16, and 8 respectively) and three separate outputs in the network's structure, concatenating all detections in one, as represented in Figure II.8. The detection kernel has the structure $(1, 1, (B \cdot (5 + C))$. B is the number of bounding boxes a feature map cell can predict, C is the number of classes, and B is the number of bounding box characteristics (the top left corner x and y coordinates, the width, and height of the bounding box) and one object confidence p. With four classes (ship, bow, midship, and stern) and three bounding boxes in YOLOff, the kernel has a $(1, 1, 27)$ dimension. This kernel generates a feature map with the same height and breadth as the previous feature map, as well as detection properties along with the depth as mentioned previously (Redmon et al. 2016; Redmon e Farhadi 2018).

All input Red, Blue, and Green (RGB) pictures are scaled to size $(416, 416, 3)$. The 82^{th} layer is the initial detection. The picture is taken down by the network in the first 81 levels, which results in a rise of 32 in the 81^{th} layer. The resulting feature map is $(13, 13)$, because the picture has a dimensions of $(416, 416)$. The $(1, 1)$ detection kernel makes the initial detection in that layer, giving us $(13, 13, 27)$ detection characteristics. The feature map from the 79^{th} level is then sampled using a couple of convolutional layers by 2 to $(26, 26)$. This functional map is then linked to the layer 61 feature map. Then a couple of $(1, 1)$ convolution layers is again put under the combined feature maps to merge the features of the previous layer (61). The layer 94^{th} then detects the second and gives a $(26, 26, 27)$ detecting map. A similar method is again performed where the 91^th layer feature map is treated to only a few convolutionary layers before it is combined with the layer 36 feature map. As previously, many $(1, 1)$ layers are used to merge the information from the preceding layer (36). The 3^{rd} is detected at a layer of 106^{th} and the result is a $(52, 52, 27)$ scale feature. Figure II.9 exemplifies the first detection with the $(13, 13)$ feature map (Martinez-Alpiste et al. 2021).

Just like with other object detectors, the characteristics of the convolutional layers are provided to a classifier that predicts the detection (coordinates of the bounding boxes and the class label). Each cell of the feature map is supposed to forecast the item through one bounding box if the center of the object falls inside the receptive field of that cell, assuming that only one bounding box detects any given object. First, it must be determined which cells belong to the bounding box. The cell (on the input picture) that contains the center of the object's base truth box is then picked as the predictor for the object. In Figure II.9, it is the light green cell that contains the center of the yellow ground truth box. The coordinated cell is allocated to the object detection on the feature map (in this case, the ship). Now, three bounding boxes may be predicted (Redmon e Farhadi 2018).

The YOLOff model is shown in Figure II.10 with three anchor boxes. The picture is re-scaled by a factor of 32 from an original RGB image with dimensions $(416, 416, 3)$, creating a $(13, 13, 3, 9)$ matrix, where 9 indicate each bounding box length (5 bounding box parameters plus 4 classes to identify)

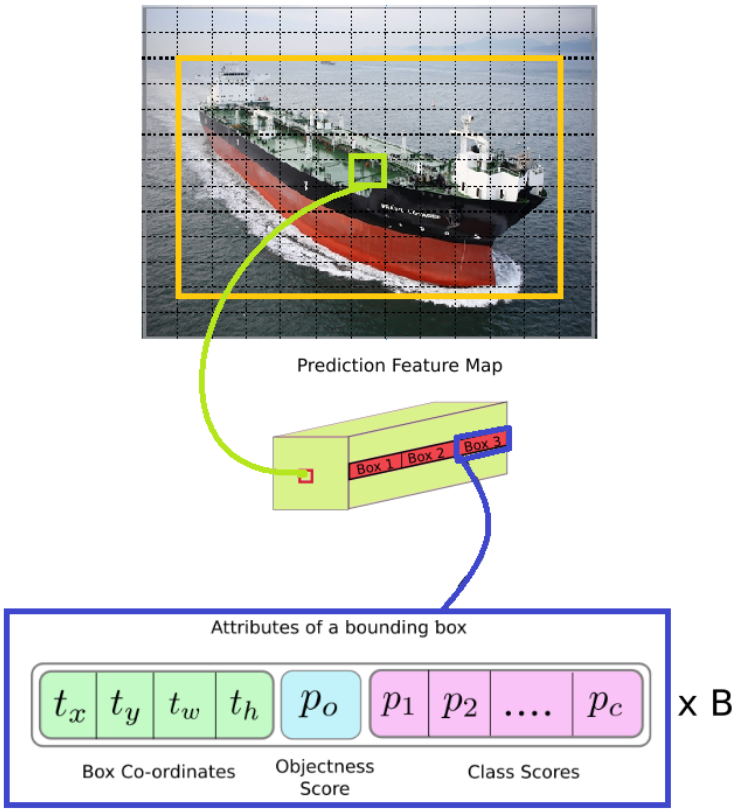


Figure II.9: Example of YOLOff detection with the 13x13 feature map (adapted from (Balsys 2019)).

(Redmon e Farhadi 2018).

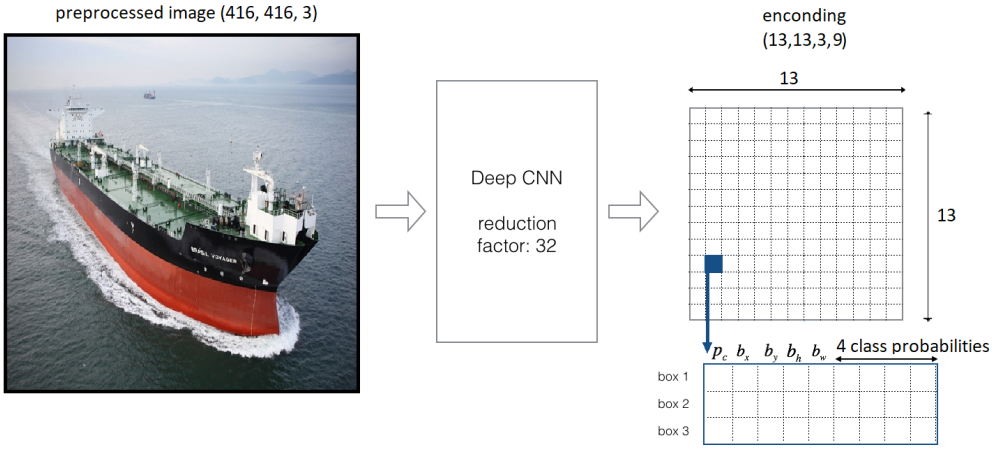


Figure II.10: Basic YOLOff detection model (adapted from (Balsys 2019)).

If an object's center or midway is placed in a grid cell, the grid cell will detect it as previously mentioned. Three anchor boxes are used to coding information on three boxes for each of the $(13, 13)$ cells. The anchor boxes have not box and class probabilities but are determined by their width and height solely. The picture is flat in a 2D array and converts a dimensions of $(13, 13, 3, 9)$ in $(13, 13, 27)$. For each box (of each cell) a product is calculated to extract a chance that the box includes a specific type of object (or class), according to Figure II.11 (Redmon e Farhadi 2018).

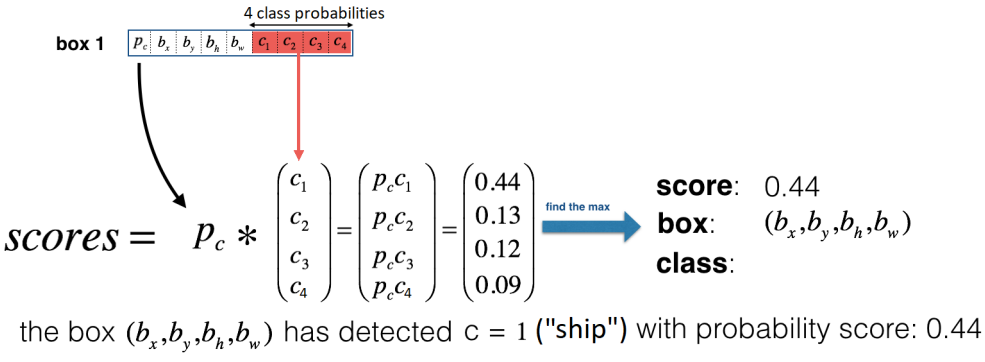


Figure II.11: Box class probability calculation (adapted from (Balsys 2019)).

Therefore, the maximum probability score is established for each of the $(13, 13)$ grid cells by taking max in both the three anchor boxes and various classes. When each bounding box has a class, it is aggregated by a K-Nearest Neighbors (KNN) algorithm into a cluster, resulting in the detection of the same item by many bounding boxes. The box is filtered to exclude boxes with class probability scores below an established threshold and then a non-max deletion approach is used to reproduce the resultant boxes, which only results in the highest score box around the intended identified item (Martinez-Alpiste et al. 2021).

In training, the ground truth box is used to compare the detected object within each epoch, in a way the class probabilities are altered by weights in the learning process. The boxes overlapping the ground truth bounding box have the respective object's class probability privileged and the other classes are penalized in the backpropagation phase. All the detection process is repeated at the end of the forward phase, comparing the detected objects to the ground truth again until the loss becomes acceptable, resulting on a You Only Look Once (YOLO) network trained to detect the objects within the provided classes (Redmon et al. 2016; Redmon e Farhadi 2018). These objects will be used by the controller to estimate the UAV's heading and maintain it fly in direction of the destination vessel (Zhang et al. 2019).

II.4 Kalman Filter

The Kalman filter is an iterative computing approach for calculating unknown variables observed on the basis of time associated with measures and uncertainty between measurements. The relatively easy operation, implementation, and low processing power required to make estimates, alongside the vast range of applications where this approach may be utilized, are one of the primary advantages of such algorithms (Kim e Bang 2019).

Kalman filters are used to estimate status in the state space format on the basis of linear dynamic systems. The process model defines the state's development from two instant observations at successive times. The role of the Kalman filter is to provide an estimate of a variable x at a time k, given the initial estimate of x, the series of measurement, z, and the information of the system described by the

state transition, control input, measurement, covariance matrices. Although the matrices of covariance are meant to reflect statistical noises, they're not Gaussian in many practical applications or they're not known as real statistical noises. The covariance matrices are therefore generally utilized to adjust to the user's required performance as tuning parameters (Kim e Bang 2019).

The Kalman filter algorithm is divided into two stages: *(i)* prediction and *(ii)* update. The predicted state is determined in the prediction stage by summing the product of control input and control vector therm to the product between the latest updated states and the transition matrix. The state error covariance is computed at this stage, which encrypts the error covariance that the filter "believes" the estimated error possesses (Chui e Chen 2017).

The residual measurement, also known as innovation, is the difference between the real measurement and the estimated measurement, and it is determined first in the update step. By multiplying the predicted state by the measurement matrix, the filter calculates the current measurement. The residual is then multiplied by the Kalman gain to offer a correction to the first filtering stage's predicted estimate. The updated state estimate is then obtained, and the Kalman filter produces the updated error covariance, which is then utilized in the next time step to repeat the process to yield the next estimate. It's worth noting that the updated error covariance is lower than the predicted error covariance, implying that the filter is more confident in the state estimate after using the measurement in the update step. This way, the Kalman filter can predict states with more accuracy, and these variables can be used as input to an anticipatory controller to achieve robustness and smoothness (Chui e Chen 2017).

An initialization stage is also required for this method to work. The first guess (or observation) of the state estimation and the initial guess of the error covariance matrices are required as starting values. These covariance matrices, as well as the starting observation, are critical in achieving the filter's intended performance. In practice, a field rule known as "initial ignorance" is used (Mohan et al. 2015), which determinate that in order to achieve faster convergence, the user should pick a large initial state error covariance. Once that is done, a Kalman filter may be implemented by completing the prediction and update phases for the following time steps after the estimates have been initialized. However, all the processes described so far apply only to linear models of process and measurements, which is a problem when it comes to real applications since the real-world processes can't be described only by linear models.

To cover this issue, the EKF is a technique for efficiently dealing with such nonlinear models. The EKF has being applied to many real-time applications, such as inertial navigation systems as described in the previous section by Melendez-Pastor et. al. (2017), Wang et. al. (2013), and Jiang et. al. (2021), because it is computationally cheaper than other nonlinear filtering methods such as point-mass filters and particle filters (Zhang et al. 2018). The EKF is a nonlinear variant of the Kalman filter that uses the Jacobian matrix, which is the first-order partial derivative of a vector function with respect to

a vector, aiming to linearize models about a current estimate. Approximating the nonlinear function as a tangent line at the place in question on the function by a small-time period between two consecutive predictions is a straightforward way to linearize it. Doing this, the models are linearized to the current estimate, then the filter algorithm can be used similarly to the linear Kalman filter described before.

One of the most interesting features of the linear Kalman filter (and therefore the EKF) is sensor fusion. Sensor fusion is defined as the capacity to integrate information from many sensors to infer anything about a state component. The gain of doing this is to mathematically reduce the values within process noise and measurement noise covariance matrices, obtaining a more assertive prediction of the state measured by the combination of the sensors (Zhang e Liao 2017). Supposing an example of a simplified system of a UAV with the following observation model:

$$\mathbf{z}_k = \mathbf{H}\mathbf{x}_{k-1} + \mathbf{v}_k \tag{II.2}$$

where $\mathbf{z}_k$ is the measurement vector in the time k, H is the measurement matrix, $\mathbf{x}_{k-1}$ is the state vector in time $k-1$ and $\mathbf{v}_k$ is the measurement noise vector. The example's sensors measurements can be described as:

$$\begin{bmatrix} \text{GPS}_k \\ \text{barometer}_k \\ \text{compass}_k \end{bmatrix} = \begin{bmatrix} f(\text{position}) & 0 & 0 \\ 0 & f(\text{altitude}) & 0 \\ 0 & 0 & f(\text{heading}) \end{bmatrix} \begin{bmatrix} \text{position}_k \\ \text{altitude}_k \\ \text{heading}_k \end{bmatrix} + \mathbf{v}_k \tag{II.3}$$

being f the sensor's functions that determine the state by each sensor reading. This way, this UAV model for a simple EKF will use GPS readings to predict the vehicle's position, a barometer to predict altitude, and a compass to predict heading. Supposing the installation of a sonar sensor to also obtain altitude readings, the new system's model would be:

$$\begin{bmatrix} \text{GPS}_k \\ \text{barometer}_k \\ \text{compass}_k \\ \text{sonar}_k \end{bmatrix} = \begin{bmatrix} f(\text{position}) & 0 & 0 \\ 0 & f(\text{altitude}) & 0 \\ 0 & 0 & f(\text{heading}) \\ 0 & f(\text{altitude}) & 0 \end{bmatrix} \begin{bmatrix} \text{position}_k \\ \text{altitude}_k \\ \text{heading}_k \end{bmatrix} + \mathbf{v}_k \tag{II.4}$$

In this way, the model will then consider two sensor readings to altitude, and the measurement noise vector will also be incremented by a element representing the noise of the new sensor. Within the filtering steps, the new sensor will improve altitude estimation by diluting the uncertainty of the altitude state observation. This work will use this technique to fuse two camera heading estimation with the compass readings, therefore improving also positioning estimation and providing robustness to the controller on inertial navigation assisted by computer vision, as it will be detailed in Chapter III.

II.5 Related Works

The task was split into three phases to transport the line from the oil rig to the shuttle tanker vessel or vice versa. Chapter III explains the motivation and methodology adopted, but in summary the initial phase consisted of the operator configuration of the final point, or the delivery spot, the takeoff and the autonomous navigation to a position at which the UAV is positioned approximately perpendicular to the delivery point, separated by a distance also configured by the operator.

Approaching the destination vessel and determining the final delivery location are the second and third phases, respectively. At this step, the UAV will start flying towards the cable delivery point area, guided by computer vision (Ramos et al. 2021). The camera image frames from the UAV will be fed into the YOLOff CNN that was introduced earlier (Choi et al. 2019). The YOLOff object detector is in charge of identifying the target ship as well as its general areas (i.e., bow, mid-ship, and stern). In addition to the related work already mentioned in Chapter I.1 regarding similar applications to the proposed in this research work, it is important to refer to some other publications regarding GNSS, computer vision, inertial navigation and sensor fusion with Kalman filters.

Related to satellite autonomous navigation, the agriculture, mapping, and environmental monitoring sectors are playing an important role in applying precision flight technology to UAV. The RTK and PPK positioning systems applied for UAV flight on remote environments are analyzed by (Tomatík et al. 2019), being able to accomplish mapping missions with an incredible 10 cm to 20 cm maximum deviation from the planned trajectory. Also using RTK and integrating it with Ultra-Wideband (UWB), (Gryte et al.) proposed a robust solution for possible satellite dropouts during UAV navigation, reaching flight precision under 1 m of deviation from the planned waypoints as well.

Also evaluating precision applied to sand beaches topography mapping, (Casella et al. 2020) attested the high precision of Global Navigation Satellite System-RTK (GNSS-RTK). Finally, it was evaluated a methodology to avoid GPS restrictive areas for flight planning and, if these regions can't be avoided, a methodology based on near known structures positions to help navigation in case of satellite missing (Zimmermann et al. 2017), similar to the proposed configuration of the approximate messenger line delivery point.

Despite its high precision, the RTK-based flight demands very expensive sensors and is vulnerable to satellite reception failures in the proposed application, mainly due to the fact that oil rigs and ships' surroundings may have high interference caused by the communication systems of the vessels. Visual-based inertial navigation on a similar environment to the proposed application is presented by (Durdevic et al. 2019). The authors addressed a simulation of an autonomous UAV system that detects wind turbines in offshore wind farms using computer vision and used the detected object to approach and perform visual surveillance of the turbine. The project however didn't present fail-safe methods if

the object is not detected, neither control strategies to improve precision.

In (Qin e Wang 2019), it is presented a visual object tracking methodology to determine the tracked target position on image. They used EKF to deal with lack of detection issues, which may be caused by obstacle occlusion of the target during a short period or even background color interference, a problem that also may affect the proposed methodology on the present work. This project was tested on an onshore controlled environment, where the UAV flies directly above the target (a small RC car) and the objective is to correct its inertial position to keep the target on the center of the image. The system worked even when the small tracked object passed under a table because the EKF could predict trajectory for a short period while the detection was not performed. The system would have failed if the object changed its trajectory under the table.

Concerning the proposed methodology in the present work, the goal is to get close from the ship, ensuring robustness to the yaw control if the object detection fails or the UAV experiences wind drag very similar to the work in (Qin e Wang 2019), thus an abrupt change in detected object position is very unlikely to happen. Finally, Chuang et. al. (2019) showed a UAV inertial positioning method based on a tracked target coordinates using computational vision. This is very alike the proposed final object detection, where the final adjustments on the UAV inertial pose will be performed based on the marker detection.

Computer vision methods are used to maintain the desired region approximately in the center of Field of View (FOV), as the UAV flies forward. To guarantee flight precision, the yaw angle is estimated by the YOLOff readings, by a Lucas-Kanade optical flow algorithm applied to the camera's image frames and by the UAV's compass, fusing the three yaw readings with an EKF and using it to predict the UAV's yaw, in case that some reading fails. The third stage consists of detecting a marker symbolizing the final and precise cable delivery position. This marker can be painted in the ship, placed on it for the operation, or can be a sign held by an operator, for example. The marker can be a set of fiducial markers (Garrido-Jurado et al. 2014) or a Quick Response (QR) code.

Regarding visual object detection focusing on ships, most of the research data are focusing on satellite images or stationary cameras on ports. Related to the present work, Zhang et. al. (2017) showed a ship detection methodology for non-stationary platforms (mounted on ships and buoys, for example). Their work is based on cosine discrete transform to segment the horizon line, and, therefore, to detect objects "floating" on water's surface. Even though the results presented to be a fast ship detection system and optimized for cameras mounted on moving platforms, it doesn't detect the ship's type and its regions and it may be confused by waves and marine fauna.

About VI navigation, Santoso et. al. (2017) reviewed this technology for several applications in distinct areas, concluding at the time that this strategy is inexpensive yet accurate and robust flight methodology for UAVs. The authors evaluated the GPS and IMU sensors fused with visual sensors such

as monocular and stereo cameras, optical flow sensing, 3D ranging cameras, and infrared cameras data, producing smooth readings and predictions for flight controller based on altitude, velocity, positioning, and yaw rate.

An example of EKF sensor fusion with vision systems with modeling similar to the present work is described by Kelly et. al. (2008). The authors fused IMU velocity and heading readings and visual odometry (a technique similar to optical flow to estimate velocity within successive camera frames) to predict the UAV position from the takeoff point, therefore controlling its desired trajectory. The result was compared to the GPS traditional navigation, obtaining a precision (final position mean absolute error) of 1.65 m.

Also about VI navigation, (Driessen et al. 2018) presented an EKF model which fuses accelerometer, magnetometer, and gyroscope readings from the IMU with sonar sensor and optical flow velocity measurements from the camera to correct and predict (x, y, z) velocities and *(roll, pitch, yaw)* angles on the respective axis related to the UAV's body using bias compensation to correct sensor's drifting, and, therefore, improving the positioning of the UAV with the controller. Comparing the implemented UAV VI navigation with a motion capture validation system, the authors obtained a maximum RSME of 0.3545 m regarding the position, 0.0442 m/s in velocity, and $0.1089°$ in angle (specifically the pitch). The present work also uses the EKF modeling basis like (Driessen et al. 2018), but with a simpler automatic sensor drifting compensation, as presented in the section Methodology III.

In order to control a UAV attitude during flight, (Marina et al. 2012) proposes the adoption of the Unscented Kalman Filter (UKF), a technique similar to EKF regarding optimization of states estimation and prediction with similar computational cost. The method is responsible to fuse data from IMU sensors in a model to estimate the vehicle's heading, thus controlling it to navigate. The usage of a visual-based roll angle estimation based on horizon line identification is an interesting feature of the method.

This estimation, however, is only used as a ground-truth reference to evaluate the prediction using the IMU sensors, obtaining small errors in attitude angles compared to the independent sensors used for validation (GPS velocity for yaw and camera for roll). The authors themselves cited the necessity to use those independent sensors in the Kalman Filter modeling as a proposal for future works in order to improve the attitude estimation robustness. Although simpler, the present work already covers this proposal by fusing IMU readings (yaw) with similar camera angle estimation.

The authors of the present work also refer to (Xu et al. 2021) paper, presenting research using IMU sensors fused with a binocular 3D camera visual odometry to predict and improve position estimation. The authors used a technique of a loosely coupled EKF, which considers the camera as a black-box model, only using its already computed position estimation as an observed state input to the EKF, the same strategy adopted in this work for yaw estimation with a camera. The authors presented an

accuracy of 0.05 m in a simulated environment and obtained an accuracy of 0.1 m in an experimental test.

In fact, the main goal of the present work is a precise strategy to reach a specific point on an open field using a VI navigation framework. The method is validated by both simulation and experiments. As simple GNSS navigation systems would be vulnerable to interference from the ship and the production facility's communication and positioning systems, besides being expensive solutions. The strategy proposed here is a yaw correction controller, where the yaw rate is constant since the flight height is supposed fixed, as will be seen in Chapter III. The EKF fuses the yaw readings of the IMU/compass of the UAV with the camera yaw estimation with optical flow yaw from the Lucas-Kanade Algorithm (Bruhn et. al. 2005), predicting the *next* yaw reading and using it to preview how the UAV is deviating from the desired region, correcting it and maintaining it on course. Finally, the present work also shows an economic feasibility study and the financial attractiveness of this project in a real industrial scenario. The related works summary is presented in Table II.1.

Table II.1: Related works summary.

Research	Autonomous Navigation	Vision Assisted	EKF Assisted Control	Offshore Application	Small Cargo Transport	Economic Study
Proposed Methodology	Yes	Yes	Yes	Yes	Yes	Yes
(Kotug 2018)	No	Yes	No	Yes	Yes	No
(Frederiksen e Knudsen 2018)	No	No	No	Yes	Yes	No
(Kim et. al. 2019)	No	No	No	No	Yes	Yes
(Tomatík et al. 2019)	Yes	No	Yes	No	No	No
(Gryte et al.)	Yes	No	Yes	No	No	No
(Casella et al. 2020)	Yes	No	Yes	No	No	No
(Zimmermann et al. 2017)	Yes	No	Yes	No	No	No
(Durdevic et al. 2019)	Yes	Yes	No	Yes	No	No
(Qin e Wang 2019)	Yes	Yes	Yes	No	No	No
(Chuang et. al. 2019)	Yes	Yes	No	No	No	No
(Zhang et. al. 2017)	No	Yes	No	Yes	No	No
(Kelly et. al. 2008)	Yes	Yes	Yes	No	No	No
(Driessen et al. 2018)	Yes	Yes	Yes	No	No	No
(Marina et al. 2012)	Yes	Yes	Yes	No	No	No
(Xu et al. 2021)	Yes	Yes	Yes	No	No	No

Chapter III Materials and Methods

As stated before, the mission of reaching the messenger cable's delivery point to transfer it from the platform to the FPSO, or vice versa, is divided into three stages. The initial stage consists in an automated route with waypoint-feedback based on GNSS. As detailed in III.1, the operator must enter some initial configurations and the UAV will automatically deploy and execute a route of a series of waypoints globally positioned. After reaching the final waypoint, the UAV then will approach to its desired destiny using a vision-assisted inertial navigation methodology.

The control strategy adopted in this work considers that the UAV begins its flight with an orientation (yaw) perpendicular to the destination ship's heading, in a way that the destination ship is in the FOV the camera's image. The strategy considers a stable flight height and that the UAV flies with an approximately constant speed. To get closer to the destination, velocity commands (v_x, v_y) will be imposed on UAV's (x, y) axis referred to its body, as presented in Figure III.1. The (v_x, v_y) velocities depends on orientation (yaw), being described by $v_x = v\cos(yaw)$ and $v_y = v\sin(yaw)$, with the UAV's velocity v referred to the ground (inertial referential) measured by the IMU sensor of the FCU.

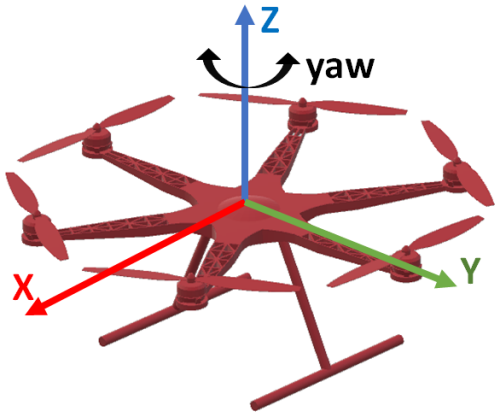


Figure III.1: UAV's rigid body simplified illustration (elaborated by the author).

The local to deliver the messenger line is defined by the operator. It depends on the local that the mooring or connection will be made (usually bow or mid-ship). To maintain the UAV's flying directly to the destination ship, a YOLOff CNN object detector was trained using real-life ship images, detailed in Subsection III.2 of this Chapter. The object detector YOLOff is also used to estimated UAV's yaw, so does the optical-flow algorithm based on the Lucas-Kanade method (Yedjour 2021) applied to camera image frames. Those yaw estimations are fused with the yaw measured by the UAV's compass by an

Extended Kalman Filter, producing a precise yaw prediction which is used in the velocity controller, and also giving robustness to the controller in case the destination region is not detected. The orientation estimate from the image frames, the EKF modelling and the controller are detailed in Subsection III.3.

The UAV will continue until the safety distance limit is reached or the marker is detected, as detailed in Subsection III.4. The distance between the UAV and the delivery point is calculated based on the GPS coordinate of both objects (the first one is configured by the operator at the beginning of the operation), an estimate which is inaccurate, in general. Once the UAV is close enough to the destination vessel, it needs to detect a marker symbolizing the final and precise cable delivery position. This marker can be painted in the ship, placed on it for the operation, or can be a sign held by an operator, for example. If the marker is detected, the drone can make the final approximation and deliver the cable oriented by computer vision algorithms. If not, the UAV will fly around (maintaining a safety distance configured by the operator) until it finds the marker or the operator cancels the delivery operation.

Once the operation is finished, either by successfully delivering the cable or by cancellation at any stage, the UAV will automatically return to the deploy point and land. The designed controller also has a series of fail-safe protocols that will make the UAV return and land on the deploy point, such as a low battery, loss of communication with the telemetry station, and loss of communication with the ground station controller. The operation flowchart is shown in Figure III.2.

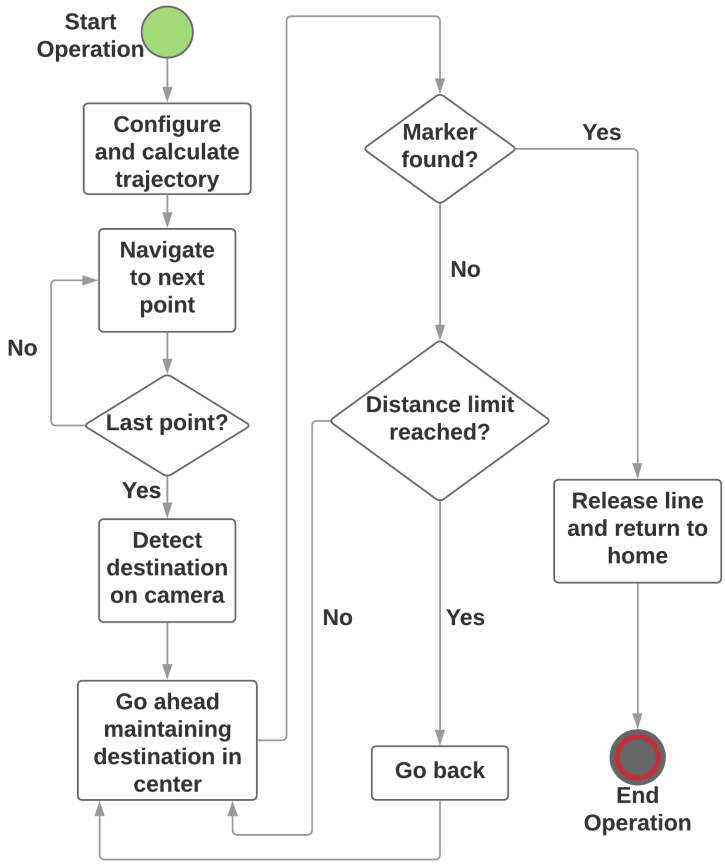


Figure III.2: Operation flowchart (Ramos et al. 2021).

III.1 Initial Waypoint GNSS Navigation

In the first step, the operator must configure the UAV's offboard controller with the delivery point GPS coordinates and the region of the vessel that this point is located. At this point, the user must also inform where is the antenna that provided the position of the destination ship, the vessel's length (in meters), the vessel's heading angle (in degrees), the flight height, and the desired distance between the ship and the vehicle at the end of this mission's stage, both in meters. The trajectory calculation reads the coordinates of the takeoff point through GPS, making this the origin of a three-dimensional Cartesian system (x-axis oriented towards the east, y-axis oriented towards magnetic north, and z-axis being altitude). The system receives the information and designs a trajectory in the form of a straight line, as the red line in Figure III.3. The reason for the trajectory shape is to avoid gas escapes points and classified areas around the vessels.

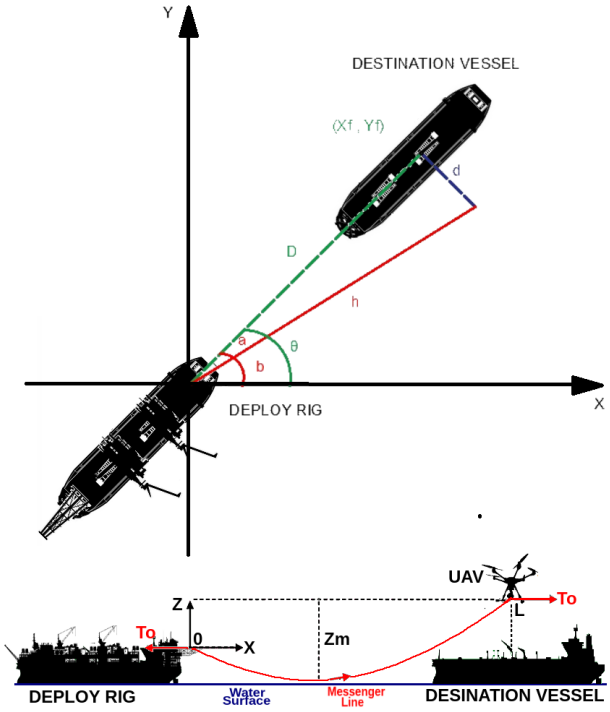


Figure III.3: Linear trajectory (Ramos et al. 2021).

The points of this trajectory are the x and y coordinates (in meters) regarding the takeoff point, and the z value is the flight height in meters. Thus, based on (Karney e Deakin 2010), given the destination coordinates set by the operator and the takeoff coordinates provided by the GPS, it is possible to calculate the distance D between the takeoff point and the arrival point:

$$\begin{aligned} D &= R \cdot \arccos(\sin(\mathsf{Lat}_i) \cdot \sin(\mathsf{Lat}_f) \\ &\quad + \cos(\mathsf{Lat}_i) \cdot \cos(\mathsf{Lat}_f) \cdot \cos(\mathsf{Lon}_i - \mathsf{Lon}_f)) \end{aligned} \tag{III.1}$$

where Lat and Lon are the GPS coordinates (in radians) and the notations "i" and "f" symbolize start (i.e., takeoff location) and destination, respectively. The parameter R symbolizes the Earth's radius, admitted as 6.373×10^6 m. Equation (III.2) gives the azimuthal direction θ (in degrees) of the destination from the takeoff point.

$$\theta = \arctan \frac{\Delta_{(Lon)}}{\Delta_{(\phi)}}, \tag{III.2}$$

where

$$\Delta\phi = \log \left[\frac{\tan(\frac{\mathsf{Lat}_f}{2} + \frac{\pi}{4})}{\frac{\mathsf{Lat}_i}{2} + \frac{\pi}{4}} \right] \tag{III.3}$$

$$\Delta lon = |\mathsf{Lon}_i - \mathsf{Lon}_f| \tag{III.4}$$

The line end (x_f, y_f) is approximately the destination vessel's point where the UAV must deliver the messenger cable. This coordinate is informed to the control node and serves as feedback to measure the UAV's distance to the target in step 2. Thus, the trajectory calculation publishes this route to the controller with the points (x, y), the flight height at each point (z), and the robot's orientation (yaw) at each point. The main objective is to maintain the destination vessel in the UAV's Field of View (FOV) continuously. Thus, when the robot reaches the flight height, the value of θ is set up into the yaw controller. After this, the UAV starts the trajectory maintaining the destination on the center of the field of view. The yaw angle varies $\pm\ 90^o$ (depending on the direction of θ) along the trajectory. Thus, the UAV orientation will be approximately perpendicular to the destination point at the end of this stage. During navigation, it will always be aligned with the vehicle's line of sight. The coordinates (x_f, y_f) of the destination point are obtained using:

$$\begin{aligned} x_f &= D \cdot \sin\theta \\ y_f &= D \cdot \cos\theta \end{aligned} \tag{III.5}$$

Thus, the trajectory is described by points (x, y) that belong to the line h , according to Equation (III.6).

$$h : y = x \tan b \tag{III.6}$$

With $x \in [0, h\cos(b)]$ and $y \in [0, h\sin(b)]$, where

$$a + b = \theta \tag{III.7}$$

$$a = \arctan\left(\frac{d}{h}\right). \tag{III.8}$$

and

$$h = \sqrt{D^2 + d^2}. \tag{III.9}$$

Notice that, for this research proposed operation, it was developed only flight control methodology. However, for an initial viability analysis for carrying the thin messenger line, the cable's catenary is considered due to its geometry related to the tension applied to the line, therefore the payload that the UAV can carry. The project's concept was designed to avoid the messenger line touching the water for the robot operation safety, as shown in Figure III.3. The purpose of those assumptions is to previously estimate if the flight methodology would be applicable and to what class of UAV.

Based on Det Norske Veritas (DNV) recommended naval towing practice (DNV 2020), the minimum point z_m of the catenary, in meters, can be described as:

$$z_m = \frac{L}{8}\left(\frac{wL}{T_0}\right)\left(1 + \frac{T_0}{EA}\right) \tag{III.10}$$

The parameter L is the distance between takeoff point and UAV, w is the fluctuated weight of the messenger line, E is the elasticity modulus of the line, A is the section area of the line, and T_0 is the traction applied to the messenger cable. This way, once the operator configures other parameters, the system can provide approximate traction that has to be applied to the messenger line to prevent it from touching the water, which would be a risk. The system can also predict if the operation is safe, given the payload capacity of the UAV. Notice that the messenger line is a very thin and light polymeric naval rope, being only used to gradually pull heavier rope and chain compositions until only the mooring link remains between the two naval structures. The main dynamic forces issues to be experienced by the UAV are due to the line's length, which will increase over time, and the drag effects caused by the wind hitting on the messenger line.

The next two operation stages refers to the destination approach. In addition to flight control, it is necessary to detail the adopted convolutional neural network to perform vessel detection and why it was chosen, the network training, and its results. This step's flight control will have a state prediction and sensor fusion step with an Extended Kalman Filter. Therefore, the next Subsections III.2 and III.3 will also present control and filter modelling. The methodology uses computational vision to aid the navigation since the vehicle has a vast empty space around it and the destination objects are too extensive. Furthermore, the GPS and avionic sensors have some noise readings that could cause navigation errors and maybe a collision with the ship. Fusing the camera readings with the sensors using EKF is an approach to avoid that problem.

III.2 YOLOff Training and Validation

A novel approach to the training was used, dividing it into two stages. The first is responsible for freezing the first 26 of the 53 layers, only changing the last layers' weights. The training monitors the 'Yolo-loss function' (Redmon et al. 2016), so if the loss and validation loss reaches the minimum desirable value with this step, there's no need to train the weights of the frozen layers, finishing the train in this first step.

The second training only begins if the first one doesn't reach the desired precision. All layers will be unfrozen in this step. It will be applied a variable descent learning rate for making the training process more aggressive by modifying more weights if the loss and validation loss functions stabilize themselves on a baseline for three consecutive epochs. The goal is to reduce the loss function output between epochs even more, resulting in a more accurate detection. The purpose of these two steps is a possible reduction of time and optimize the training process.

For the training, a set of 560 real shuttle tanker or FSO/FPSO images were annotated manually using Computer Vision Annotation Tool (CVAT) (CVAT 2021). This caused the YOLOff to not be able to detect the vessels in simulation because the models used in simulation are simplified solids, and using only real ship images caused wrong classifications due to the fact that the images used to train were much more detailed (more texture characteristics).

For the second training, it was used 580 images where 20 of those ship images were generated by the 3D Gazebo models using on the simulated world as a data augmentation strategy, and with this, the results improved for the detection in simulation. On each image, the whole ship, its bow, mid-ship and stern were annotated as shown in Figure III.4. The training was performed using 70% of the images for training and 30% of the images as validation, the stop criteria in each epoch was the "Yolo-loss" function (Redmon et al. 2016).

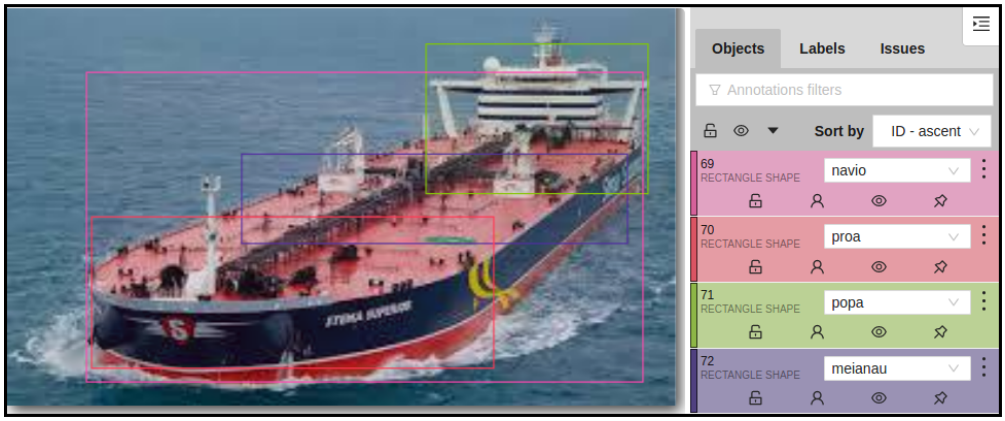


Figure III.4: Example of an annotated image in CVAT (Ramos et al. 2021).

With the YOLOff trained, the CNN was able to detect the ship and its 3 generic regions described before. The camera ROS node in which the CNN was running feeds the navigation ROS controller

with the desired region (configured by the operator at the beginning of stage 1) centroid coordinates, automatically detected by the YOLOff. The controller has a simple design: navigate forward, in direction of the interest region. If this region starts to move away from the image center, correct the UAV's orientation angle until the interest region is approximately in center of the image again. This methodology was chosen in order to provide precision to the ship's approximation by the drone.

The YOLOff network test was based on average precision methodology (mAP) and on $Precision \times Recall$ (or $P \times R$) curve (Padilla et. al. 2020). The mAP metric allows inferring how well a detected object is related to its respective ground truth. However, this methodology can lead to misinterpretations because the network may detect annotated objects and several non-existing objects within the image. The $P \times R$ curve eliminates this problem, where P is the reason between true positives and the total of detected objects in an image, and R denotes the reason between true positives and the total ground truths in an image. It is expected to P falls as R improves, but a good object detector has high P and R at the end of the process.

III.3 Extended Kalman Filter

In this research, the prediction estimates the state from the UAV's orientation (yaw), the x and y positions, and linear (v) and angular (ω) velocities. The update step corrects the state found in the prediction phase. Figure III.5 presents a simple Cartesian scheme representing the UAV's (x, y) position, its linear v and angular ω velocities, and the yaw.

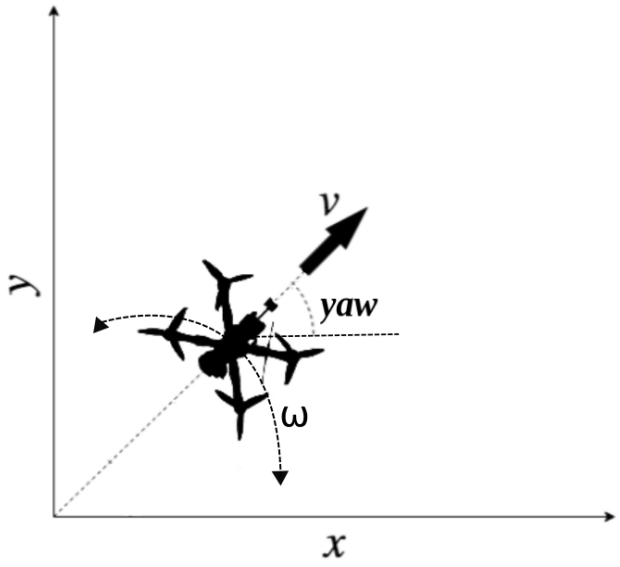


Figure III.5: Cartesian operation scheme (elaborated by the author).

The state equations of the modeled filter are:

$$\begin{cases} x_{k+1} = x_k + v_k \Delta t_k \cos(\text{yaw}_k) + w_{x_k} \\ y_{k+1} = y_k + v_k \Delta t_k \sin(\text{yaw}_k) + w_{y_k} \\ yaw_{k+1} = \text{yaw}_k + \omega_k \Delta t_k + w_{\text{yaw}_k} \\ \omega_{k+1} = \omega_k + \epsilon_{\omega,k} w_{\omega_k} \\ v_{k+1} = v_k + \epsilon_{v,k} w_{v_k} \end{cases} \tag{III.11}$$

where $\epsilon_{\omega,k}$ and $\epsilon_{v,k}$ are the noise gain therms in linear and angular velocities, and the w therms are assumed as the "extra errors" or noise, in-process or state equations, imposed by non-deterministic disturbances. The Δt_k represents the time step between two sensor readings. The linearized state equations can be represented in state-space matrix form as:

$$\mathbf{T}_{k+1} = \mathbf{F}(\mathbf{T}_k)\mathbf{T}_k + \mathbf{\Gamma}(\mathbf{w}_k)\mathbf{w}_k \tag{III.12}$$

where

$$\mathbf{T}_k = \begin{bmatrix} x_k & y_k & \text{yaw}_k & \omega_k & v_k \end{bmatrix}^T \tag{III.13}$$

is the state vector and

$$\mathbf{F}(\mathbf{T}_k) = \begin{bmatrix} 1 & 0 & -\Delta t_k v_k \sin(\text{yaw}_k) & 0 & \Delta t_k \cos(\text{yaw}_k) \\ 0 & 1 & \Delta t_k \cos(\text{yaw}_k) & 0 & \Delta t_k \sin(\text{yaw}_k) \\ 0 & 0 & 1 & \Delta t_k & 0 \\ 0 & 0 & 0 & 1 & 0 \\ 0 & 0 & 0 & 0 & 1 \end{bmatrix} \tag{III.14}$$

denotes the jacobian of $\mathbf{T}_k$. Matrix $\mathbf{\Gamma}(w_k)$ contains the partial derivatives of the state equations with respect to the stochastic terms in the w_k vector:

$$\mathbf{\Gamma}(w_k) = \begin{bmatrix} 1 & 1 & 1 & 1 & 0 \\ 1 & 1 & 1 & 1 & 0 \\ 1 & 1 & 0 & 0 & 1 \end{bmatrix}^T . \tag{III.15}$$

Note that w_k relates with noise covariance, but yaw_k is estimated with two sensor components, the flight controller compass, and the camera-estimated orientation. The sensor matrix $\mathbf{h}_k(\mathbf{T}_k)$ representing measured states is represented by:

$$\mathbf{h}_k(\mathbf{T}_k) = \begin{bmatrix} x_k & y_k & \text{yaw}_{k,\text{compass}} & \text{yaw}_{k,\text{YOLOFF}} & \text{yaw}_{k,\text{LK}} & \omega_k & v_k \end{bmatrix}^T , \tag{III.16}$$

where $\text{yaw}_{k,\text{compass}}$ is just the orientation from the flight control unit (FCU) compass, $\text{yaw}_{k,\text{LK}}$ is the orientation based on Lucas-Kanade optical flow algorithm and $\text{yaw}_{k,\text{YOLOFF}}$ is the orientation based on horizontal position variation of the detected object of interest in camera readings defined by:

$$\text{yaw}_{k,\text{YOLOff}} = \text{yaw}_{(k-1),\text{YOLOff}} + \gamma_p \frac{(\text{obj}_{x,k} - \text{obj}_{x,k-1})}{\text{img}_x} \Delta t_k \tag{III.17}$$

where the parameter img_x is the center of the camera's image, $\text{obj}_{x,k}$ is the x-coordinate corrected by a linear Kalman estimation process of the object centroid detected by YOLOff CNN in the current camera's image frame, and $\text{obj}_{x,k-1}$ is the same reading for the previous frame. The, γ_p $(0 < \gamma_p < 1)$ is a proportional gain defined by the reason between the calculated current distance from the UAV to the delivery point and the initial distance where the UAV begins its approach. When the UAV gets closer to the delivery region, the centroid variations tend to be bigger, so this coefficient becomes smaller to correct false yaw deviations estimated by the camera. The initial orientation angle is the compass measurement, but the subsequent angle estimations with YOLOff object detector are defined with this process.

The variable Δt_k is the time step between two successive detections. The higher Δt_k, the higher the current yaw estimation deviation compared to the previous yaw estimation from the camera. The initial camera yaw is set to be equal to the measured by the compass, and if the yaw estimation from YOLOff differs from the compass' measurement of more than 10^o, the $\text{yaw}_{(k-1),\text{YOLOff}}$ is reset to be the last compass measurement to avoid yaw estimations with a high error if the detection fails.

For the optical flow yaw angle estimation, as already stated before, the algorithm is based on classical Lucas-Kanade method. Summing up the process, the Lucas-Kanade is based on apparent movement of pixels belonging to an object on an image on two consecutive frames. Given the pixel $P(x, y, t)$ of an tracked object on a frame in time t, this pixel will move a distance (dx, dy) on next frame. Therefore, the observed pixel motion can be described by:

$$P(x, y, z) = P(x + dx, y + dy, t + dt). \tag{III.18}$$

Expanding the right term in Taylor series and dividing it by dt, we get:

$$\frac{\partial f}{\partial x}\frac{dx}{dt} + \frac{\partial f}{\partial y}\frac{dy}{dt} = 0 \tag{III.19}$$

where:

$$\begin{cases} \frac{\partial f}{\partial x} = f_x \\ \frac{\partial f}{\partial y} = f_y \\ \frac{dx}{dt} = u \\ \frac{dy}{dt} = v \end{cases} \tag{III.20}$$

For the studied pixel, all the other pixels in its neighborhood will probably have the same motion. In the Lucas-Kanade method, the observed pixel is the central element of the 3 $\times$ 3 mask. Thus, Equation III.19 will be solved for 9 points to estimate motion, which represents 2 variables being u and v (motion in x and y directions, respectively). Solving these equations, the final result is:

$$\begin{bmatrix} u \\ v \end{bmatrix} = \begin{bmatrix} \sum_i f_{x_i}^2 & \sum_i f_{x_i} f_{y_i} \\ \sum_i f_{x_i} f_{y_i} & \sum_i f_{y_i}^2 \end{bmatrix}^{-1} \begin{bmatrix} -\sum_i f_{x_i} f_{t_i} \\ -\sum_i f_{y_i} f_{t_i} \end{bmatrix} \tag{III.21}$$

Using this mathematical modeling, given a set of interest points, the algorithm returns the (u, v) motions of those points. The yaw estimator takes the average u motion of the interest points and estimate $\text{yaw}_{k,\text{LK}}$ as:

$$\text{yaw}_{k,\text{LK}} = \text{yaw}_{(k-1),\text{LK}} + u_{\text{avg}} \Delta t_k \tag{III.22}$$

This yaw orientation estimation with Lucas-Kanade optical flow presents a considerable error because the pixel motions in x-axis can be originated by the UAV's rotation, which is the movement desired, but also by the robot's drifting and movement in flight. The yaw estimation with the YOLOff and the sensor readings have errors as well, due to sensor noises and object detection imprecisions. The fusion of those readings with EKF has the function of reducing these errors and improve yaw estimation, to improve the controller.

Compared to (Driessen et al. 2018) EKF modelling, which presents a bias compensation strategy to the sensor having high measurement drifting, this work uses a momentary replacement of the sensor reading with the higher drifting to the one which has less drifting, continuing estimation from there. In other words, if the estimated $\text{yaw}_{k,\text{LK}}$ or $\text{yaw}_{k,\text{YOLOff}}$ present high deviations, the next estimation does not use it for the next estimation. Instead of this, $\theta_{k,\text{compass}}$ is adopted, which will always have less drifting, therefore "resetting" prediction with the camera.

The measurement, prediction, and process covariances can be chosen to adjust these arrays properly, but usually, those matrices are just set with initial high covariances, as stated before regarding "initial ignorance". The EKF filtering and prediction process will quickly reduce the high initial error within few steps, turning the fused measurement more reliable. Thereby, the EKF steps are executed as follows:

i State prediction:

$$\mathbf{T}_{k+1}^{(-)} = \mathbf{T}_k \tag{III.23}$$

ii Calculate prediction covariance matrix $\mathbf{P}$:

$$\mathbf{P}_{k+1}^{(-)} = \mathbf{F}(\mathbf{T}_k)\mathbf{P}_k\mathbf{F}(\mathbf{T}_k)^T + \mathbf{\Gamma}(\mathbf{w}_k)\mathbf{Q}_k\mathbf{\Gamma}(\mathbf{w}_k^T) \tag{III.24}$$

where $\mathbf{Q}_k$ is the process noise covariance matrix

iii Calculate filter gain $\mathbf{K}$:

$$\mathbf{K}_{k+1} = \frac{\mathbf{P}_{k+1}^{(-)}\mathbf{H}(\mathbf{T}_k)^T}{\mathbf{H}(\mathbf{T}_{k+1})^T + \mathbf{R}_{k+1}} \tag{III.25}$$

where $\mathbf{P}_{k+1}^{(-)}$ is obtained by equation (III.14), $\mathbf{H}(T_k)$ is the Jacobian of sensor matrix $\mathbf{H}(\mathbf{T}_k)$ and $\mathbf{R}_k$ is the covariance matrix of the sensor noise .

iv Update states:

$$\mathbf{T}_{k+1} = \mathbf{T}_{k+1}^{(-)} + \mathbf{K}_{k+1}[\mathbf{z}_{k+1} - \mathbf{h}_{k+1}(\mathbf{T}_{k+1}^{(-)})], \tag{III.26}$$

where $\mathbf{z}_k$ is the observation vector, obtained as a function of $\mathbf{h}(T_k)$ and the sensor error vector $\boldsymbol{\nu}$:

$$\mathbf{z}_k = \mathbf{h}(\mathbf{T_k}) + \boldsymbol{\nu} \tag{III.27}$$

v Finally, the prediction covariance matrix is updated:

$$\mathbf{P}_{k+1} = [\mathbf{I} - \mathbf{K}_{k+1}\mathbf{H}(\mathbf{T}_{k+1})]\mathbf{P}_{k+1}^{(-)} \tag{III.28}$$

By using the camera to maintain the right orientation and predicting the UAV's position with the EKF, the vehicle can begin to navigate towards the destination ship with safety. To correct the yaw deviation error and maintain the heading in direction of the destination, a generic Proportional-Derivative-Integrative (PID) controller is used to set the yaw increase or decrease command to the yaw controller of the UAV. Figure III.6 presents the closed loop control diagram.

The primary controller is the position, which is fed by the GNSS module. This controller will read the UAV's position from the GNSS and calculate the distance from the vehicle to the coordinate of delivery point location. It will only act if the UAV is dangerously close to the destination and still hasn't find the marker. It's noteworthy that the GNSS module also inputs the velocity readings to the EKF, since the simulated UAV doesn't have speed sensors. The secondary controller is the yaw, which is fed by the input signal generated by the difference between the yaw prediction with the EKF and the center of the object of interest detected on camera (the desired setpoint is always with the object of

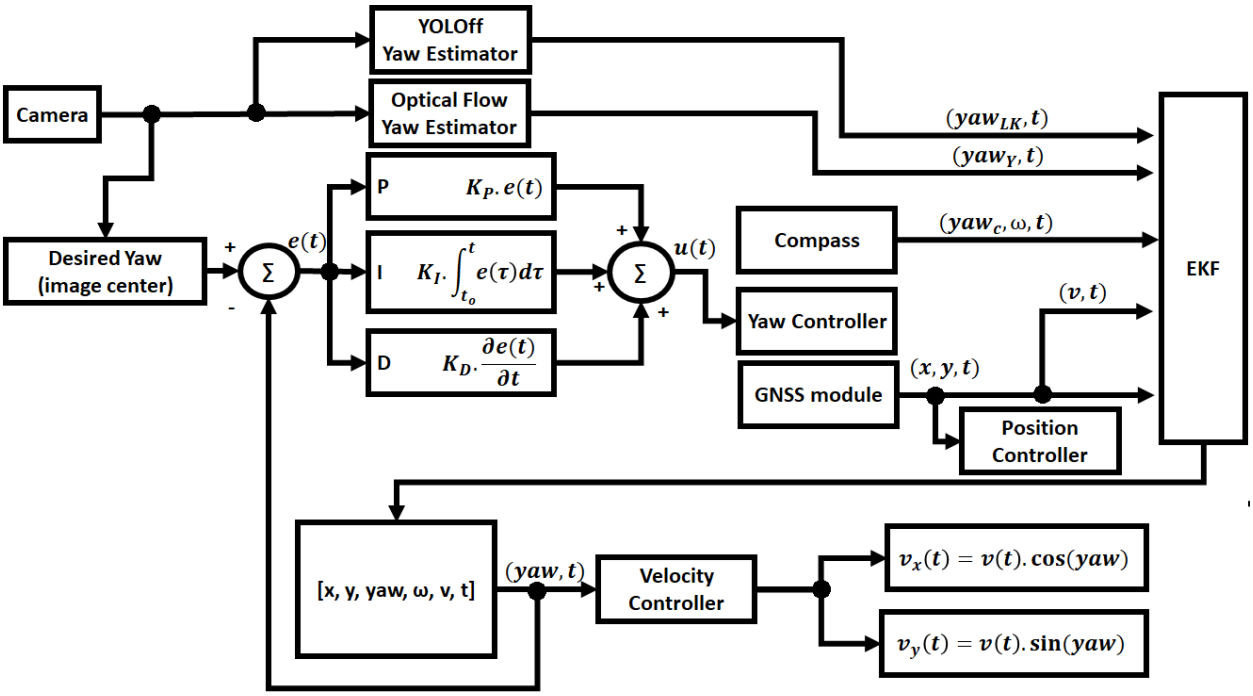


Figure III.6: Control loop of approaching flight mode strategy adopted in stage 2 (consider yaw_y as the yaw$_{k,\text{YOLOff}}$, yaw_LK as the yaw$_{k,\text{LK}}$, and yaw_c as the $yaw_{k,compass}$ of the model description)(elaborated by the author).

interest approximately on image's center). It will correct the UAV's orientation to maintain it navigating toward the desired point. The tertiary controller is the velocity, which will be fed by the yaw and velocity predictions from the EKF and output velocity commands to the UAV, completing the inertial navigation.

For the predicted yaw precision evaluation, a KY-040 rotary encoder module was attached at the UAV's bottom, with its rotation axis coinciding with the vehicle rotation axis, as seen in Figure III.7. The encoder mechanism, and therefore the UAV, were fixed on the table, so the only motion possible was rotating clockwise or anticlockwise.

The yaw angle could be estimated rotating the drone and therefore the encoder, whose output was captured by an Arduino Mega 2560 board (Arduino 2021), processed and transferred to the validation script using the Python serial communication packages. To improve and guarantee clean encoder signals to Arduino, the module outputs were filtered by a Schmitt-Trigger circuit (Kumar 2019), presented in Figure III.8.

A ship scaled model was placed in front of the robot in order that the YOLOff could use the camera's images to recognize the ship and estimate yaw by the object detection and Lucas-Kanade optical flow. The test was performed by manually rotating the UAV and comparing the yaw angles of the sensors, camera, and EKF predictions with the angle readings provided by the encoders, which were considered the ground-truth given their high precision.

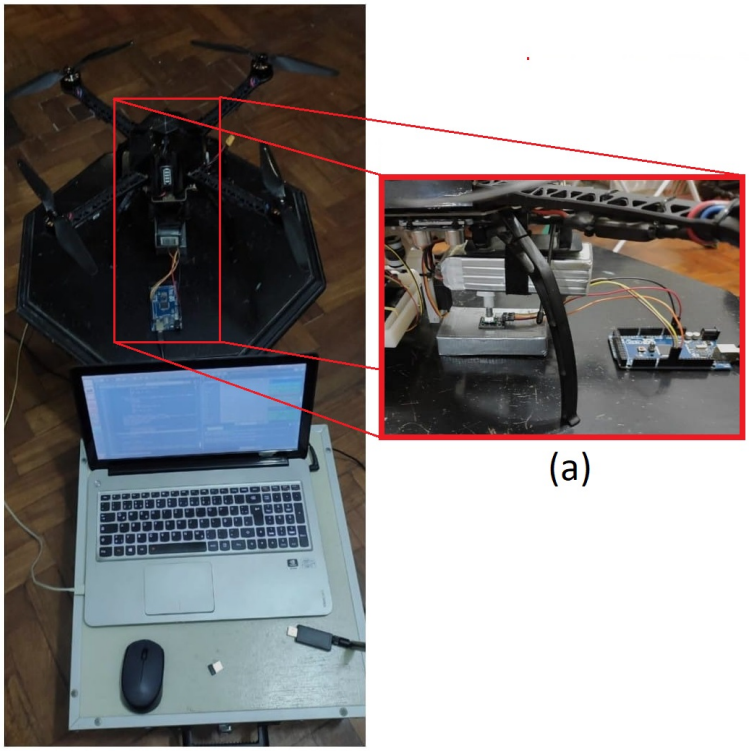


Figure III.7: EKF validation setup with the rotary encoder detail in (a) (elaborated by the author).

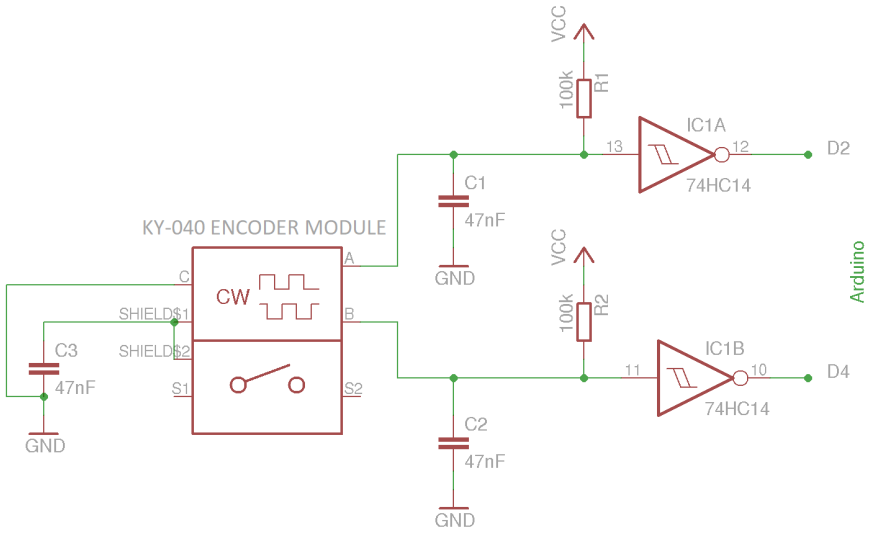


Figure III.8: Schmitt-Trigger debouncing circuit (elaborated by the author).

III.4 Cable delivery location

This final stage of the proposed methodology occurs when the robot reaches the maximum approach distance or recognizes the messenger cable's marker. The sign can be a fiducial marker, a system comprised of a set of valid markers and an CV algorithm that is responsible for performing the detection (Garrido-Jurado et al. 2014), or a simples QR Code, which is implemented in this work. This marker is a symbol strategically positioned at a vessel's area where the robot must make the final approach and release the cable.

Another possible approach is for an operator to carry out the signal and show the UAV where to land. Both fiducial markers or QR Code allows the controller to estimate camera's positioning data (and therefore the UAV position data) based on the position of the found sign, and also calculate the distance to the target more reliably than using the ship's region detected by the YOLOff camera node. However, on the current work the UAV simply stops the mission when it detects the marker in simulation. Still, it will use the marker for satisfactory approximation and release the messenger line in future works.

The marker detection was performed using `pyzbar` barcode and QR code detection on digital images python library. As a numerical precision metric, authors used the Intersection Over Union (IOU) (Blanger e Hirata 2019; Rezatofighi et al. 2019) parameter for evaluating the marker detection algorithm accuracy. The IOU measures how well a detected object in an image is related to the respective real object (or ground-truth). Mathematically, the metric is the relation between the intersection on the detected and ground-truth bounding boxes areas and the union of those same areas, as shown in Figure III.9.

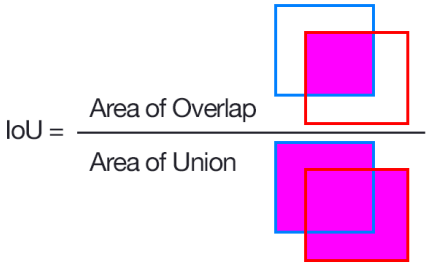


Figure III.9: IOU metric definition (adapted from (Balsys 2019)).

When the `camera-kf` node detects the marker on simulation, the IOU for each image frame is calculated and saved on a vector. The results are evaluated for their average, standard deviation, and variance in the results section.

III.5 Flight controller with MavROS

The controller was developed in Python language using ROS packages (Quigley et al. 2009), specially MavROS, which is a package used to develop aerial robotics application using Mavlink telemetry protocol (Atoev et al. 2017). The developed controller was designed for a PixHawk Px4 FCU (Ardupilot 2020), receiving the board's sensor readings and camera as well, processing it on the base station using MavROS, and sending flight commands back to the FCU. The ROS system works with a graph structure in which the processing is realized on nodes, and those nodes can send and receive messages from other nodes, where the messages represent an individual or multiplexed sensor readings, control inputs, state, planning, etc. All the robotic system's actuators, sensors, and controllers are

abstracted on those nodes and messages.

The developed robotic system in ROS is presented in Figure III.10. The `/mavros` node is the main ROS package for the MavLink communication protocol. This node is responsible for receiving all sensors telemetry readings from the FCU and also for sending flight commands to the onboard controller. The `/gps-reading` node represents the initial configuration and calculation of the first stage of the operation. The messages `/mavros/global-position/global` represents the GPS global position readings of the UAV, which is used by this node to calculate the initial trajectory (sent to the controller node trough `/configure-trajectory` message) and to send the approximate location of the delivery point (configured by the operator), sent on `/configure-center` message.

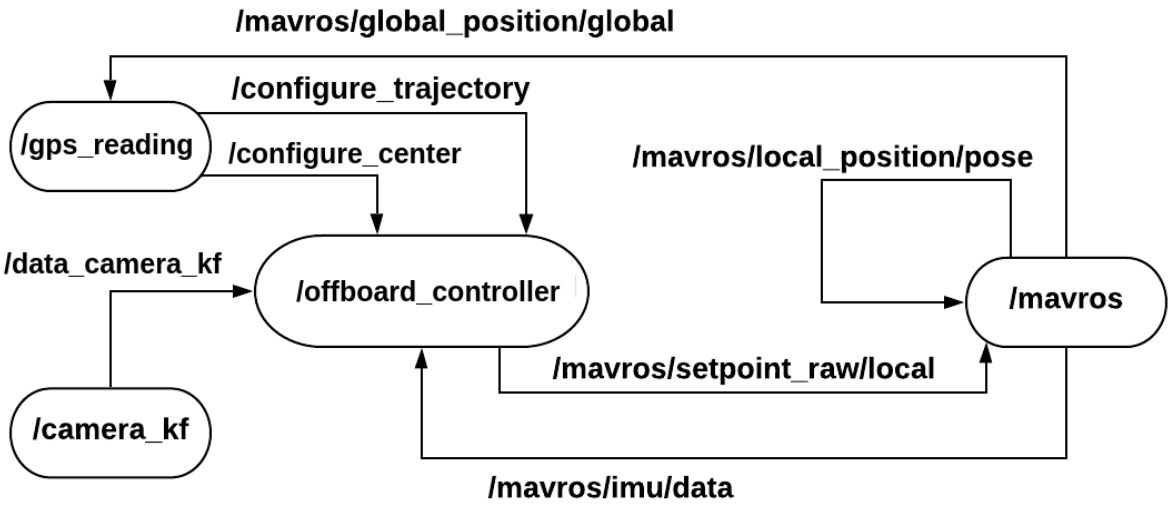


Figure III.10: Robotic system active nodes and messages (elaborated by the author).

All the control strategy, mission states, and EKF are executed on `/offboard-controller` node. The camera's images, the YOLOff detector, and the Lucas-Kanade optical flow algorithms are implemented on `/camera-kf` node, so does the yaw estimation with the computer vision strategies mentioned before, sent to the controller through the `/data-camera-kf` message. The `/mavros/imu/data` messages contain several position readings of the UAV's body, including yaw readings provided by the FCU compass. Those readings are EKF-fused with the yaw estimations from the camera, producing more precise output and predicting with high precision the next reading, which is processed to get velocity controls on UAV's (x, y) axis, sent to MavROS through `/mavros/setpoint-raw/local`. The MavROS send those flight commands to the FCU through MavLink protocols, which execute the commands.

III.6 Technical and Economic Feasibility Study

(This subsections are based on (Ramos et al. 2021))

As stated, the main goal of this technology is to reduce both man-hour and resources applied to the

offloading operations by using a UAV to transport the messenger line in autonomous mode. The goal is to have an operator on deploy point to perform initial configurations and observe UAV's flight (it needs to be ready to regain manual control if something goes wrong) and another operator on destination point to receive the messenger line, reducing a whole team of people working in this process and eliminating dangerous tools and actions (such as "fishing" the line on sea surface). The proposed methodology also has high potential to considerably reduce risks for performing offloading, as the shuttle tanker and support vessels can operate farther from the oil rig during mooring and connection once the UAV will autonomously carry the messenger line to its destiny, and reduce environment limitations as well by not using the LHs described in the first chapter of this work, which has waves, surface current, wind, and visibility limitations, while the UAV will have only wind as a challenge to face.

For the project economic evaluation, will be supposed the application of the methodology on an FPSO in its final production year, when the production presents decline and the last offloading operations are easily counted, and also for an FPSO on its initial production years, where the production is stable and high.

III.6.1 Project in Final Operational Year

Based on the oil and gas production dynamic panel elaborated by the Brazilian National Petroleum Agency (ANP 2021), the oil production from January 1^{st} 2021 to January 31^{th} 2022 will be estimated based on Belyadi et. al. (2019), analyzing the historical production curve of the generic FPSO as a decline production curve in its final production years operating on the selected oil field for this study. The typical production decline in the oil and gas industry is represented in Figure III.11.

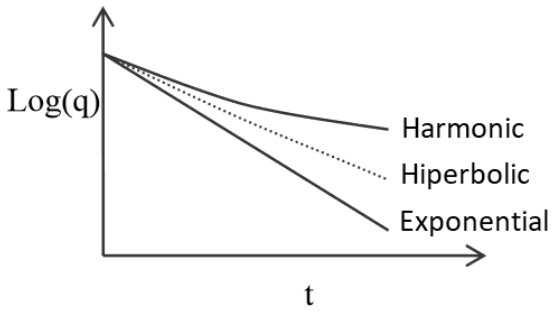


Figure III.11: Production Decline Curves (elaborated by the author).

Thus, based on the chosen FPSO production since the end of ramp-up, we can assume that the harmonic model will represent a good approximation to estimate future oil production flow, as seen in Figure III.12. The production harmonic decline rate a can be expressed by Equation III.29.

$$a = -\frac{1}{q}\frac{\partial q}{\partial t} = a_0(\frac{q}{q_0}) \tag{III.29}$$

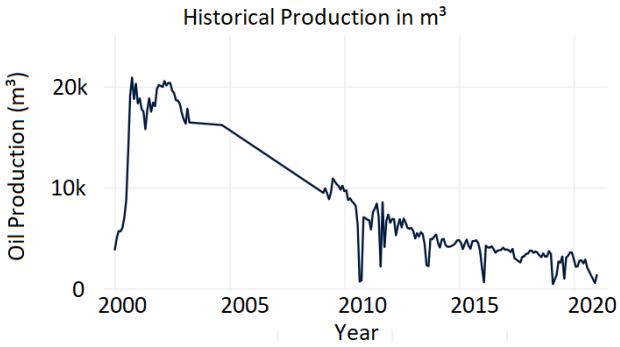


Figure III.12: FPSO's Historical Production (ANP 2021).

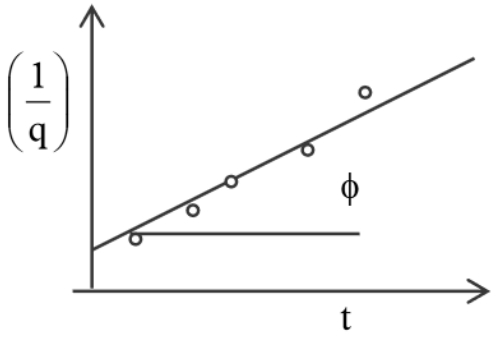


Figure III.13: Production Analysis for the Harmonic Decline (elaborated by the author).

where a_0 is the initial decline rate, q is the production flow in m^3/d, q_0 is the initial production flow in m^3/d and t is the time in days. Rearranging Equation III.29, we obtain the following.

$$\frac{q_0}{q^2}\partial q = -a_0 \partial t \tag{III.30}$$

$$\int \frac{q_0}{q^2}\partial q = \int -a_0 \partial t \tag{III.31}$$

Therefore:

$$\frac{q_0}{q} = 1 + a_0 \cdot t \tag{III.32}$$

$$\frac{1}{q} = \frac{1}{q_0} + \frac{a_0}{q_0} \cdot t \tag{III.33}$$

Now, it is possible to determine the line's angular coefficient $\frac{a_0}{q_0}$ and the linear coefficient $\frac{1}{q_0}$ by graphically analyzing the production overtime data in the dynamic panel (ANP 2021), as shown in Figure III.13.

Thus:

$$\tan \phi = \frac{a_0}{q_0} \tag{III.34}$$

Once the production for the final year is estimated, the offloading operations and their dates need to be also estimated. The offloading must occur before the FPSO is full otherwise this would cause production to stop. The FPSO and FSO also have a certain amount of residual oil in their cargo tanks that serve as ballast, and it may vary depending on platform project, structural and stability necessities, maintenance, meteorological and oceanographic conditions, etc (OCIMF 2018). Being S_n the total inventory of oil in cargo tanks at the end of the day n, B_n the ballast of fluid in cargo tanks, C_n the operational storage capacity, P_n the oil production accounted from 00 h to 23 h 59 min of the day n, T_n the volume of oil transferred from the FPSO/FSO tanks to shuttle tanker during day n, the volume V_n available for offloading at the end of the day n is given by:

$$V_n = (S_{n-1} + P_n) - B_n - T_n \tag{III.35}$$

But $S_n = S_{n-1} + P_n$; $S_n \leq C_n$. Then:

$$V_n = S_n - B_n - T_n \tag{III.36}$$

Thus, starting with an S_0 oil volume, the total inventory of oil will be added a P_n (calculated based on Equation III.33) every n day from January 1^{st} 2021 until the FPSO ends its production, on December 31^{th} 2021. Whenever the volume available for offloading V_n is equal or greater than an V_{off} volume, there will be an offloading on that day of volume T_{off} (knowing $T_{\text{off}} = V_{\text{off}}$), otherwise the transferred volume on the day n will be zero. Also will be considered that the total oil ballast B_n of the FPSO at the last day of production will be transferred after the production stops, so there will be some offloading operations until the total volume of oil is zero (in practice, the oil in ballast is replaced by seawater), ending the life cycle at January 31^{th} 2022.

The information of S_0 will be used as an internal oil inventory in the real FPSO based on the panel (ANP 2021), for more realistic analysis. Also, the V_{off} and T_{off} parameters will be considered as the average offloaded oil volume on the FPSO history. The operational storage capacity C_n and the volume of oil ballast in cargo tanks B_n will be considered as the average volumes on the FPSO history as well. Therefore, given the oil inventory evolution, the offloading will be placed during the year of production simulated, so becoming known an estimate of the number of offloading operations still needed.

After that, there is a necessity to estimate the costs of each operation and the costs of each operation applying the new methodology based on robotics systems, then, it will be measured the economic gain

between them. The estimated offloading operation costs M_{TOTAL} will be defined as:

$$M_{\text{TOTAL}} = M_{\text{LH}} + M_{\text{AHTS}} + M_{\text{CAP}} + M_{\text{ST}} \tag{III.37}$$

where M_{LH} is the total LH cost, based on DSB Offshore shipbroking agency average costs of LHs for offloadings (DSB 2020), given in $US\$/Operation.$ The M_{AHTS} is given by Clarksons shipbroking agency (Clarksons 2020), as well as Sea Boats Marine Brokers are the reference for M_{CAP} costs (Brokers 2020), and Barry Rogliano Salles is the reference for Shuttle Tanker M_{ST} costs (BRS 2020). It is noteworthy that the AHTS, shuttle tanker and maneuver captain costs depends on offloading total time, once the scenario supposes that the contracts are paid by $US\$/day$ tariff for each resource. The total offloading time t_{off} will be given by:

$$t_{\text{off}} = t_{i_{\text{off}}} + \frac{T_{\text{off}}}{Q_{\text{off}}} + t_{f_{\text{off}}} \tag{III.38}$$

Where $t_{i_{\text{off}}}$ is the average time in hours taken on initial works (approximation, mooring, and connection), T_{off} is the total volume of oil to be transferred, Q_{off} is the average pumping flow of the FPSO in m^3/h, therefore $\frac{T_{\text{off}}}{Q_{\text{off}}}$ is the total time in hours taken to pump the offloading volume, and finally $t_{f_{\text{off}}}$ is the average time taken on final works (disconnection, untie and departure). The average time taken on initial and final works is based on FPSO's historical offloading datasheet information, as well as the average pumping flow.

In this way, the AHTS, maneuver captain and shuttle tanker costs on each operation will be given by the Equations III.39, III.40 and III.41. Notice that the R_{AHTS}, R_{CAP} and R_{ST} are the average AHTS, maneuver captain and shuttle tanker respective tariffs, practiced by Brazilian oil and gas companies contracts, converted in $USD/h.$ Also, for each offloading, the cost on the simulated scenario will be added by the projected dollar inflation accordingly to Brazilian Central Bank (BCB 2021).

$$M_{\text{AHTS}} = t_{\text{off}} \cdot R_{\text{AHTS}} \tag{III.39}$$

$$M_{\text{CAP}} = t_{\text{off}} \cdot R_{\text{CAP}} \tag{III.40}$$

$$M_{\text{ST}} = t_{\text{off}} \cdot R_{\text{ST}} \tag{III.41}$$

Similarly to Equation III.37, the total offloading operation cost of the proposed methodology $M^{\text{UAV}}_{\text{TOTAL}}$ will be given by:

$$M^{\text{UAV}}_{\text{TOTAL}} = M_{\text{UAV}} + M_{\text{AHTS}} + M_{\text{CAP}} + M_{\text{ST}} \tag{III.42}$$

The M_{AHTS}, M_{CAP} and M_{ST} are the same from a normal operation, but we are proposing changing the LH costs (M_{LH}) to UAV costs (M_{UAV}), since the main gain of this would be to replace the expensive LH boat resource to the UAV service to carry and delivery messenger line, then the ship would use its crane to pull either the mooring link or the offloading hose. Using this new methodology also would avoid LH approximation from both shuttle tanker and FPSO/FSO hulls, a risky maneuver that could cause accidents and collisions.

Another gain is that the LH operation is limited by wind speed and direction, marine surface current and direction, wave height, and visibility (i.e., it requires daylight to operate), and the UAV is only limited by wind speed. When one or more of those meteorological and oceanographic conditions are critical, the LH can't operate. Therefore, the offloading costs will considerably rise as all resources will be waiting until the environmental conditions are permissive. The proposed methodology has the potential to increase the probability of an operation occur, and also that it occurs within a programmed time window as well, which would increase efficiency, and therefore, reduce costs.

Besides, the M_{UAV} costs are considerably lower than M_{LH} costs themselves. The first one just considers the initial investment of buying the UAV (CAPEX), crew training, maintenance, which is increasingly lower (69), and the operation, which is simpler than the LH operation once it just needs an operator to configure and observe the UAV, and another to receive the messenger line. The M_{LH} considers the LH affreightment contract costs itself, the used fuel, the navigation time to the FPSO/FSO, the waiting time during operation, the line handling operation services fees, and the man-hour of the crew, which can be up to 12 seamen. All costs will be detailed on discussions topics ahead, but to sum up, the M_{UAV} costs in $USD/Operation$ within a certain month on the simulated time scenario will be given by:

$$M_{\text{UAV}} = M_{\text{CAPEX}} + M_{\text{OPEX}} \tag{III.43}$$

Where:

$$M_{\text{OPEX}} = M_{\text{operation}} + M_{\text{training}} + M_{\text{maintenance}} \tag{III.44}$$

The M_{CAPEX} will be the investment cost of buying a UAV that meets the operational needs plus Brazilian taxes over importing manufactured products and currency exchange, to know II, IPI, PIS, Cofins, IOF, ICMS, and ISS (whose rates will be detailed in discussion topics). It is important to notice that the aerodynamic effects of the messenger line on the UAV's flight behavior are not yet being accounted for, but the line weight, the minimal T_0 traction to be applied online to it don't touch water surface as a safety measure (see Figure III.3 scheme) and an exaggeration of wind drag forces are taken in account to choose an ideal UAV model that could operate without major problems, which

will be detailed ahead in this section. In the future, a more or less robust UAV may be chosen based on aerodynamic simulation results. Finally, the net present value (NPV) of each operation within the simulation time will be evaluated as:

$$NPV = \frac{M_{\text{TOTAL}_0}}{(1+i)^0} + \frac{M_{\text{TOTAL}_1}}{(1+i)^1} + ... + \frac{M_{\text{TOTAL}_k}}{(1+i)^k} = \sum_{m=0}^{k} \frac{M_{\text{TOTAL}_m}}{(1+i)^m} \tag{III.45}$$

And,

$$NPV_{\text{UAV}} = \frac{M^{\text{UAV}}_{\text{TOTAL}_0}}{(1+i)^0} + \frac{M^{\text{UAV}}_{\text{TOTAL}_1}}{(1+i)^1} + ... + \frac{M^{\text{UAV}}_{\text{TOTAL}_k}}{(1+i)^k} = \sum_{m=0}^{k} \frac{M^{\text{UAV}}_{\text{TOTAL}_m}}{(1+i)^m} \tag{III.46}$$

Where the parameter m is the month within the proposed simulation time period, M_{TOTAL_m} and $M^{\text{UAV}}_{\text{TOTAL}_m}$ are the respective total operating costs of the operation and the operation with the proposed methodology in a month m (the more operations, the higher the costs in a month) and i is the minimum interest rate. The economic gain G (or cost reduction) on each month, the total gain TG and the internal rate of return IRR, which is the minimum interest rate i that will make the NPV becomes zero, will be given as follow:

$$G_m = M^{\text{UAV}}_{\text{TOTAL}_m} - M_{\text{TOTAL}_m} \tag{III.47}$$

$$TG = NPV_{\text{UAV}} - NPV \tag{III.48}$$

$$\sum_{m=0}^{k} \frac{G_m}{(1+IRR)^m} = 0 \tag{III.49}$$

The simulated costs in numbers within each month of the economic simulation period as well the economic indicators described above will be presented and discussed in the next topic. It is important to notice that this FPSO only performs offloading with conventional ships. Thus, the economic simulated scenario will only consider this kind of operation. Even though conventional offloading are falling out of favor worldwide, some old FPSOs still perform this kind of operation. However, this fact won't invalidate the economic analysis of this work because the proposed methodology can reduce man-hour, time, and risks (Sphaier et al. 2012) in DP operations.

III.6.2 Project in the First Years of Production

This scenario considers the application of the methodology on a new FPSO project of a deepwater oilfield on Brazilian pre-salt. It will be considered a period of five years, from January 1$^{\text{st}}$ 2021 to January 1$^{\text{st}}$ 2026, which is a reasonable service lifetime for an industrial-class UAV. The simulated

FPSO is based on a production facility data extracted from the same oil and gas production dynamic panel (ANP 2021) to estimate the fluid production on this period and therefore the evolution of the inventory on the FPSO's cargo tanks.

Since the chosen FPSO began its production in March 2019, it is experiencing a production ramp-up that will become stable for the next years. Thus, the production is considered to be almost linear. Therefore estimating the oil inventory evolution, it is possible to project offloading operations through the period. This way, the volumes of each operation, time taken in the offloading tasks and resources cost rates will be the same as the first described scenario, except for the fact that the offloading operations considered now are always performed in DP mode, then it never uses LH and maneuver captain resources.

The quantities $M_{\text{UAV}_{\text{AHTS}}}$ and $M_{\text{UAV}_{\text{ST}}}$ are almost the same from a normal operation, but considering a time reduction on 5% of each operation time, applied both for the ST and the AHTS tariffs. The M_{UAV} costs represent the UAV operations, considering crew, planning, and execution of the flight. Using the proposed methodology also would avoid the necessity of line handling motorboats in special operations where the dynamic positioning system is not available. This gain, however, was not modeled on this analysis.

Other gains are based on the delay or postponement of offloading operations due to environmental conditions. The ST and AHTS are limited by wind speed and direction, marine surface current and direction, wave height, and visibility (i.e., it requires daylight to operate), and the UAV is only limited by wind speed. When one or more of those meteorological and oceanographic conditions are critical, the operation cannot go on. Therefore, the offloading costs will considerably rise as all resources will be waiting until the environmental conditions are permissive. The proposed methodology has the potential to increase the operation occurrence probability, and also that it occurs within a programmed time window as well, which would increase efficiency, and therefore, reduce costs. These gains were considered as a 5% cost reduction of the AHTS and ST total costs.

The M_{UAV} costs also consider the initial investment of buying the UAV, known as CAPEX, and only accounted on the first day of simulation. Also, at the end of each year, a 20% depreciation cost is accounted for over the initial investment, reducing every year. The operation crew training, UAV's maintenance, which is increasingly low (69), and the UAV's operation costs are grouped on OPEX costs. The operations are quicker than normal, once it just needs an operator to configure and observe the UAV, and another to receive the messenger line. The $M_{\text{UAV}_{\text{AHTS}}}$ considers the AHTS affreightment contract costs itself, the used fuel, the navigation time to the FPSO/FSO, the waiting time during operation, the line handling operation services fees, and the man-hour of the crew. The M_{UAV} costs in USD/Operation within a certain month on the simulated time scenario will be given by Equations III.43 and III.44.

The investment cost is considered for the same UAV of the first scenario, but assuming to endure for the lifespan of five years. In this case, operational costs of maintenance and crew training will also be higher than the considered for the only one year project. The NPV and total gain indicators will be the same of the previous scenario, but with different input values.

Chapter IV Results and Discussion

IV.1 Object Detection Training and Results

The training was not completed within the first step with frozen layers, taking 2.633 days (227515 seconds) in total. At first, the initial loss was 1288.57, and the validation loss was 252.10. The final loss and validation loss were 24.45 and 27.22, respectively. The YOLOff training results and some detection examples in real and simulated images are presented in Figures IV.1 and IV.2, respectively.

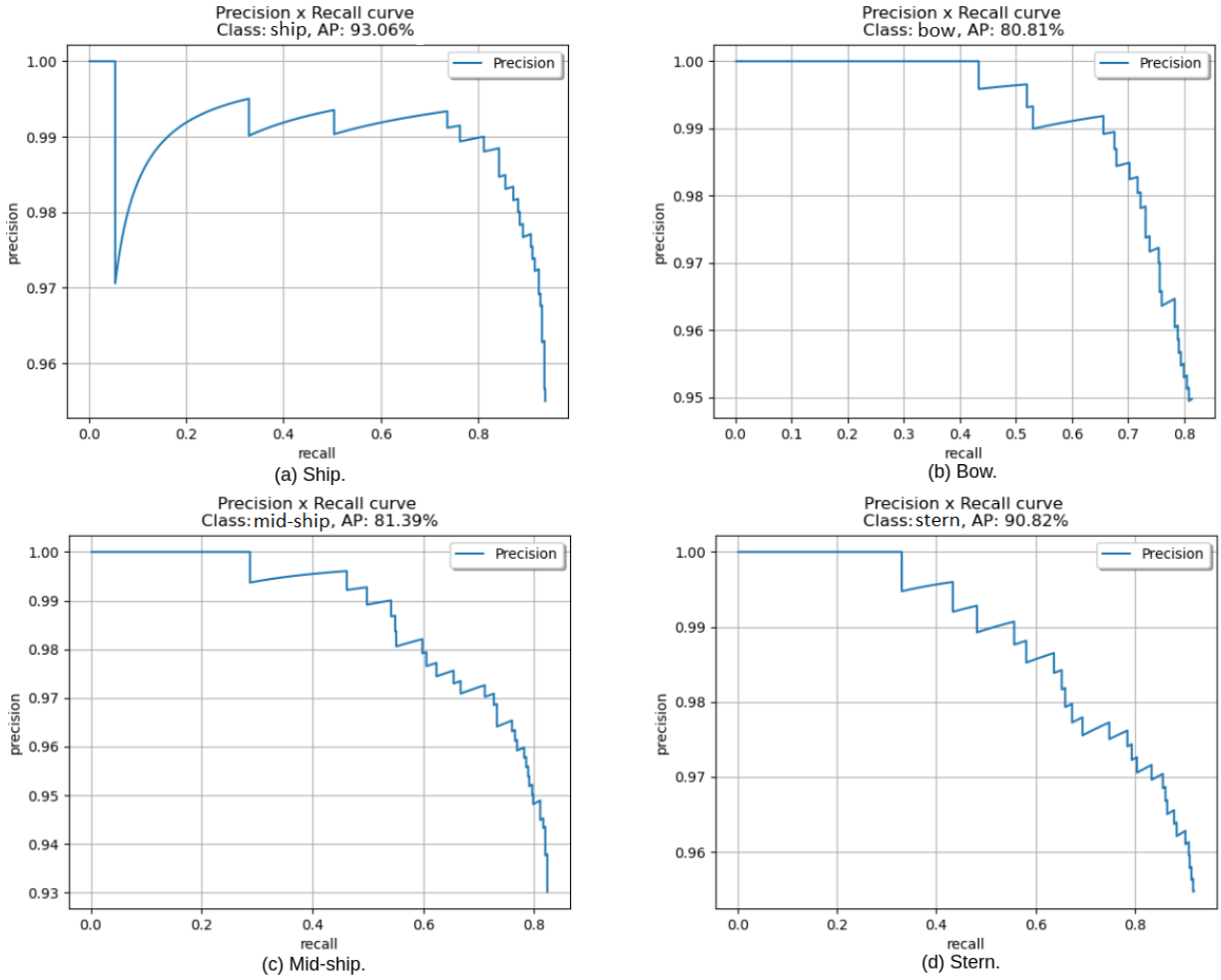


Figure IV.1: YOLOff results for all classes (Ramos et al. 2021).

Table IV.1 presents more detailed results for true positives (TP), false positives (FP), true negatives (TN), and false negatives (FN) when YOLOff was applied on the 580 training images. TPs' results compared to the total number of annotated ground truths, represented in this table as GTs, demonstrate

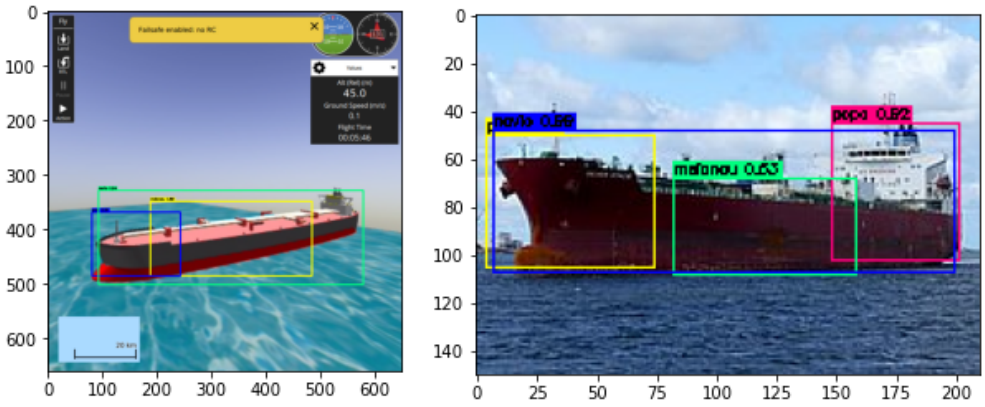


Figure IV.2: YOLOff example of detection (Ramos et al. 2021).

Table IV.1: Detection results.

-	**ship**	**bow**	**midship**	**stern**
Total GTs	611	558	550	575
TP	573	454	453	528
FP	27	24	34	25
TN	27	51	61	46
FN	38	104	97	47

that YOLOff is a good object detector for the designed application.

For a comparative result, the table IV.2 present the accuracy metric (ACC), and also the true positive, false positive, true negative, and false negative ratios (TPR, FPR, TNR, and FNR, respectively). This table shows that the YOLOff has good accuracy, mainly detecting the ship, and the error ratios (FPR and FNR) are considerably smaller than correct detection ratios.

In the simulation, it is running on the `/camera-kf` node. The ship mAP was 93.06%, and the bow, mid-ship, and stern were 80.81%, 81.39%, and 90.82%, respectively. The PxR curves also have appropriate behavior, with $Precision$ metric above 90% and $Recall$ metric above 80% after all detections in the 580 image dataset. It feeds its centroid as a data message to the offboard controller node when detecting the destination region in the image.

Table IV.2: Detection evaluation metrics.

Metric	**ship**	**bow**	**midship**	**stern**
$ACC = \frac{TP+TN}{TP+TN+FP+FN}$	90.23%	79.78%	79.69%	88.85%
$TPR = \frac{TP}{TP+FN}$	93.78%	81.36%	82.36%	91.83%
$FPR = \frac{FP}{FP+TN}$	50,00%	32,00%	35,79%	35,21%
$TNR = \frac{TN}{FP+TN}$	50,00%	68,00%	64,21%	64,79%
$FNR = \frac{FN}{TP+FN}$	6,22%	18,64%	17,64%	8,17%

IV.2 Sensor Fusion

Table IV.3 shows the Mean Absolute Error (MAE) and Mean Squared Error (MSE) for sensor readings and fused predictions compared to the encoder readings.

Table IV.3: EKF validation results.

Reading	MAE (^{o})	MSE (^{o2})
Compass	0.24	33.79
YOLOff	0.22	216.34
Optical Flow	0.47	86.61
EKF (Compas + YOLOff)	0.04	39.42
EKF (Compass + YOLOff + Optical Flow)	0.23	19.75

This result indicates that the proposed three-sensor fusion with an EKF predicting algorithm is the best estimator. Still, the compass alone would have a better reading than fusing the only compass with the YOLOff yaw estimation. The MAE shows that all readings are very close to the considered ground truth. The test results are presented in Figure IV.3. In practical terms, the yaw estimation through the camera is working well, and the EKF sensor fusion provides accuracy and robustness if some sensor reading fails.

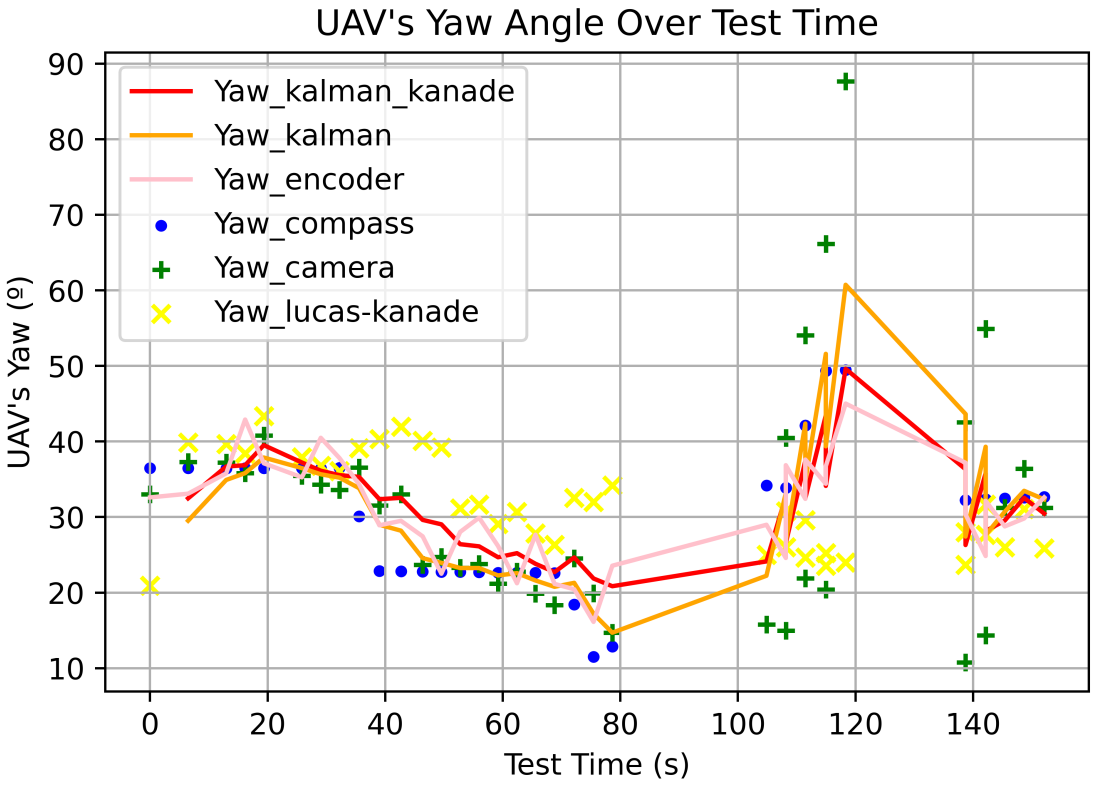


Figure IV.3: EKF validation essay results (elaborated by the author).

In practical terms, the yaw estimation through the camera is working well and the EKF sensor fusion provides accuracy and robustness if some sensor reading fails.

IV.3 Simulation Results

To test the developed controller, a simulation was performed in Gazebo environment (Gazebo 2021), which is an open-source platform for 3D robotics simulations. It provides realistic rendering of environments including high-quality lighting, shadows, textures, environment conditions (e.g., wind, waves, fog, gravity, Earth position, etc.), and all the robot's sensors. The simulated robot is a Typhoon H480 hexacopter, presented in Figure IV.4. It was used ROS Kinetic for developing the controller, the trajectory calculation, and camera nodes packages in the Python programming language. The MavLink was simulated through the MavROS package. The simulation and YOLOff training were executed in Linux 16.04 OS, with an Intel Core i7-3537U 2.00GHz processor, NVIDIA GeForce 625M graphics board, and 6GB DDR3 1600MHz RAM.

Note that based on real-life scale simplified 3D models of an FPSO and a shuttle tanker, the offloading world was built in Gazebo with both vessels positioned in tandem as in a real offloading operation, and also using physical engines for collision, gravity, flight, and aerodynamics, as seen in Figure IV.5.



Figure IV.4: Simulated hexarotor on Gazebo (elaborated by the author).

The initial UAV's position on the simulated world was set as $(-42.963770°S, -26.236411°W)$, a spot located approximately on Brazilian offshore pre-salt reservoirs location. The destination point (i.e., the approximate location of the final delivery spot) has coordinates around $(-42.9638135^oS, -26.2391134^oW)$, obtained in Gazebo's simulated GPS, therefore with high imprecision (as a real-life GPS). The initial distance between the UAV and the shuttle tanker at the end of the first stage of the mission (the blue d in Figure III.5) was configured as $d = 50$ m, and the limit distance between the UAV and the final spot was configured as 2 m.

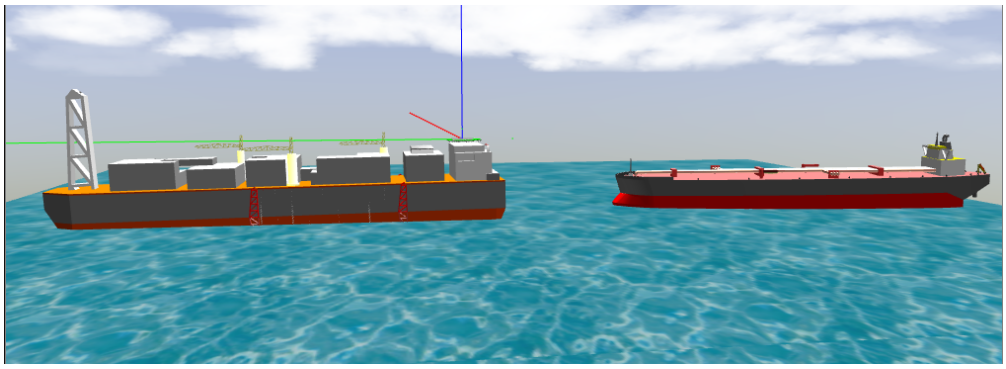


Figure IV.5: Simulated offloading world on Gazebo (elaborated by the author).

The marker detection was implemented using `pyzbar` barcode and QR code detection on digital images Python library. As a numerical precision metric, authors used the IOU (Blanger e Hirata 2019; Rezatofighi et al. 2019) parameter for evaluating the marker detection algorithm accuracy. The IOU measures how well a detected object in an image is related to the respective real object (or ground-truth).

As described in Section III, the path configured in simulation have a takeoff location point read by simulation GPS near $(-42.963770^{o}S, -26.236411^{o}W)$. The destination point have coordinates around $(-42.9638135^{o}S, -26.2391134^{o}W)$, obtained in Gazebo. The configured distance between UAV and ship at the end of trajectory was d = 50 m, the trajectory was calculated by equations II.1 to III.5, providing as result D = 301.716 m and θ = -90.1011^{o}. Figure IV.6 presents the calculated and performed trajectory projected in XY plane.

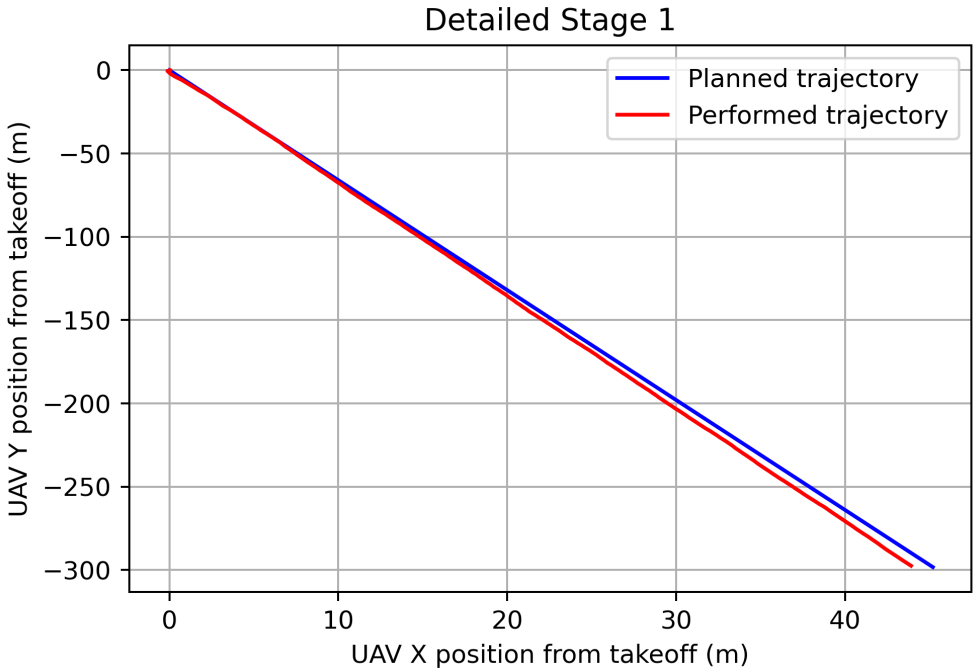


Figure IV.6: Calculated and performed trajectories (Ramos et al. 2021).

The designed controller allows a difference up to 2 m in reading location compared to the desired

location point in trajectory beyond GPS and conversion noises. Still, it presented itself as a very stable trajectory-guided navigation system and has some advantages from Mavlink (or MavROS in the simulation) and PX4 firmware, such as automatic takeoff and landing and the "*return to home*" failsafe. The flight height related to the takeoff point was configured as 5 m. Figure IV.7 shows the measure altitude results during operation step 1.

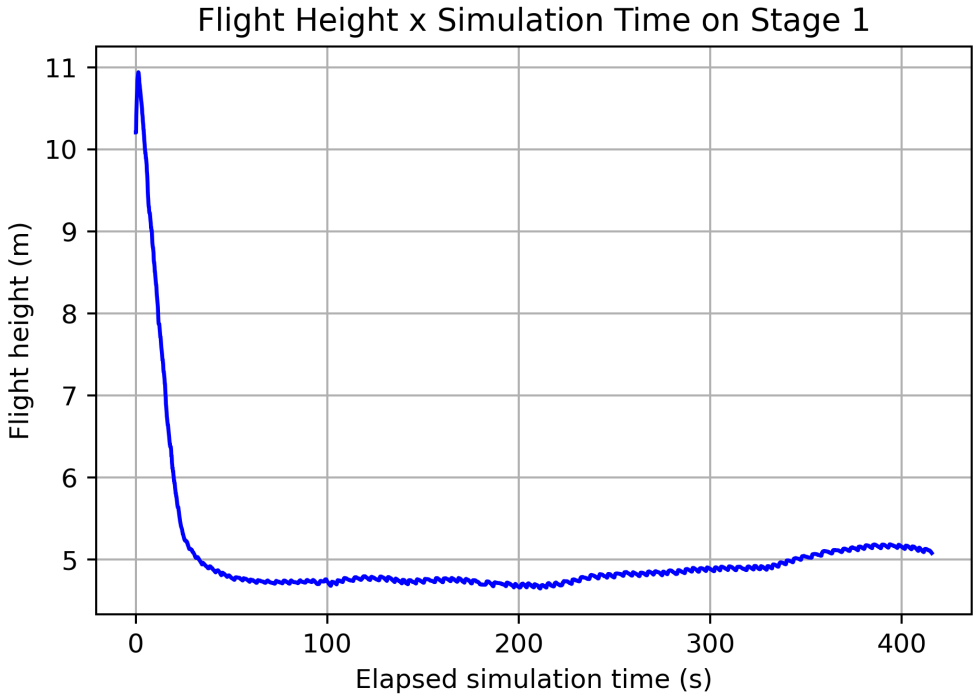


Figure IV.7: Flight height in simulation step 1 (elaborated by the author).

The takeoff height was around 10 m for safety reasons, but the UAV quickly goes to flight height and maintains it during step 1 execution. There are some deviations caused by aerodynamics and inertial conditions, but the controller performs reasonably well, fixing the setpoint's flight height. Therefore, it also justifies the presumed fixed z position in EKF modeling due to the reliable native PX4 altitude controller (PixHawk 2021).

Another important parameter of trajectory planning for the first step was drone orientation. For each (x, y) point of the calculated trajectory, a z height and a desired yaw (orientation) were associated. The initial orientation is the destination's direction, varying $\pm 90^o$ through the trajectory (depending on the destiny direction), to maintain the objective always in FOV. Figure IV.8 presents UAV orientation results during operation step 1.

When the trajectory begins, the orientation is approximately -90^o, and it varies linearly to approximately -180^o, satisfying the designed model and proving the efficiency of orientation angle control. At the end of operation step 1, the UAV faces the objective at approximately 43.908 m from the goal. The next step is the approach to the destination guided by vision.

As already stated, at the end of the first stage, the UAV was almost 41 m above the final point

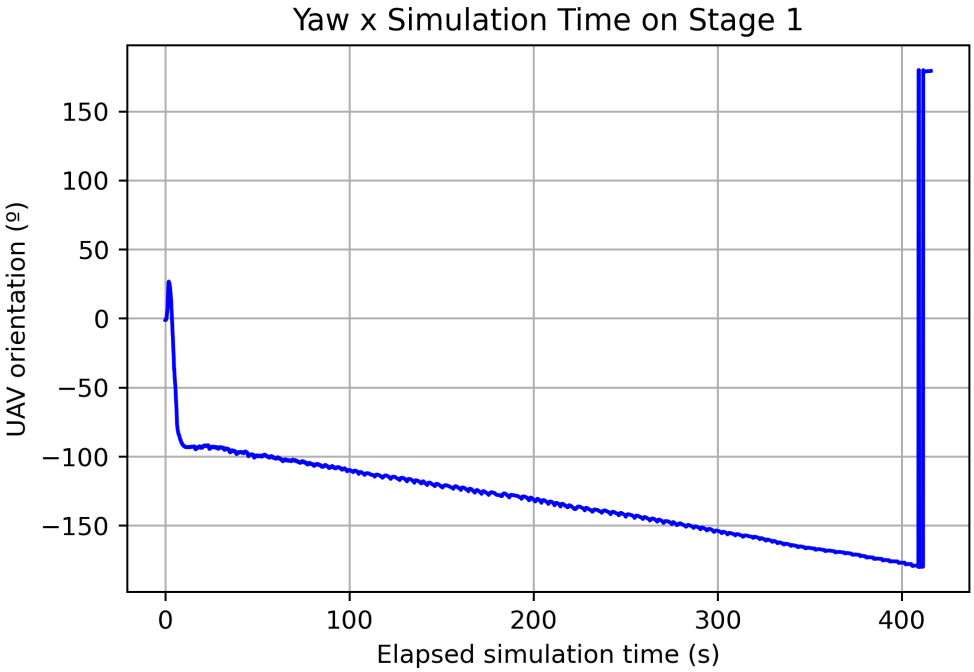


Figure IV.8: Drone orientation in simulation step 1 (elaborated by the author).

level (the flight height at stage 1 was 5 m above the takeoff point, and it is 36 m above the final spot), and approximately perpendicular to the destination vessel in a way that the YOLOff could detect the ship and all its generic regions. As exposed in methodology, the controller considered the altitude as fixed, so the UAV began to lower its altitude until it reaches approximately the final point level, and then it began to approach the delivery spot as planned. Figure IV.9 presents the performed trajectory to approach the destination using the described controller methodology.

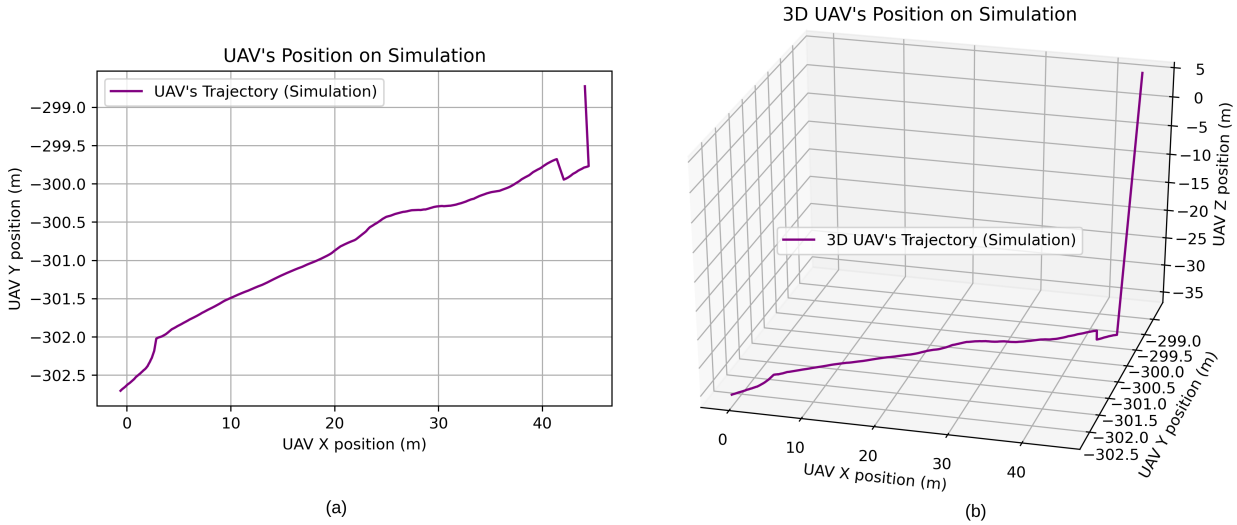


Figure IV.9: Approach trajectory results. (a) 2D trajectory (XY plan) (b) 3D trajectory (elaborated by the author).

The UAV was able to approach the destination vessel smoothly, with a maximum flight speed

configured as 1 m/s (far below what can be performed). It took 4.380 min to navigate around 44.889 m (the desired distance between the UAV and the vessel at the end of stage 1 was 50 m) until being able to detect the final QR Code marker. Figure IV.10 presents the yaw measurements of the simulated UAV, as well as EKF predictions using the presented strategy.

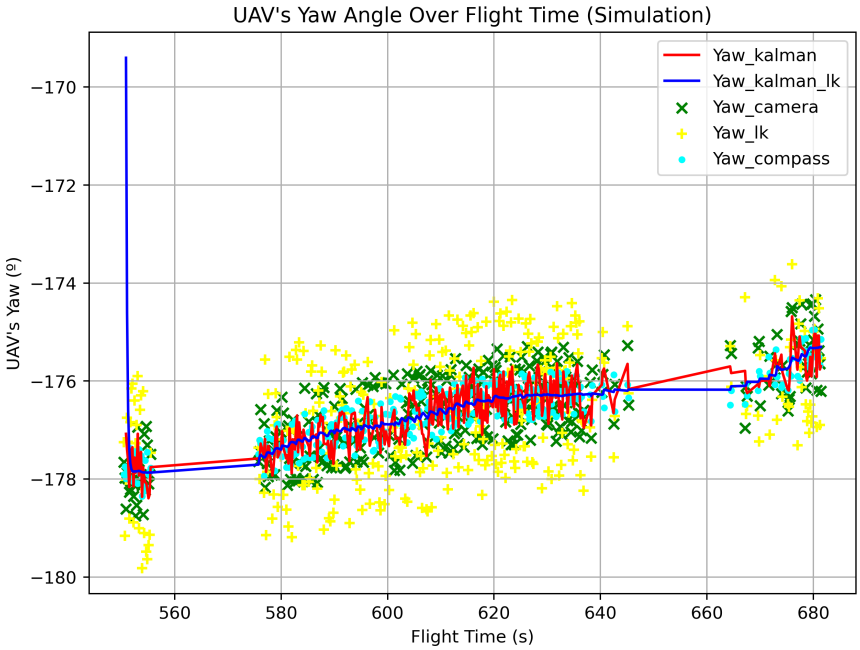


Figure IV.10: Yaw readings and prediction during simulation (elaborated by the author).

Besides the higher initial error due to the arbitrary configured high covariances within the EKF model, the predictions fusing the three sensors (compass, YOLOff e Optical Flow predictions) are much less noisy than the prediction without using Optical Flow, which also is less noisy than the compass readings, the most reliable sensor for yaw. The proposed yaw correction controller based on computer vision revealed to be a robust inertial navigation strategy for the final point approach.

After detecting the marker, the UAV was able to hold its position with 1.199 m of Root Mean Squared Error (RSME) and 0.813 m of MAE, comparing the distance of the fixed marker point to the origin and the GPS distance of the UAV to the origin. These results are presented in Figure IV.11, and Figure IV.12 shows the detection within the simulation world.

This result simulation shows that the UAV was able to autonomously take off and reach the final point as designed and presented in methodology, describing a trajectory similar to the one proposed in Figure III.5, navigating without using expensive GNSS sensors (e.g., RTK/PPK), which would be extremely susceptible to electromagnetic interference due to the vessel's communication and satellite equipment. The results also presented that the proposed methodology is a reliable backup inertial navigation alternative to be used with the cited GNSS UAV navigation, giving robustness to the system. Figure IV.13 shows all the paths navigated by the UAV within the simulation.

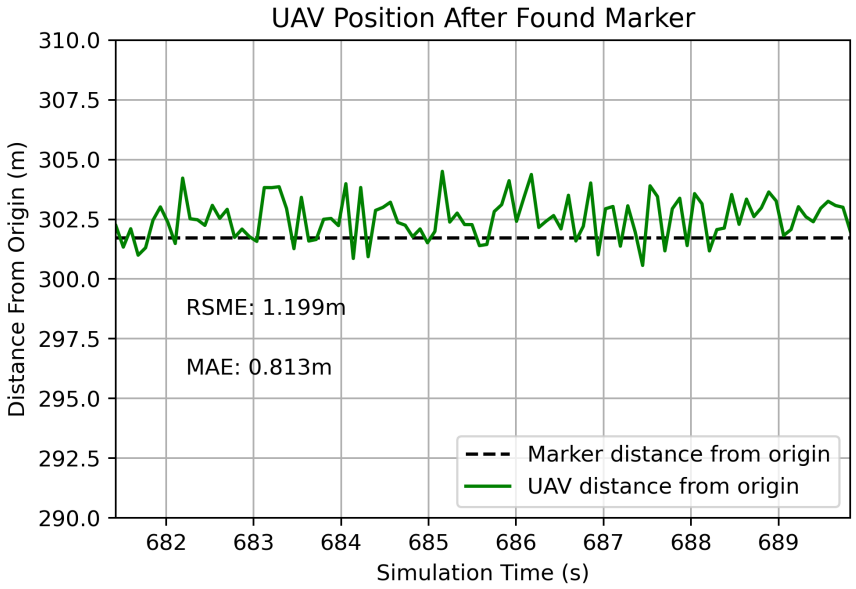


Figure IV.11: Marker detection results (elaborated by the author).

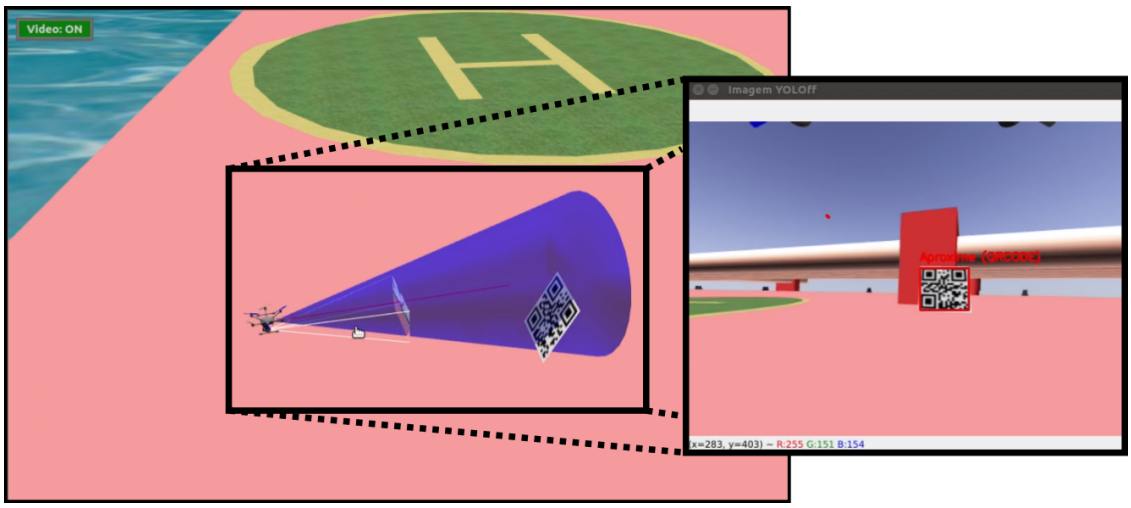


Figure IV.12: Marker detection on simulation (adapted from (Ramos et al. 2021)).

IV.3.1 Messenger Line Considerations

The final point is located approximately 36 m below the takeoff point. At the end of stage 1, the UAV was 41 m above the destination and 301.6914 m from the takeoff point. Using the messenger line's characteristics described in Table IV.4 and Equation III.10, the traction applied to the messenger line would prevent the cable to touch the water surface would be 13.0422 N.

The UAV must be able to carry the messenger line's weight, support the traction applied to the line, and deal with environmental forces. In order to maintain the cable above water at the maximum distance, it would have to deal with a payload of approximately 20.519 kg, considering almost 12 kg for the 301.6914 m of rope's weight, around 5 kg (more than double of the calculated) of line's traction to maintain it above water and a surplus of 5 kg representing external environmental forces acting on the

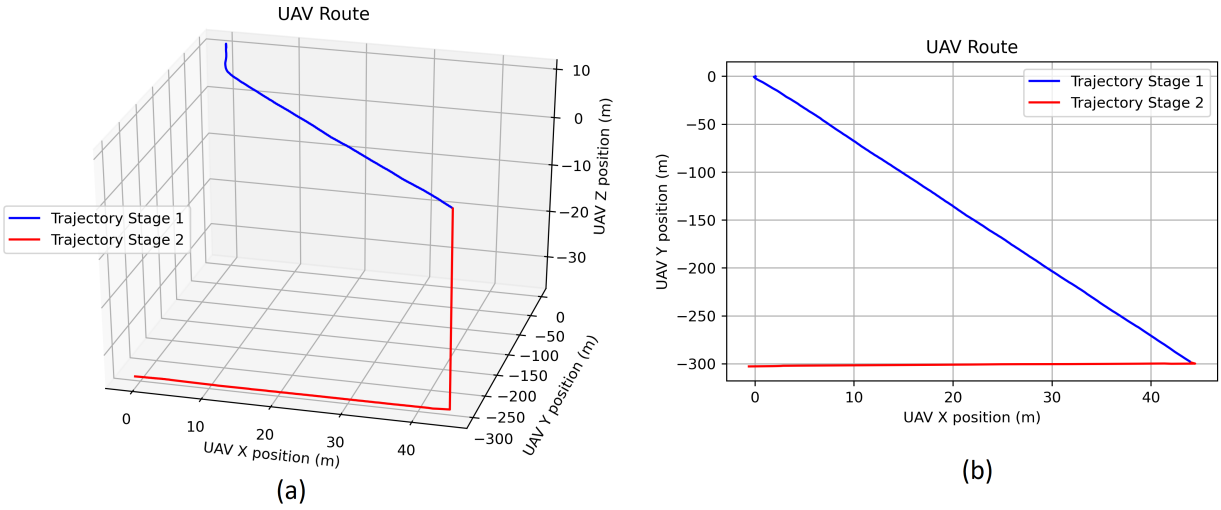


Figure IV.13: UAV's trajectory in simulation. (a) 2D executed trajectory (XY plan) compared to planned. (b) 3D executed trajectory compared to the direct ideal (Ramos et al. 2021).

Table IV.4: List of messenger line's parameters.

Variable	Description	Value	Unit
L	Distance between points	301.6914	m
z_m	Maximum height	41.0	m
w	Fluctuated weight on air	0.0469	kg/m^3
A	Transversal cable section	$3.2169 \cdot 10^{-9}$	m^2
E	Elasticity modulus	$11.6 \cdot 10^8$	Pa

UAV's body.

It is also important to highlight that the distance is an exaggeration, once the shooting position of the messenger line's launching demands that the ship and the oil rig must be 50 m apart. To meet the safety improvements required, a distance of 100 m to 150 m to receive the messenger line would be a considerable improvement. Hence 301.6914 m is much more than what would be experienced in a real operation. This serves as an estimate for the proposed application viability, indicating that a heavy-lifting UAV would be necessary, such as in (VulcanUAV 2021), a robust UAV that can transport around 25 kg of payload and is also water resistant.

A proposed solution to simulate the messenger line dynamic forces and their effects on the UAV's flight is based on (Chang e Padr 2020), where the thin messenger line in the simulation will be modeled based on the Gazebo's "fire hose model". This model considers a fire hose which is composed of cylinders connected by spherical joints. The model was modified to make the cylinder's radius smaller, as well as its length bigger. The mass and inertial parameters of each cylinder link in the "hose" were also modified to behave more like the thin messenger line in simulation. Figure IV.14 presents the schematic of the line model used in simulations.

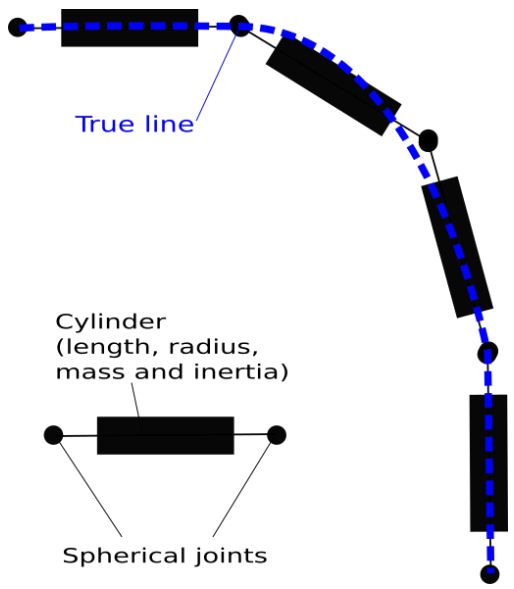


Figure IV.14: Messenger line model for simulations.

In practical terms, the main dynamic forces issues to be experienced by the UAV are due to the line's length, which will increase mass over time, and the drag effects caused by the wind acting on the messenger line. Therefore, in simulation, each cylinder link will be subjected to wind drag (D) and weight (W) forces, as presented in Figure IV.15. For each link, the resultant (R) will be solved, and therefore the simulated UAV will be subjected to a resultant force.

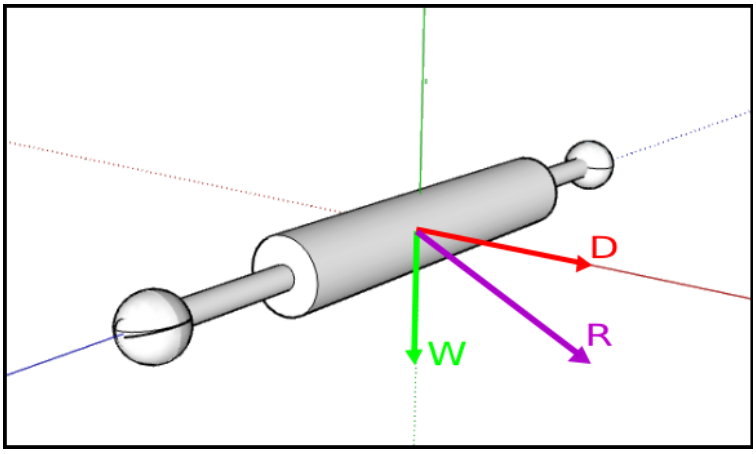


Figure IV.15: Dynamic forces acting on a line model link.

The weight force W, always pointing downwards, will be solved by:

$$W = m \cdot g \tag{IV.1}$$

, where m is the link mass and g is the gravity acceleration. The drag force will be solved on each link

by:

$$D = \frac{\rho.C.A.v^2.\sin\theta}{2} \tag{IV.2}$$

, where ρ is the air density, C is the coefficient of drag, A is the cross area over which the wind is striking, v is the relative velocity between the line model link and the wind and $theta$ is the angle of incidence of the wind over the cross area.

With two forces calculated in each link, it is possible to obtain the resultant vector force acting along the line. As the vehicle gets apart from the takeoff point, equation III.10 will be applied to verify the tension force necessary for the line not to touch the water surface. In order to verify the dynamic effects on the UAV, it will be analyzed its roll and pitch angles, as well as the vibration in these axes. This will indicate if the UAV is struggling to carry the line due to the weight and drag of the cable. Thus, these results can be used to ensure the methodology's feasibility.

In order to verify the methodology feasibility, it is proposed to replace the normal messenger line used in operations with a thinner and lighter wire, such as a braided microfiber line (Rikimaru 2020). The typical messenger line must serve as a guide for the ship to pull the mooring link composition, so it has a breaking strength of the order of 500 tons. However, these lines have a linear weight of around 30 g/m and a diameter of 10 mm. The replacement strategy consists of delivering the thinner line to the ship, then using it to pull the typical messenger line, continuing the operation as usual. As Typhoon H480 couldn't deliver the normal messenger line. The simulation considered this thinner and lighter line to accomplish the task, which has breaking tension of 38.6 kg in the diameter of 0.5 mm, with a linear weight of 0.49 g/m (Rikimaru 2020). So, more than enough to be carried out by the simulated UAV and then being used to pull the normal messenger line. Figure IV.16 presents the line in simulation.

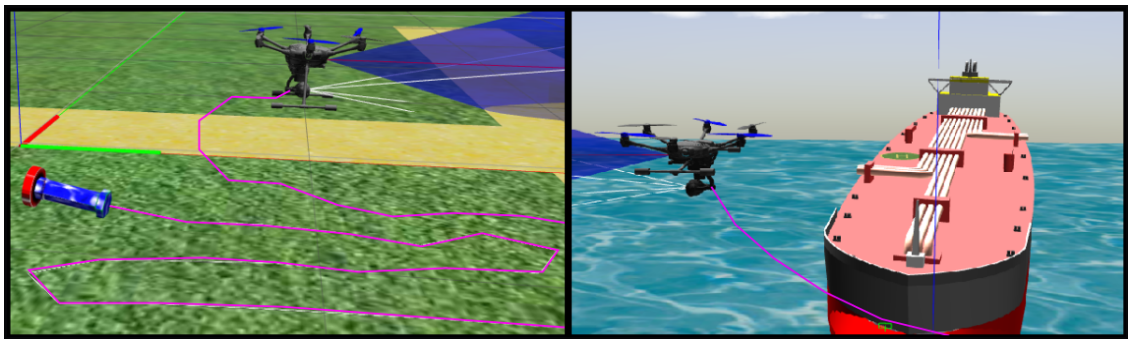


Figure IV.16: Messenger line in simulation.

For this simulation, it is necessary 350 links of 1 m each were used with the mass of 0.49 g per cylinder (sphere joints were configured without weight) and 0.5 mm of radius, the same used in the spheres. This modeled line was so thin and light that the equation III.10 couldn't be applied to it since it is applicable only if the tension in the cable is larger than the weight of the cable (the total weight

for the 301.716 m maximum distance is 147.841 grams). The model couldn't be graphically simulated due to its size and interaction between the joints between the line's cylinders, but the calculations show that the Typhoon would be able to successfully deliver this line without the catenary even touching the water surface. To evaluate the simulated UAV behavior and stability for this application, Figure IV.17 shows the vehicle's pitch and roll angles and also the vibration on the yaw, pitch, and roll axis.

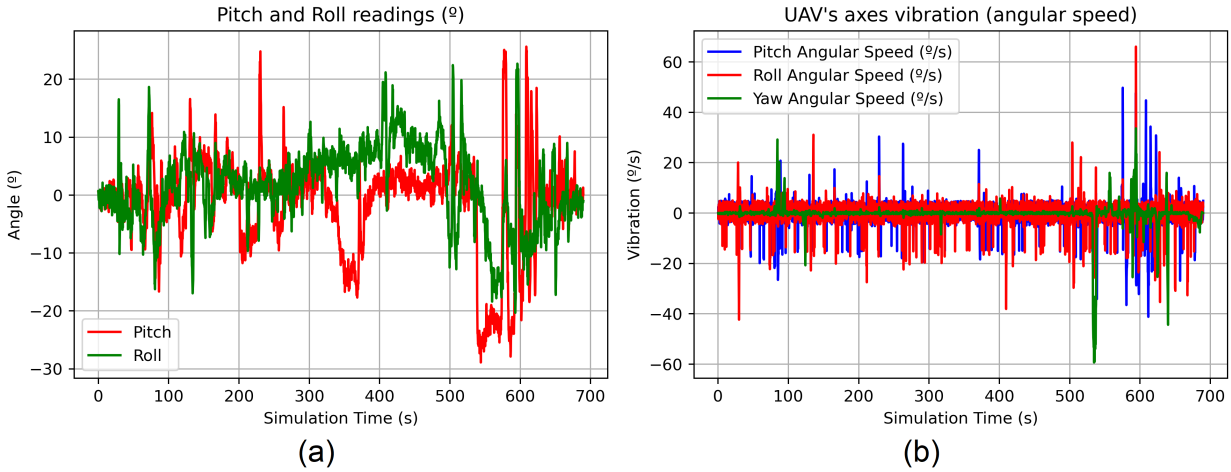


Figure IV.17: Typhoon H480 pitch and roll angles (a) and vibration (b) transporting the line in simulation.

As the manual describes (Yuneec 2020), the maximum rotation angle is $\pm 35^o$ and the maximum rotation rate is $\pm 85^o/s$. In the simulation, the vehicle behavior was framed within these stability parameters, facing more vibration in the last stages where the visual-inertial navigation was active. The vehicle presented very stable behavior and operated far from the stability limits imposed by the manufacturer, assuring the methodology feasibility given the considered models.

IV.4 Scale test

Due to space restrictions, the test on a real UAV was performed only on the second operation stage, which is the destination ship approximation guided by computer vision detailed before. The test was conducted on an empty parking lot in Rio de Janeiro, Brazil. The purpose of the test was for a real UAV to take off, detect a cardboard model ship (Figure IV.18), and then approximately do the delivery spot. This spot is configured as the model's mid-ship region, recognizing the final destination in that region represented as a QR Code marker (the same used in simulation). The controller used in this test is the same as the simulation since the developed system based in MavROS was theoretically ready to be used on a real robotics system with a PixHawk Px4 FCU configured with Autopilot firmware.

The UAV used in the real test is a hand-built quadrotor using an S500 frame (Figure IV.20). The FCU is a PixHawk Px4 with the Autopilot firmware. The UAV's setup diagram is presented in Figure IV.19.



Figure IV.18: Ship model used for real tests (elaborated by the author).

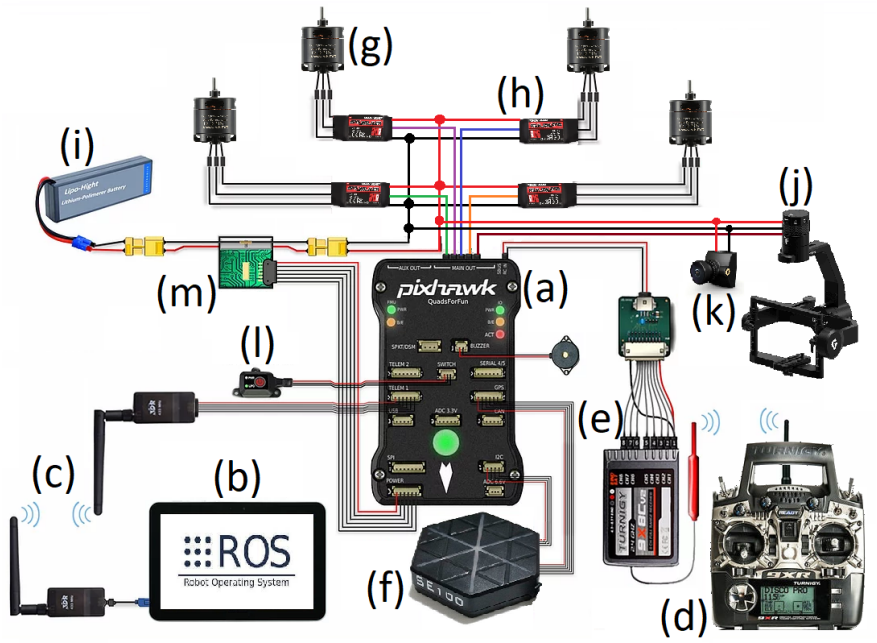


Figure IV.19: Test UAV setup: (a) PixHawk Px4 FCU; (b) Base station running ROS system; (c) MavLink telemetry radio; (d) Turnigy 9XR radio; (e) RC receiver; (f) SE100 GPS Module; (g) [4x] Sunnysky 720KV brushless motor; (h) [4x] Hobbywing 40A Electronic Speed Controller; (i) Tattu 4 cells 5200mAh LiPo battery; (j) Camera gimbal; (k) Eachine TX03 NTSC FPV Camera; (l) Safety killswitch; (m) Current sensor (elaborated by the author).

The real test method consists of: the UAV starts on the ground when the controller ROS node is initialized. The controller sent the autonomous takeoff command to the FCU, which is a native MavROS package. When the takeoff is finished, the camera node must detect the ship and its regions to process the information and send the same flight commands presented earlier. The camera node receives the



Figure IV.20: UAV used in real tests (elaborated by the author).

camera's image through the analog FPV receiver. If the model ship is detected, the yaw is processed, and the velocity commands are parsed to the FCU through MavROS. The controller is designed to fix a flight height, which the FCU tries to maintain autonomously as the velocity on the (x, y) axis referred to UAV's body is modified while the vehicle navigates in the target's direction. The vehicle will stop if the safe limit is reached (in this case configured to 1 m, which is a precision very hard to accomplish with simple GPS) or if the final marker is detected. When the marker is detected, the vehicle will maintain its position until the mission is stopped, then it will return to the home point and land.

Due to technical limitations, the test with the real UAV was performed only for the approaching step. The UAV was initially positioned on the ground, approximately perpendicular to the vessel's model. Therefore the controller is programmed only to take off and begin the approach to the vessel's model using the described and simulated methodology. The test was conducted on march 30^{th} 2021 in Rio de Janeiro, Brazil.

Figure IV.21 presents the approaching process in the test. In this same way, Figure IV.22 shows the trajectory from takeoff until the UAV finds the marker on the model, and IV.23 shows the performed trajectory related to the map.

The approach to the vessel's model was executed with an MAE of 0.523 m between the executed trajectory and the ideal direct trajectory as shown in figure IV.22. The flight height presented an MAE of 0.197 m. This seems high on the figure, but this is caused because the controller was set to fly at 1.2 m since the marker was around 1.15 m above the ground. Still, with this height, the altitude controller becomes unstable due to proximity to the ground. Nevertheless, the controller worked without any issues, presenting a smooth behavior on correcting the UAV's yaw and allowing the vehicle to approach and locate the marker. Figure IV.24 presents the yaw angle during the test.

The prediction used on the flight was the EKF fusing all three readings, but for comparison analysis, it was plotted the EKF fusing only the compass and YOLOff estimation. This time, the two EKF would behave very alike, but still, the tree-sensor prediction has less abrupt variations, despite the slightly high

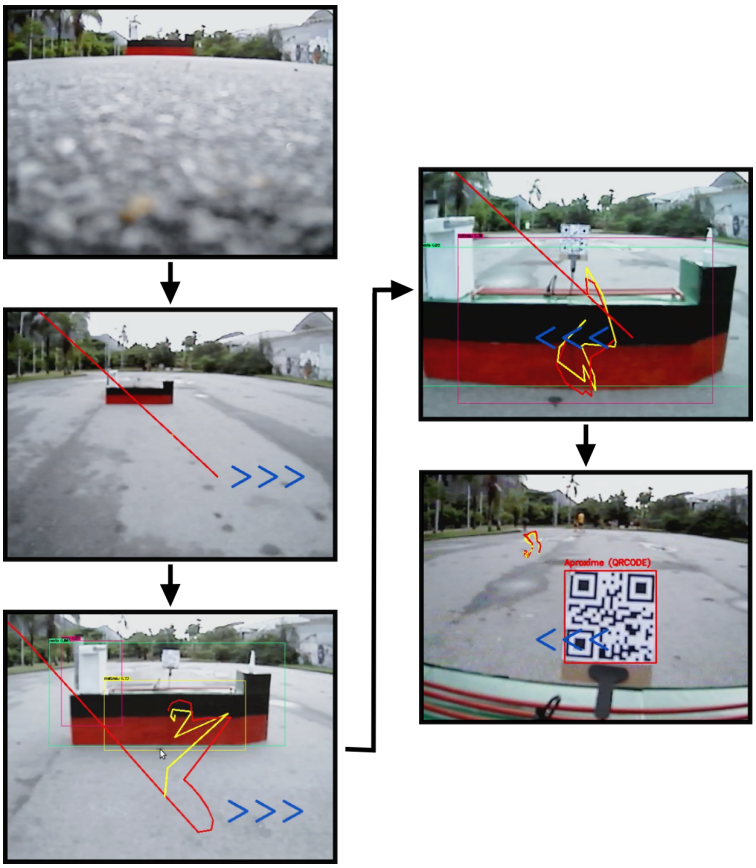


Figure IV.21: Controller test on real UAV.

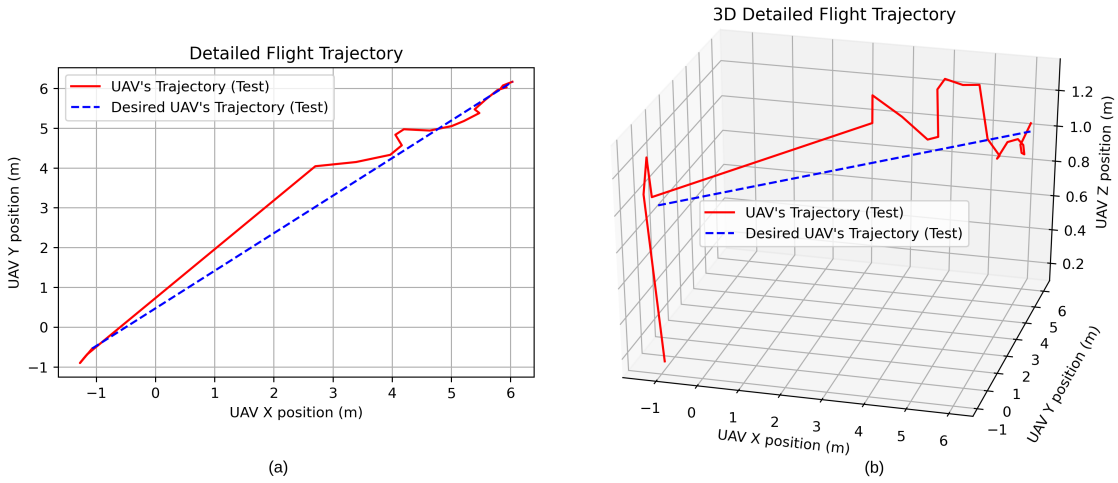


Figure IV.22: Real UAV's trajectory in test. (a) 2D executed trajectory (XY plan) compared to the desired direct navigation. (b) 3D executed trajectory compared to the desired direct navigation

initial error. In the same way, as in simulations, the proposed methodology proved to be a good inertial flight strategy.

IV.5 Field test

The test was executed in an offshore environment, aboard an FPSO, with an average wind speed of 13.4 knots (26.05 m/s) and a wind gust of 15 knots (29.16 m/s). Since an offloading operation was



Figure IV.23: Real test trajectory on map

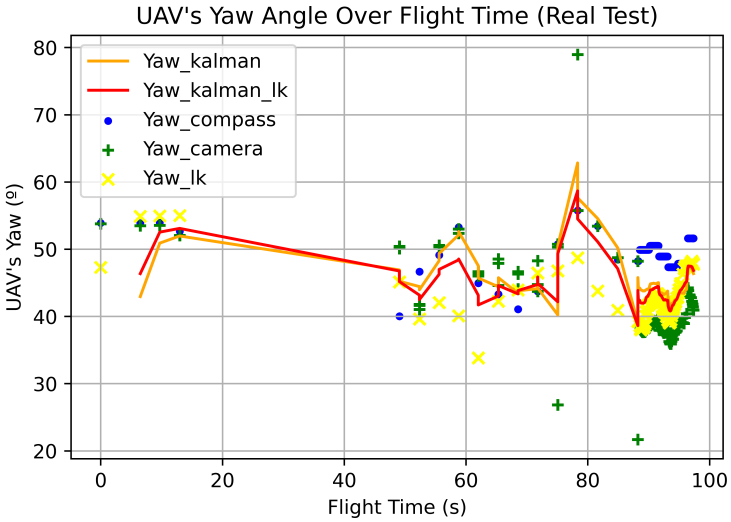


Figure IV.24: Yaw during the test on real UAV.

not happening during the test window, it was performed only using the oil rig.

For the EKF approaching VI navigation, the UAV was positioned at a distance of 280.12 m from the oil rig's port, having the structure entirely in its FOV. When the algorithm was started, the UAV began to approach the QRCode (or delivery point) coordinate using the developed VI controller to maintain the direction of flight. The UAV successfully identified the marker at the end of the trajectory within 1.39 min, besides the wind drag. Figure IV.25 shows the VI navigation test camera's image until it finds the marker and Figure IV.26 presents the executed trajectory.

Finally, the EKF behaved very well, predicting yaw orientation with robustness and less noise than the other readings. This allowed yaw correction and navigation commands to anticipate high drifting. Figure IV.27 presents the EKF behavior during the flight.

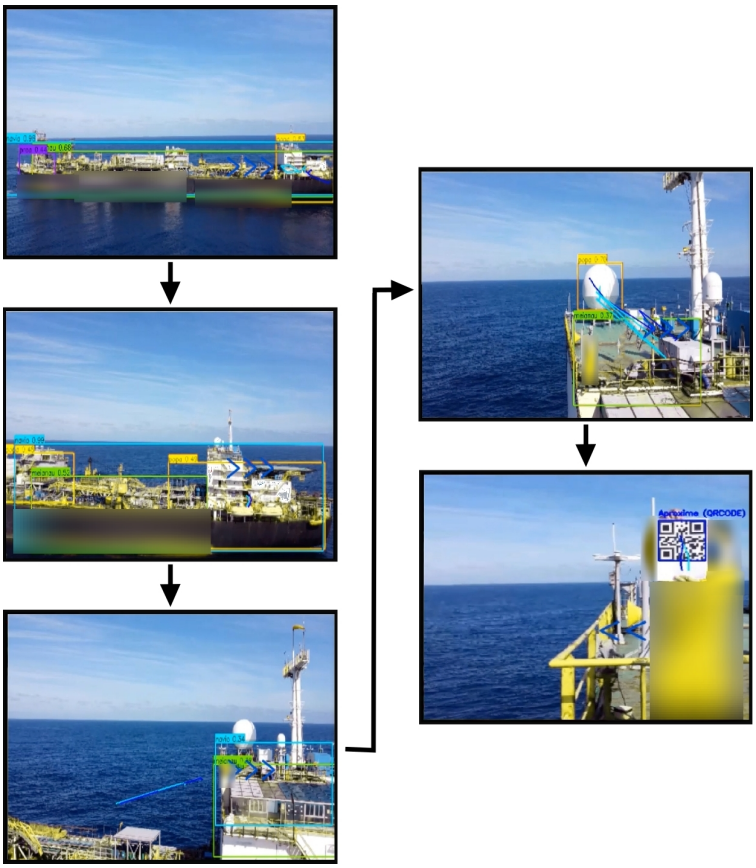


Figure IV.25: VI approaching navigation in field test.

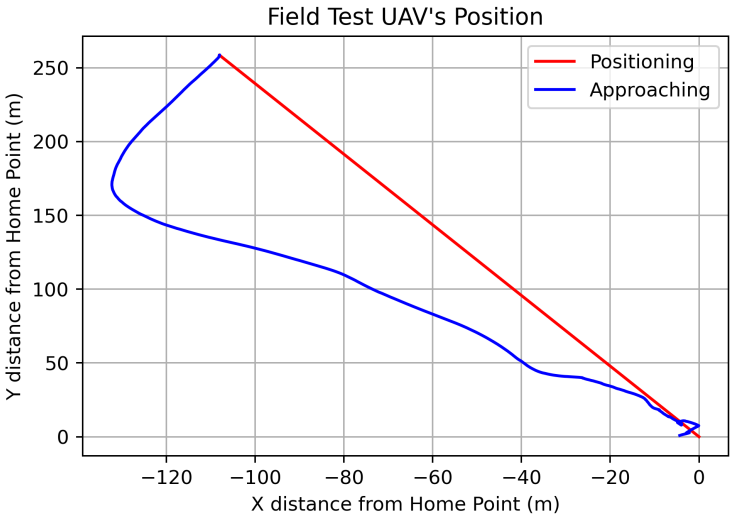


Figure IV.26: VI approaching navigation in field test trajectory log.

IV.6 Economic Evaluation

IV.6.1 Final Year of Production Scenario

For this scenario, based on the harmonic decline production curve presented in the methodology section, Table IV.5 presents the oil average daily production of the FPSO for the described hypothetical

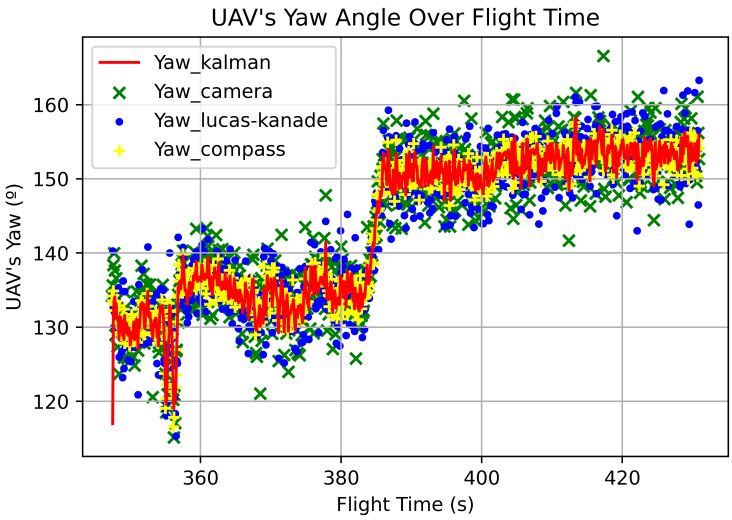


Figure IV.27: Yaw readings during VI approaching navigation field test.

simulated scenario. Every production q on Equation III.33 was associated with a certain month t, and the result was divided by 31 (to transform $m^3/month$ into m^3/d) and multiplied by an random Gaussian factor in the interval $[0.5; 1.5]$ to simulate production oscillations, as seen in Figure III.11.

Date (mm/yyyy)	Production (mș/d)	Date (mm/yyyy)	Production (mș/d)
01/2021	2057.57	08/2021	1967.61
02/2021	2042.92	09/2021	1957.24
03/2021	2027.08	10/2021	1946.69
04/2021	671.45	11/2021	1937.15
05/2021	2001.12	12/2021	1913.92
06/2021	1990.10	01/2022	1690.85
07/2021	1978.44	-	-

Table IV.5: FPSO's Estimated Daily Production.

Based on data of the FPSO, the operational storage capacity was considered $196.300m^3$ and the oil ballast in cargo tanks $107.453m^3$. As described in Equations III.35 and III.36, the considered V_{off} volume based on average offloading volumes performed with this FPSO is $45.000m^3$. The initial oil inventory on cargo tanks, based on internal data, is $133.690m^3$. So from this amount, every n day a production P_n will be added to the total inventory based on Table IV.5, from day $01/01/2021$ to $31/01/2022$.

However, whenever the available volume for offloading reaches $45.000m^3$ or more, an offloading operation will be considered in the simulation. The offloading volume decrease must never leave the total oil inventory below the ballast volume, except after $31/12/2021$, when the production is finished,

and the oil ballast will be transferred for the rig's decommission. Figure IV.28 represents the oil inventory evolution projected for these simulations and also the offloading operations during this time.

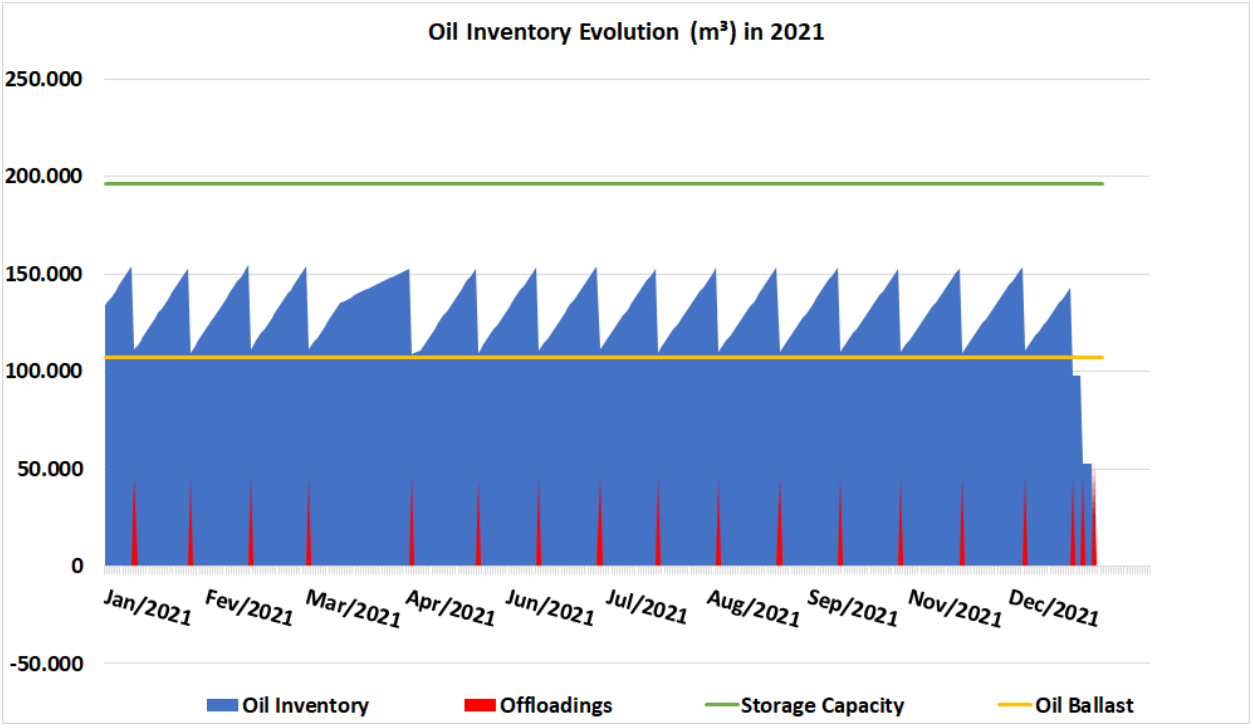


Figure IV.28: Oil inventory evolution in economic simulated scenario (Ramos et al. 2021).

Also based on FPSO's historical behavior, the average pumping flow considered for pumping time calculation is $1880m^3/h$, the average time took in initial and final works is $30.02hours$ and $10.06hours$, respectively. The considered resources tariffs for each operation are presented in Table IV.6.

Resource	Tariff
Shuttle Tanker	1764,67 US$/h (BRS 2020)
AHTS	2226,23 US$/h (Clarksons 2020)
LH	12546,99 US$/Operation (DSB 2020)
Maneuver Captain	11791,70 US$/h (Brokers 2020)

Table IV.6: Resources Tariffs.

Now, it is possible to calculate the M_{TOTAL} costs and its parcels for a typical offloading operation according to Equation III.37. To compare economic results, there is just a need to calculate the M_{TOTAL}^{UAV} for each offloading. As stated, just the M_{LH} costs will be changed by a M_{UAV} cost, which will be composed of an investment parcel on the first month (CAPEX) and operation, crew training, and maintenance.

The CAPEX will be chosen from Table IV.8, added all Brazilian taxes and additional from Table IV.7, converted in dollars. For this work, the Vulcan UAV Airlift (VulcanUAV 2021) was chosen as a

viable option for investment due to its lifting capacity and flight time autonomy. Table IV.9 presents the OPEX costs simulated for the proposed solution and the frequency that each cost is associated in Equation III.44.

For crew training costs, a value of $1000USD$ are estimated for theoretical and practical onshore training of operators, and the time chosen is based on oil and gas industries' training standards for offshore workers. The operation costs of $500USD$ per operation are considering the crew man-hour to prepare the UAV, configure the initial parameters, observe UAV during flight and receive the messenger line cable (on shuttle tanker), as well as perform initial flight checks, charge batteries and verify UAV's integrity.

The maintenance is arbitrarily chosen quarterly, and its goal is to guarantee UAV integrity, recalibrate avionic sensors, and change malfunctioning peripherals such as brushless motors, propellers, electronic speed controllers (ESC), etc. It is important to notice that this work is considering that the UAV will fly only at offloading operations, and with a total of 18 operations in the considered period, there is an exaggeration in OPEX costs.

Tax	Aliquot
Tax over importation (II)	20%
Tax over manufactured product (IPI)	10%
Tax over finantial operations (IOF)	3%
Social integration program (PIS)	1.65%
Contribution to social security financing (Cofins)	7.6%
Tax on circulation of goods and services (ICMS)	18%
Tax on services of any nature (ISS)	5%
Homologation fee of the National Civil Aviation Agency (USD)	100

Table IV.7: Brazilian considered taxes.

UAV	Payload (kg)	Maximum Wind Speed (knots)	Water Resistant	Autonomy (min)	Price after taxes (USD)
Vulcan UAV Airlift (VulcanUAV 2021)	25	33	Yes	20	33150
Green Bee 1200 (AZDrone 2021)	20	-	-	20	30403.21
Freefly Alta 8 (FreeFly 2021)	18	20	Yes	16	31388.66
Onyxstar Hydra 12 (OnyxStar 2021)	12	24	Yes	30	9437.62
Drone Volt Hercules 20 (DroneVolt 2021)	20	30.4	Yes	40	24947.01
Tarot T-18 V2.1 (UAVSystems 2021)	8	14	No	25	6526.14
Inspired Flight IF1200 (InspiredFlight 2021)	8	20	No	40	46333.15

Table IV.8: Selected UAVs, characteristics and investment costs.

Finally, Table IV.10 presents the cash flow results M_{TOTAL_m} and $M^{UAV}_{TOTAL_m}$ at the end of each

Cost Description	Value	Frequency
Crew training	1000 (US$)	First 10 weeks
Operation cost	500 (US$)	Per operation
Depreciation	20%	p.a.
Maintenance	1000 (US$)	Quarterly

Table IV.9: UAV operational costs.

m month for the simulated period. Also are presented the brute difference (gain) between the costs of normal offloading operations and the operations with the proposed robotics solution for each month G_m and the accumulated gain AG_m. Figure IV.29 represents a graphical visualization of the cash flow and the Figure IV.30 shows the accumulated cash gain.

End date	m	M_{TOTAL_m} (US$)	$M^{UAV}_{TOTAL_m}$ (US$)	G_m (US$)	AG_m (US$)
31/01/2021	0	-280341.69	-306493.43	-26151.73	-26151.73
28/02/2021	1	-561729.99	-542206.28	19523.70	-6628.03
31/03/2021	2	-281389.28	-271931.27	9458.00	2829.98
30/04/2021	3	-281914.54	-271430.20	10484.34	13314.32
31/05/2021	4	-282440.78	-270926.29	11514.48	24828.80
30/06/2021	5	-282968.00	-271430.82	11537.18	36365.98
31/07/2021	6	-566992.41	-544240.34	22752.07	59118.05
31/08/2021	7	-284025.40	-272442.69	11582.71	70700.76
30/09/2021	8	-284555.58	-272950.05	11605.53	82306.29
31/10/2021	9	-570173.50	-546271.33	23902.17	106208.46
30/11/2021	10	-285618.91	-274988.33	10630.58	116839.04
31/12/2021	11	-286152.07	-274477.80	11674.26	128513.31
31/01/2022	12	-877173.05	-841815.06	35357.98	163871.29

Table IV.10: Economic results.

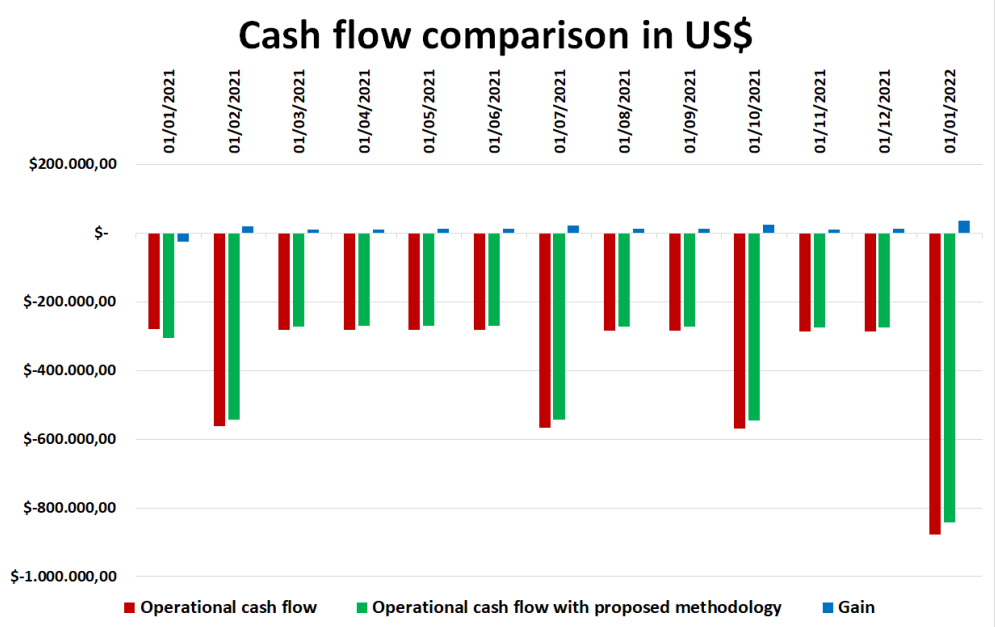


Figure IV.29: Cash flow comparison for each simulated month (Ramos et al. 2021).

Based on the projected dollar inflation of 0.29% per month for 2021 and set it as the minimum interest rate, Table IV.11 presents the estimated net pay value for both normal offloading operations

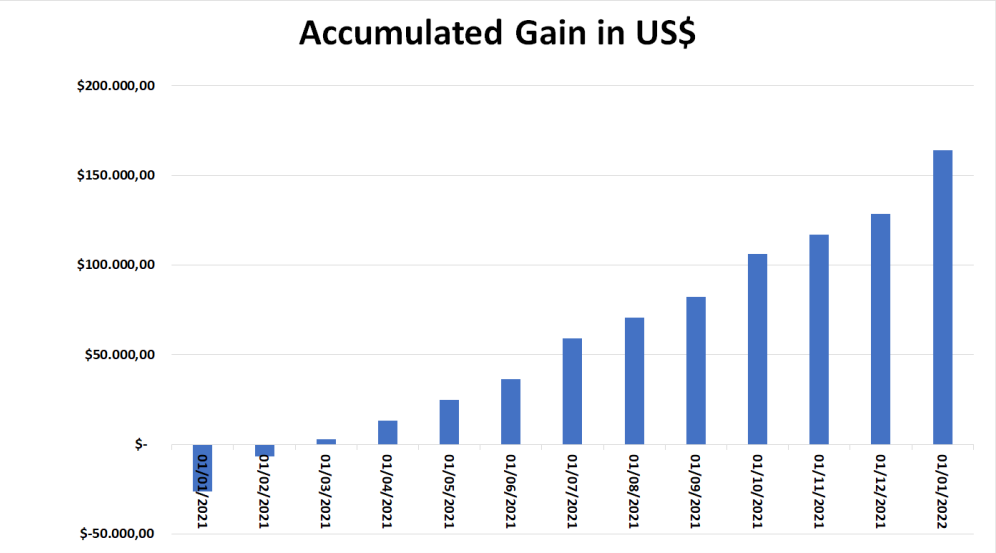


Figure IV.30: Accumulated gain on simulated period (Ramos et al. 2021).

and offloading operations with the robotics methodology applied in the simulated economic scenario. The table also presents the total gain (the brute difference between the two offloading operations as stated in Equation III.16) and internal rate of return per month, as in Equation III.17.

Economic Indicator	Value
NPV	USD -5,014,194.19
NPV_{UAV}	USD -4,854,667.74
TG	USD 159,526.46
IRR	55% per month

Table IV.11: Economic indicators.

Therefore, the presented economic results and indicators show that the proposed solution is attractive, with the gain (cost reduction) of $USD159,526.46$, an accumulated cash flow gain of $USD163,871.29$ from an investment of $USD33,150.00$, within a 2-month payoff, as shown in Figure IV.30. The internal rate of return shows a positive result of 55% per month, far greater than the considered minimum interest rate of 0.29% per month, which is the projected dollar inflation for 2021.

The robotics simulation results also prove the technical feasibility of the proposed methodology. As designed, the UAV was able to take off from the FPSO helipad, perform the initial flight stage only guided by a calculated route without serious deviations, and then, safely approximate to the destination vessel guided only by computational vision, and also using it to recognize the delivery point marker. Due to GPS systemic errors and noises, this navigation hardly would be performed with such safety and precision using only geographically referenced flight without using more expensive technologies.

IV.6.2 First Years of Production Scenario

Once more based on the production panel for the chosen FPSO in which this scenario is based, Table IV.12 presents the offloading parameters of the new production facility according to the methodology.

Table IV.12: Offloading parameters.

Variable	Description	Estimated Value
C_n	Storage Capacity (mṣ)	211,536.128
B_n	Ballast (mṣ)	85,662.512
V_{off}	Average Offloading Volume (mṣ)	82,081.642
P_n	Average Production (mṣ)	23,548.250
Q_{off}	Pumping Flow (mṣ/h)	6300
$t_{i_{off}}$	Initial Works Time (h)	6.920
$t_{f_{off}}$	Final Works Time (h)	4.155

Starting from $S_0 = 102,920$ m^3 on January 1st 2021, the oil inventory S_n was increased by P_n (with the average presented in Table IV.12) every n day. If the V_n volume available for offloading was bigger than V_{off}, an offloading of $T_n = V_{\text{off}}$ was considered on that day. If the S_n was equal or bigger than $C_n - 2 \cdot P_n$, an offloading of $T_n = S_n - B_n$ was considered on that day. In this way, Figure IV.31 presents the oil average daily production of the FPSO for the described hypothetical simulated scenario, the ballast, capacity, offloading volumes, and a total number of offloading operations accumulated per month.

After the design of the number of operations and the time taken on them, it was possible to project the resource's cost based on referenced panels prices and rates, being $R_{\text{ST}} = USD1,895.83$/h and $R_{\text{AHTS}} =$ USD $2,226.23$/h, with the AHTS projected to be used only on 40% of the operations. With these rates and operation time projections, it was possible to estimate the total offloading cost per operation, inflating the value by a total of 0.29% per month, representing the projected dollar inflation during the simulated period (BCB 2021).

To estimate investment costs (CAPEX), it was considered the Brazilian taxes and fees presented on Table IV.7, applied to the market value of the same Vulcan Airlift UAV (VulcanUAV 2021) chosen before, totalizing USD 33,211.88. This UAV was chosen due to its high payload capacity up to 25 kg, wind speed operation limit up to 33 knots (above offloading limiting), flight autonomy of 20 min, and also for being water-resistant, attending requirements of a real offshore industrial application.

As described in Section III, the cost reduction of the proposed methodology is based both on the

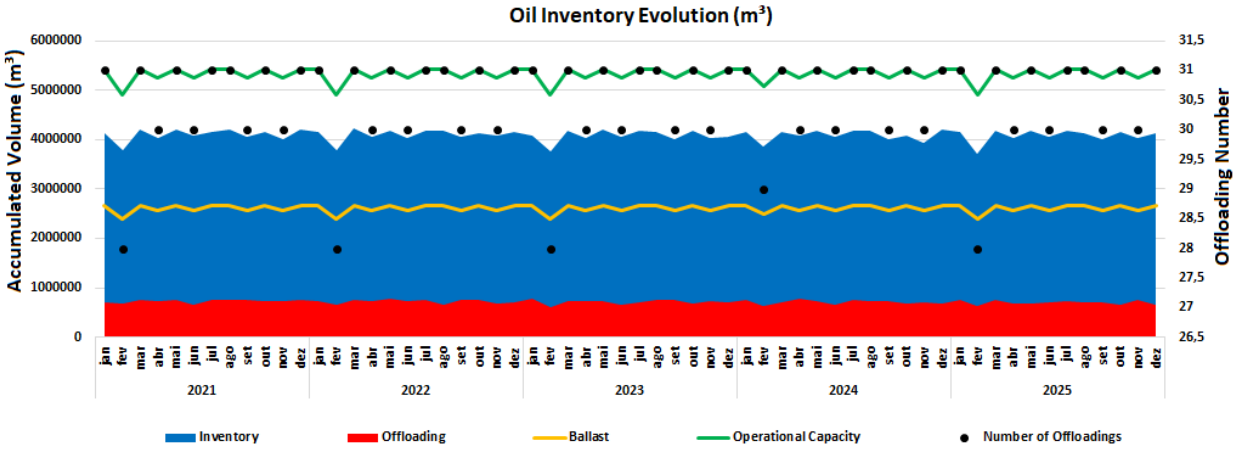


Figure IV.31: Accumulated volumes and offloading numbers by month within the economic simulation time (elaborated by the author).

resource utilization time reduction and on the operation being cheaper by itself, since it demands fewer crew-members and considerably reduces man-hour time, as well as the already presented risk reduction. The costs considered on this scenario are almost the same of the previous one, but since the UAV must have 5 years of lifespan, the maintenance is applied on each operation, and training became a cost applied every semester trough the whole project's life. The operational costs intrinsic to the OPEX of the UAV are presented in Table IV.13.

Table IV.13: UAV operational costs.

Cost Description	Value	Frequency
Crew training	1000 (US$)	Semiannually
Operation cost	500 (US$)	Per operation
Maintenance	1000 (US$)	Per operation
ST resource cost	95% x M_{ST}	Per operation
AHTS resource cost	95% x M_{AHTS}	Per operation
Depreciation	20%	Yearly

With this information, it is possible to calculate the operational costs for a normal operation and an offloading considering using the proposed UAV strategy. Figure IV.32 presents a graph showing the accumulated costs between the two alternatives within the months of the economic simulation, as well as the gain (cost reduction).

Table IV.14 presents the results in terms of present value and accumulated gain. The present cost reduction or total gain (TG) with the performed economic simulation at the end of 5 years application would be USD $2,349,811.34$, and the accumulated cost reduction per month at the end of this period is USD $3,625,388.88$. This may not seem much considering the offshore oil and gas industry, but it is an attractive return considering the investment of USD $33,211.88$, with an investment payoff in 7 offloading operations, which occur within the first month in the simulated scenario.

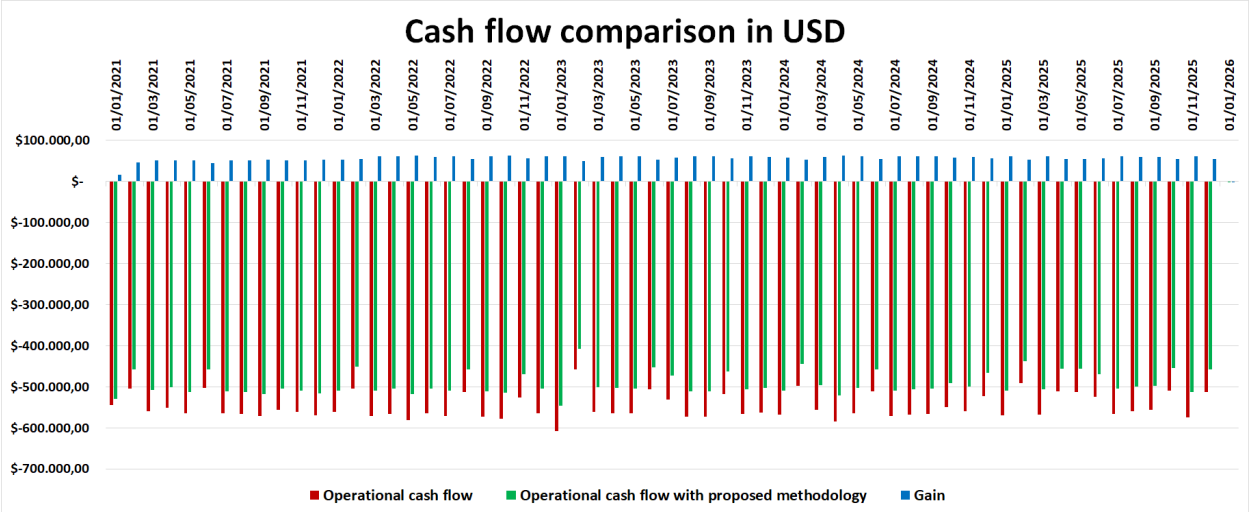


Figure IV.32: Monthly accumulated offloading costs comparison within the economic simulation time (elaborated by the author).

Also, it is considered that the UAV will serve only to one FPSO, but due to proximity between production facilities in offshore giant reservoirs, a UAV could perfectly serve more platforms. Finally, it is not financially considered the probability of not delaying or postponing an operation, as well as the financial costs of an accident, which makes the project even more attractive.

Table IV.14: Cost reduction evaluation.

Gain	Value
NPV	USD -23,087,789.80
NPV_{UAV}	USD -20,737,978.47
TG	USD 2,349,811.34
Accumulated G_m	USD 3,625,388.88

Chapter V Conclusions and Future Work

V.1 Conclusions

This dissertation presented robust results both in the simulation and in the real controlled test. In the simulation, the UAV was able to autonomously takeoff from the production facility and navigate according to the designed safe route, and guided by computer vision, safely reach the destination point with precision under 2 m. Without using expensive sensors and GNSS positioning systems, the UAV was able to accomplish the objective with satisfactory precision. The simulation also attests that the proposed framework may be used as a backup for more robust inertial navigation techniques for UAVs, but that can be subject to failure (satellite dropouts due to ship's communications interference, for example).

The scale tests on the controlled environment validated the simulation results and also confirmed that the developed controller packages with ROS and MavROS are fully ready for a real field test. The UAV behaved in a reasonable manner, also being able to autonomously take off and reach a determined point on the open field with a precision that would be hardly achieved using only simple GPS positioning. Furthermore, the field test confirmed that the developed framework presents a solid solution for the presented problem, as the essay demonstrates that the approaching strategy to find the QR marker worked fine, allowing the UAV to autonomously find the delivery spot with efficiency and safety.

About the economic evaluation for the system's application, the results presented solid return over the invested value, beyond the mapped and described possibilities of risk reduction, therefore preventing monetary, environmental, and humanitarian damage. The efficiency improvement also must be taken into account since the operation with the UAV is less susceptible to several meteorological and oceanographic conditions, improving reliability on operation's programming and resources allocation, as well as a possible reduction in the hired fleet since a resource time in one operation will reduce.

V.2 Future Propositions

In terms of evaluation, this research opens up several future works. For instance, in future implementations, there's still a need to use the detected marker as approximation controller feedback. Also, the aerodynamics, inertial forces, and messenger line's dynamic forces have to be taken into account in

the simulation, such as the ship's movements during the operation. The messenger line cable has to be coupled in the UAV on the simulation, and its effects on the flight must be analyzed on the UAV's flight behavior before trying to test the offboard controller on the real proposed environment.

The proposed methodology also makes way for a new robotics application in offshore production facilities operations, explored for very few reports in the literature, although there's still a need to test and evaluate the full route navigation strategy in a real controlled environment. The robust dynamic controller must be designed, simulated, and tested as well, considering the messenger line's dynamic forces acting on the vehicle. Also, for the methodology validation, a test mission must be performed in a real-scale offshore environment, using a working industrial-class UAV to evaluate risks and difficulties before preparing guidelines for a continuous application of this technology.

Bibliography

AGHDAM, H. H.; HERAVI, E. J. *Guide to Convolutional Neural Networks: A Practical Application to Traffic-Sign Detection and Classification*. 1st. ed. [S.l.]: Springer Publishing Company, Incorporated, 2017. ISBN 331957549X. Cited on page 25.

AHMED, S. F. et al. Attitude stabilization of quad-rotor (uav) system using fuzzy pid controller (an experimental test). p. 99–104, 2015. Cited on page 15.

ANDRADE, F. A. A. et al. Autonomous unmanned aerial vehicles in search and rescue missions using real-time cooperative model predictive control. *Sensors*, MDPI AG, v. 19, n. 19, p. 4067, Sep 2019. ISSN 1424-8220. Disponível em: <http://dx.doi.org/10.3390/s19194067>. Cited on page 15.

ANP, A. N. d. P. *Dynamic Panel of Oil and Gas Production*. 2021. https://www.gov.br/anp/pt-br/assuntos/exploracao-e-producao-de-oleo-e-gas/paineis-dinamicos-de-producao-de-petroleo-e-gas-natural. Acessado em 17/02/2021. Cited 6 times on page xi, 20, 52, 53, 54, and 58.

ARDUINO. *Arduino Mega 2560*. 2021. https://store.arduino.cc/usa/mega-2560-r3. Accessed in 02/17/2021. Cited on page 48.

ARDUPILOT. *APM Planner 2*. 2020. https://ardupilot.org/planner2/. Acessado em 09/06/2020. Cited on page 50.

ARDUPILOT. *Mission Planner*. 2021. Accessed: 2020-06-15. Disponível em: <https://ardupilot.org-/planner/>. Cited on page 24.

ATOEV, S. et al. Data analysis of the mavlink communication protocol. p. 1–3, 2017. Cited on page 50.

AZDRONE. *AZ 4k Green Bee 1200*. 2021. https://www.gobizkorea.com/user/goods/frontGoodsDetail.do?goods_no=GS20180317156053. Acessado em 28/02/2021. Cited on page 80.

BALSYS, R. *YOLOv3 theory explained*. 2019. Accessed: 2020-06-15. Disponível em: <https:/-/pylessons.com/>. Cited 4 times on page xi, 29, 30, and 50.

BCB. *Economic Panorama*. 2021. https://www.bcb.gov.br/. Acessado em 23/02/2021. Cited 2 times on page 55 and 83.

BELYADI, H.; FATHI, E.; BELYADI, F. Chapter seventeen - decline curve analysis. In: BELYADI, H.; FATHI, E.; BELYADI, F. (Ed.). *Hydraulic Fracturing in Unconventional Reservoirs (Second Edition)*. Second edition. Gulf Professional Publishing, 2019. p. 311–340. ISBN 978-0-12-817665-8. Disponível em: <https://www.sciencedirect.com/science/article/pii/B9780128176658000175>. Cited on page 52.

BLANGER, L.; HIRATA, N. S. T. An evaluation of deep learning techniques for qr code detection. p. 1625–1629, 2019. Cited 2 times on page 50 and 64.

BROKERS, S. B. M. *Tenders and Auctions*. 2020. https://www.seaboats.net/shop. Accessed in 06/09/2020. Cited 2 times on page 55 and 79.

BRS. *Tanker*. 2020. https://www.brsbrokers.com/assets/review_splits/BRS_Review_2020_Tanker.pdf. Accessed in 06/09/2020. Cited 2 times on page 55 and 79.

BRUHN, A.; WEICKERT, J.; SCHNÖRR, C. Lucas/kanade meets horn/schunck: Combining local and global optic flow methods. *International Journal of Computer Vision*, v. 61, n. 3, p. 211–231, Feb 2005. ISSN 1573-1405. Disponível em: <https://doi.org/10.1023/B:VISI.0000045324.43199.43>. Cited on page 36.

CAMACHO, C. *Convolutional Neural Networks*. 2018. https://cezannec.github.io/Convolutional_Neural_Networks/. Accessed in 02/06/2021. Cited 3 times on page xi, 25, and 26.

CASELLA, E. et al. Accuracy of sand beach topography surveying by drones and photogrammetry. *Geo-Marine Letters*, v. 40, n. 2, p. 255–268, Apr 2020. ISSN 1432-1157. Disponível em: <https://doi.org/10.1007/s00367-020-00638-8>. Cited 2 times on page 33 and 36.

CHANG, P.; PADR, T. Model-based manipulation of linear flexible objects: Task automation in simulation and real world. *Machines*, v. 8, n. 3, 2020. ISSN 2075-1702. Disponível em: <https://www.mdpi.com/2075-1702/8/3/46>. Cited on page 69.

CHOI, J. et al. Gaussian yolov3: An accurate and fast object detector using localization uncertainty for autonomous driving. p. 502–511, 2019. Cited 2 times on page 27 and 33.

CHU, J. L.; KRZYAK, A. Analysis of feature maps selection in supervised learning using convolutional neural networks. In: _____. *Advances in Artificial Intelligence*. Springer International Publishing, 2014. p. 5970. Disponível em: <http://dx.doi.org/10.1007/978-3-319-06483-3_6>. Cited 2 times on page 26 and 27.

CHUANG, H.-M.; HE, D.; NAMIKI, A. Autonomous target tracking of uav using high-speed visual feedback. *Applied Sciences*, v. 9, n. 21, 2019. ISSN 2076-3417. Disponível em: <https://www.mdpi.com/2076-3417/9/21/4552>. Cited 3 times on page 17, 34, and 36.

CHUI, C. K.; CHEN, G. *Kalman Filtering with Real-Time Applications*. 5. ed. [S.l.]: Springer, 2017. v. 1. 247 p. Cited on page 31.

CLARKSONS. *AHTS and PSV*. 2020. https://offshore.clarksons.com/. Accessed in 06/09/2020. Cited 2 times on page 55 and 79.

COELHO, F. O. et al. Ekf and computer vision for mobile robot localization. p. 148–153, 2018. Cited on page 15.

CVAT. *Computer Vision Annotation Tool*. 2021. https://cvat.org/. Acessado em 09/01/2021. Cited on page 42.

DNV, D. N. V. *Recommended Practice DNV-RP-H103: Modelling and Analysis of Marine Operations*. 2020. https://home.hvl.no/ansatte/tct/FTP/H2020%20Marinteknisk%20Analyse/Regelverk%20og%20standarder/DnV_documents/RP-H103.pdf. Cited on page 41.

DOVIS, F. *GNSS Interference Threats and Countermeasures*. Norwood: Artech House, 2015. (The GNSS technology and application series). ISBN 1608078108. Cited on page 24.

DRIESSEN, S. et al. Experimentally validated extended kalman filter for uav state estimation using low-cost sensors. *IFAC-PapersOnLine*, v. 51, n. 15, p. 43–48, 2018. ISSN 2405-8963. 18th IFAC Symposium on System Identification SYSID 2018. Disponível em: <https://www.sciencedirect.com/science/article/pii/S2405896318317488>. Cited 3 times on page 35, 36, and 46.

DRONEVOLT. *Hercules 20 heavy-lift drone*. 2021. https://www.dronevolt.com/en/expert-solutions/hercules-20/. Acessado em 28/02/2021. Cited on page 80.

DSB. *Tugboats for charter*. 2020. https://www.dsboffshore.com/vessels-for-charter/tugs/. Accessed in 06/09/2020. Cited 2 times on page 55 and 79.

DUGGAL, A.; MINNEBO, J. The floating production, storage and offloading system past, present and future. Day 2 Tue, May 05, 2020, 05 2020. D021S017R005. Disponível em: <https://doi.org/10.4043-/30514-MS>. Cited on page 20.

DURDEVIC, P. et al. Vision aided navigation of a quad-rotor for autonomous wind-farm inspection. *IFAC-PapersOnLine*, v. 52, n. 8, p. 61–66, 2019. ISSN 2405-8963. 10th IFAC Symposium on Intelligent Autonomous Vehicles IAV 2019. Disponível em: <https://www.sciencedirect.com/science/article/pii-/S2405896319303696>. Cited 4 times on page 15, 16, 33, and 36.

FAMIGLIETTI, N. A. et al. A test on the potential of a low cost unmanned aerial vehicle rtk/ppk solution for precision positioning. *Sensors*, v. 21, n. 11, 2021. ISSN 1424-8220. Disponível em: <https:-//www.mdpi.com/1424-8220/21/11/3882>. Cited on page 24.

FREDERIKSEN, M.; KNUDSEN, M. *Drones for Offshore and Maritime Missions: Opportunities and Barriers*. [S.l.]: Center for Integrative Innovation Management, SDU, 2018. Cited 2 times on page 16 and 36.

FREEFLY. *Alta*. 2021. https://freeflysystems.com/alta. Acessado em 28/02/2021. Cited on page 80.

GARRIDO-JURADO, S. et al. Automatic generation and detection of highly reliable fiducial markers under occlusion. *Pattern Recognition*, Elsevier, v. 47, n. 6, p. 2280–2292, 2014. Cited 2 times on page 34 and 49.

GAZEBO. *Gazebo Robot Simulator*. 2021. http://gazebosim.org/. Acessado em 26/02/2021. Cited on page 63.

GONZALEZ, M. et al. Yoloff: You only learn offsets for robust 6dof object pose estimation. *arXiv preprint arXiv:2002.00911*, 2020. Cited on page 27.

GRYTE, K. et al. Robust navigation of uav using inertial sensors aided by uwb and rtk gps. In: _____. *AIAA Guidance, Navigation, and Control Conference*. [s.n.]. Disponível em: <https://arc.aiaa.org/doi-/abs/10.2514/6.2017-1035>. Cited 2 times on page 33 and 36.

HEIN, G. W. Status, perspectives and trends of satellite navigation. *Satellite Navigation*, v. 1, n. 1, p. 22, Aug 2020. ISSN 2662-1363. Disponível em: <https://doi.org/10.1186/s43020-020-00023-x>. Cited on page 23.

HSU, G. Z. . L.-T. Intelligent gnss/ins integrated navigation system for a commercial uav flight control system. *Aerospace Science and Technology*, v. 80, p. 368–380, 2018. ISSN 1270-9638. Disponível em: <https://www.sciencedirect.com/science/article/pii/S127096381830600X>. Cited on page 25.

INSPIREDFLIGHT. *IF-1200 Hexacopter*. 2021. https://inspiredflight.com/if1200-hexacopter/. Acessado em 28/02/2021. Cited on page 80.

JIANG, C.; XU, B.; HSU, L.-T. Probabilistic approach to detect and correct gnss nlos signals using an augmented state vector in the extended kalman filter. *GPS Solutions*, v. 25, n. 2, p. 72, Mar 2021. ISSN 1521-1886. Disponível em: <https://doi.org/10.1007/s10291-021-01101-6>. Cited on page 31.

KAARTINEN, H. et al. Accuracy of kinematic positioning using global satellite navigation systems under forest canopies. *Forests*, v. 6, n. 9, p. 3218–3236, 2015. ISSN 1999-4907. Disponível em: <https:/-/www.mdpi.com/1999-4907/6/9/3218>. Cited on page 24.

KARNEY, C.; DEAKIN, R. F.w. bessel (1825): The calculation of longitude and latitude from geodesic measurements. *Astronomical Notes*, Wiley Online Library, v. 331, n. 8, p. 852–861, 2010. Cited on page 39.

KELLY, J.; SARIPALLI, S.; SUKHATME, G. S. Combined visual and inertial navigation for an unmanned aerial vehicle. In: _____. *Field and Service Robotics: Results of the 6th International Conference*. Berlin, Heidelberg: Springer Berlin Heidelberg, 2008. p. 255–264. ISBN 978-3-540-75404-6. Disponível em: <https://doi.org/10.1007/978-3-540-75404-6_24>. Cited 2 times on page 35 and 36.

KHAN, S. et al. [S.l.: s.n.], 2018. v. 1. 207 p. Cited on page 25.

KIM, G.; PARK, H.; ZHANG, X. A method on using drone for connecting messenger lines in power transmission line construction. In: . [s.n.], 2019. p. 731–736. Disponível em: <https://ieeexplore.ieee.org/document/8939933>. Cited 2 times on page 16 and 36.

KIM, Y.; BANG, H. Introduction to kalman filter and its applications. In: GOVAERS, F. (Ed.). *Introduction and Implementations of the Kalman Filter*. Rijeka: IntechOpen, 2019. cap. 2. Disponível em: <https://doi.org/10.5772/intechopen.80600>. Cited 2 times on page 30 and 31.

KOENIG, N.; HOWARD, A. Design and use paradigms for gazebo, an open-source multi-robot simulator. v. 3, p. 2149–2154, 2004. Cited on page 16.

KOTUG. *Drone technology for safer tug operations*. 2018. Accessed: 2020-06-15. Disponível em: <https://www.kotug.com/newsmedia/drone-technology-safer-tug-operations>. Cited 2 times on page 16 and 36.

KUMAR, K. P. Design and analysis of cmos schmitt trigger. *International Journal of Innovative Technology and Exploring Engineering*, v. 8, p. 106, 05 2019. Cited on page 48.

LECHNER, W.; BAUMANN, S. Global navigation satellite systems. *Computers and Electronics in Agriculture*, v. 25, n. 1, p. 67–85, 2000. ISSN 0168-1699. Disponível em: <https://www.sciencedirect.com/science/article/pii/S0168169999000563>. Cited on page 23.

MARINA, H. G. de et al. Uav attitude estimation using unscented kalman filter and triad. *IEEE Transactions on Industrial Electronics*, v. 59, n. 11, p. 4465–4474, 2012. Cited 2 times on page 35 and 36.

MARTINEZ-ALPISTE, I. et al. A dynamic discarding technique to increase speed and preserve accuracy for yolov3. *Neural Computing and Applications*, Mar 2021. ISSN 1433-3058. Disponível em: <https://doi.org/10.1007/s00521-021-05764-7>. Cited 2 times on page 28 and 30.

MCMAHON, C.; MORA, O. E.; STAREK, M. J. Evaluating the performance of suas photogrammetry with ppk positioning for infrastructure mapping. *Drones*, v. 5, n. 2, 2021. ISSN 2504-446X. Disponível em: <https://www.mdpi.com/2504-446X/5/2/50>. Cited on page 24.

MELENDEZ-PASTOR, C.; RUIZ-GONZALEZ, R.; GOMEZ-GIL, J. A data fusion system of gnss data and on-vehicle sensors data for improving car positioning precision in urban environments. *Expert Systems with Applications*, v. 80, p. 28–38, 2017. ISSN 0957-4174. Disponível em: <https://www.sciencedirect.com/science/article/pii/S0957417417301641>. Cited 2 times on page 24 and 31.

MENEGALDO, L. L. et al. Development and navigation of a mobile robot for floating production storage and offloading ship hull inspection. *IEEE Transactions on Industrial Electronics*, v. 56, n. 9, p. 3717–3722, 2009. Cited on page 20.

MOHAN, S. et al. *Introduction to the Kalman Filter and Tuning its Statistics for Near Optimal Estimates and Cramer Rao Bound*. 2015. Cited on page 31.

MULLENDERS, V. Design of a motion monitoring system for unmanned offshore topside installation based on real-time visual object tracking using drones and fixed cameras on an sscv. 2019. Cited on page 15.

OCIMF, O. C. I. M. F. *Guidelines for Offshore Tanker Operations*. London, United Kingdom: Oil Companies International Marine Forum, 2018. Cited 5 times on page 20, 21, 22, 23, and 54.

ONYXSTAR. *Hydra-12*. 2021. https://www.onyxstar.net/hydra-12/. Acessado em 28/02/2021. Cited on page 80.

O'SHEA, K.; NASH, R. *An Introduction to Convolutional Neural Networks*. 2015. Cited on page 26.

OXTS. *What is RTK?* 2021. https://www.oxts.com/rtk/. Accessed in 02/06/2021. Cited 2 times on page xi and 25.

PADILLA, R.; NETTO, S. L.; SILVA, E. A. B. da. A survey on performance metrics for object-detection algorithms. p. 237–242, 2020. Cited on page 43.

PAN, Z.; CHAI, H.; KONG, Y. Integrating multi-gnss to improve the performance of precise point positioning. *Advances in Space Research*, v. 60, n. 12, p. 2596–2606, 2017. ISSN 0273-1177. BDS/GNSS+: Recent Progress and New Applications - Part 2. Disponível em: <https://www.sciencedirect.com-/science/article/pii/S0273117717300443>. Cited on page 24.

PETILLOT, Y. R. et al. Underwater robots: From remotely operated vehicles to intervention-autonomous underwater vehicles. *IEEE Robotics & Automation Magazine*, IEEE, v. 26, n. 2, p. 94–101, 2019. Cited on page 15.

PETRITOLI, E.; LECCESE, F.; CIANI, L. Reliability and maintenance analysis of unmanned aerial vehicles. *Sensors*, v. 18, p. 3171, 09 2018. Cited 2 times on page 56 and 58.

PINTO, M. F. et al. Arcog: An aerial robotics cognitive architecture. *Robotica*, Cambridge University Press, p. 1–20, 2020. Cited on page 15.

PINTO, M. F. et al. A robotic cognitive architecture for slope and dam inspections. *Sensors*, Multidisciplinary Digital Publishing Institute, v. 20, n. 16, p. 4579, 2020. Cited on page 15.

PINTO, M. F. et al. A framework for analyzing fog-cloud computing cooperation applied to information processing of uavs. *Wireless Communications and Mobile Computing*, Hindawi, v. 2019, 2019. Cited on page 15.

PINTO, M. F. et al. Case-based reasoning approach applied to surveillance system using an autonomous unmanned aerial vehicle. p. 1324–1329, 06 2017. Cited on page 15.

PIXHAWK. *Controller Diagrams*. 2021. https://docs.px4.io/master/en/flight_stack/controller_diagrams.html. Accessed in 05/26/2021. Cited on page 65.

QIN, X.; WANG, T. Visual-based tracking and control algorithm design for quadcopter uav. p. 3564–3569, 2019. Cited 3 times on page 16, 34, and 36.

QUIGLEY, M. et al. Ros: an open-source robot operating system. v. 3, n. 3.2, p. 5, 2009. Cited on page 50.

RAMOS, G. S.; PINTO, M. F. *Shuttle Tanker, FPSO and FSO image dataset for ship recognition*. IEEE Dataport, 2021. Disponível em: <https://dx.doi.org/10.21227/9xzy-fd09>. Cited on page 18.

RAMOS, G. S. et al. Technical and economic feasibility study for implementing a novel mooring-assisting methodology in offloading operations using autonomous unmanned aerial vehicles. *SPE Production Operations*, p. 1–16, Jun 2021. ISSN 1930-1863. Disponível em: <https://doi.org/10.2118/205524-PA>. Cited 17 times on page xi, xii, xiii, 22, 33, 38, 39, 42, 51, 60, 61, 64, 68, 69, 79, 81, and 82.

REDMON, J. et al. You only look once: Unified, real-time object detection. p. 779–788, 2016. Cited 3 times on page 28, 30, and 42.

REDMON, J.; FARHADI, A. Yolov3: An incremental improvement. 04 2018. Cited 5 times on page xi, 27, 28, 29, and 30.

REZATOFIGHI, H. et al. Generalized intersection over union. June 2019. Cited 2 times on page 50 and 64.

RIKIMARU. *RP9 Professional PE*. 2020. http://www.fishingc.com/productinfo/99929.html. Accessed in 10/16/2020. Cited on page 71.

RODIN, C. D. et al. Cited on page 15.

SANTOSO, F.; GARRATT, M. A.; ANAVATTI, S. G. Visualinertial navigation systems for aerial robotics: Sensor fusion and technology. *IEEE Transactions on Automation Science and Engineering*, v. 14, n. 1, p. 260–275, 2017. Cited on page 34.

SELECKý, M. et al. Framework for incremental development of complex unmanned aircraft systems. p. J3–1–J3–9, 2015. Cited on page 15.

SILVA, M. et al. Design of angular pid controllers for quadcopters built with low cost equipment. p. 216–221, 2016. Cited on page 15.

SPE, S. o. P. E. *Tugboat Company Takes Its Business Flying With Drones*. 2018. Accessed: 2020-06-15. Disponível em: <https://jpt.spe.org/tugboat-company-takes-its-business-flying-drones>. Cited on page 16.

SPHAIER, S. H. et al. On the safety of offloading operation in the oil industry. *International Journal of Computer Applications in Technology*, Inderscience Publishers, v. 43, n. 3, p. 207, 2012. Disponível em: <http://dx.doi.org/10.1504/IJCAT.2012.046307>. Cited on page 57.

STAVINOHA, S. et al. Challenges of robotics and automation in offshore oil&gas industry. p. 557–562, 2014. Cited on page 23.

TOMATíK, J. et al. Uav rtk/ppk methodan optimal solution for mapping inaccessible forested areas? *Remote Sensing*, v. 11, n. 6, 2019. ISSN 2072-4292. Disponível em: <https://www.mdpi.com/2072-4292/11/6/721>. Cited 2 times on page 33 and 36.

UAVSYSTEMS. *Tarot T-18 V2.1*. 2021. https://uavsystemsinternational.com/products/tarot-t-18-ready-fly-drone. Acessado em 28/02/2021. Cited on page 80.

VULCANUAV. *Aircraft Series*. 2021. http://vulcanuav.com/aircraft/. Acessado em 28/02/2021. Cited 4 times on page 69, 79, 80, and 83.

WANG, X.; CUI, N.; GUO, J. Ins/visnav/gps relative navigation system for uav. *Aerospace Science and Technology*, v. 28, n. 1, p. 242–248, 2013. ISSN 1270-9638. Disponível em: <https://www.sciencedirect.com/science/article/pii/S127096381200185X>. Cited 2 times on page 25 and 31.

XU, H. et al. Vision / inertial integrated navigation method for quadcopter based on EKF state observer. *Journal of Physics: Conference Series*, IOP Publishing, v. 1748, p. 062076, jan 2021. Disponível em: <https://doi.org/10.1088/1742-6596/1748/6/062076>. Cited 2 times on page 35 and 36.

YEDJOUR, H. Optical flow based on lucas-kanade method for motion estimation. Springer International Publishing, Cham, p. 937–945, 2021. Cited on page 37.

YU, L. et al. Inspection robots in oil and gas industry: a review of current solutions and future trends. p. 1–6, 2019. Cited on page 15.

YUNEEC. *Typhoon H User Manual V1.1*. 2020. https://static.bhphotovideo.com/lit_files/319649.pdf. Accessed in 10/16/2020. Cited on page 72.

ZHANG, M. et al. Research on the application of deep learning YOLOv3 in aerial patrol inspection of optical cable lines. *Journal of Physics: Conference Series*, IOP Publishing, v. 1345, p. 032068, nov 2019. Disponível em: <https://doi.org/10.1088/1742-6596/1345/3/032068>. Cited on page 30.

ZHANG, Q. et al. An improved robust adaptive kalman filter for gnss precise point positioning. *IEEE Sensors Journal*, v. 18, n. 10, p. 4176–4186, 2018. Cited 2 times on page 24 and 31.

ZHANG, T.; LIAO, Y. Attitude measure system based on extended kalman filter for multi-rotors. *Computers and Electronics in Agriculture*, v. 134, p. 19–26, 2017. ISSN 0168-1699. Disponível em: <https://www.sciencedirect.com/science/article/pii/S0168169916312418>. Cited on page 32.

ZHANG, Y.; LI, Q.-Z.; ZANG, F.-N. Ship detection for visual maritime surveillance from non-stationary platforms. *Ocean Engineering*, v. 141, p. 53–63, 2017. ISSN 0029-8018. Disponível em: <https://www.sciencedirect.com/science/article/pii/S0029801817303190>. Cited 2 times on page 34 and 36.

ZIMMERMANN, F. et al. Precise Positioning of Uavs - Dealing with Challenging Rtk-Gps Measurement Conditions during Automated Uav Flights. *ISPRS Annals of Photogrammetry, Remote Sensing and Spatial Information Sciences*, v. 42W3, p. 95–102, ago. 2017. Cited 2 times on page 33 and 36.